

Nucleon generalized parton distributions from full lattice QCDPh. Hägler,¹ W. Schroers,^{2,*} J. Bratt,³ J. W. Negele,³ A. V. Pochinsky,³ R. G. Edwards,⁴ D. G. Richards,⁴ M. Engelhardt,⁵ G. T. Fleming,⁶ B. Musch,¹ K. Orginos,^{4,7} and D. B. Renner⁸

(LHPC Collaboration)

¹*Institut für Theoretische Physik T39, Physik-Department der TU München, James-Franck-Straße, D-85747 Garching, Germany*²*John von Neumann-Institut für Computing NIC/DESY, D-15738 Zeuthen, Germany*³*Center for Theoretical Physics, Massachusetts Institute of Technology, Cambridge, Massachusetts 02139, USA*⁴*Thomas Jefferson National Accelerator Facility, Newport News, Virginia 23606, USA*⁵*Physics Department, New Mexico State University, Las Cruces, New Mexico 88003-8001, USA*⁶*Sloane Physics Laboratory, Yale University, New Haven, Connecticut 06520, USA*⁷*Department of Physics, College of William and Mary, Williamsburg, Virginia 23187-8795, USA*⁸*Department of Physics, University of Arizona, 1118 E. 4th Street, Tucson, Arizona 85721, USA*

(Received 10 June 2007; revised manuscript received 4 January 2008; published 6 May 2008)

We present a comprehensive study of the lowest moments of nucleon generalized parton distributions in $N_f = 2 + 1$ lattice QCD using domain-wall valence quarks and improved staggered sea quarks. Our investigation includes helicity dependent and independent generalized parton distributions for pion masses as low as 350 MeV and volumes as large as $(3.5 \text{ fm})^3$, for a lattice spacing of 0.124 fm. We use perturbative renormalization at one-loop level with an improvement based on the nonperturbative renormalization factor for the axial vector current, and only connected diagrams are included in the isosinglet channel.

DOI: [10.1103/PhysRevD.77.094502](https://doi.org/10.1103/PhysRevD.77.094502)

PACS numbers: 12.38.Gc, 13.60.Fz

I. INTRODUCTION

Generalized parton distributions (GPDs) [1–4] play a vital role in our understanding of the structure of the nucleon in terms of the fundamental building blocks of QCD, the quarks and gluons. Before the advent of GPDs, fundamental questions as to the origin of the spin of the nucleon, the decomposition of the nucleon total momentum, and the distribution and density of the nucleon constituents in position and momentum space seemed to be largely unrelated. In some cases, it was even unclear how to formulate these questions in a theoretically sound way and how to measure the underlying observables experimentally. With the introduction of GPDs, it is possible not only to give precise definitions to quantities, such as the quark and gluon angular momentum contributions to the nucleon spin [5] and the probability densities of quarks and gluons in impact parameter space [6], but also to unify and extend the successful concepts of parton distribution functions (PDFs) and form factors. Nucleon generalized parton distributions are experimentally accessible in deeply virtual Compton scattering of virtual photons off a nucleon and a range of other related processes [7–10]. Since these reactions involve in general convolutions of GPDs over the longitudinal momentum fraction x , which makes it difficult if not impossible to map them over the whole parameter

space, the most stringent quantitative information on GPDs currently comes from quark PDFs and nucleon form factors [11].

Complementary to experimental efforts, lattice QCD offers a unique opportunity to calculate x -moments of GPDs from first principles. The first investigations of GPDs including studies of the quark angular momentum contributions to the nucleon spin have been presented by the QCDSF Collaboration in quenched QCD [12] and by LHPC/SESAM in $N_f = 2$ lattice QCD [13]. Lattice results on nucleon GPDs published since then have provided important insights into the transverse structure of unpolarized nucleons [14], the lowest moments of polarized [15] and tensor GPDs [16], and transverse spin densities of quarks in the nucleon [17,18]. With the exception of several initial studies [19,20], all previously published lattice results on GPDs have been obtained from calculations in a two-flavor “heavy pion world” with pion masses in the range of 550 to over 1000 MeV. In this work, we improve on previous studies by presenting a comprehensive analysis of the lowest three moments of unpolarized and polarized GPDs in $N_f = 2 + 1$ lattice QCD with pion masses as low as 350 MeV and volumes as large as $(3.5 \text{ fm})^3$.

The paper is organized as follows. We begin with an introduction to the calculation of moments of GPDs in lattice QCD in Sec. II. Section III describes the hybrid approach of using domain-wall valence quarks with $2 + 1$ flavors of improved staggered sea quarks. In Sec. IV we present our numerical results for the generalized form factors, including a discussion and interpretation of the

*Present address: Department of Physics, Center for Theoretical Sciences, National Taiwan University, Taipei 10617, Taiwan.

quark orbital angular momentum (OAM) and the transverse nucleon structure. Chiral extrapolations of selected lattice results to the physical pion mass are presented in Sec. V. Conclusions are given in the final section.

II. LATTICE CALCULATION OF MOMENTS OF GENERALIZED PARTON DISTRIBUTIONS

Generalized parton distributions determine off-forward matrix elements of gauge invariant light cone operators

$$\mathcal{O}_\Gamma(x) = \int \frac{d\lambda}{4\pi} e^{i\lambda x} \bar{q}\left(\frac{-\lambda n}{2}\right) \Gamma \mathcal{P} e^{-ig \int_{-\lambda/2}^{\lambda/2} d\alpha n \cdot A(\alpha n)} q\left(\frac{\lambda n}{2}\right), \quad (1)$$

where x is the momentum fraction, n is a light cone vector and $\Gamma = \not{n}$ or $\Gamma = \not{n}\gamma_5$. The twist-2 tensor GPDs [21] related to $\Gamma = n_\mu \sigma^{\mu j}$, $j = 1, 2$ are not studied in this work. The four independent twist-2 unpolarized and polarized generalized parton distributions H , E , \tilde{H} and \tilde{E} are defined by the parametrizations

$$\langle P', \Lambda' | \mathcal{O}_{\not{n}}(x) | P, \Lambda \rangle = \langle \not{n} \rangle H(x, \xi, t) + \frac{n_\mu \Delta^\nu}{2m} \times \langle \langle i\sigma^{\mu\nu} \rangle \rangle E(x, \xi, t), \quad (2)$$

and

$$\langle P', \Lambda' | \mathcal{O}_{\not{n}\gamma_5}(x) | P, \Lambda \rangle = \langle \not{n}\gamma_5 \rangle \tilde{H}(x, \xi, t) + \frac{n \cdot \Delta}{2m} \times \langle \langle \gamma_5 \rangle \rangle \tilde{E}(x, \xi, t), \quad (3)$$

where we use the shorthand notation $\langle \langle \Gamma \rangle \rangle = \bar{U}(P', \Lambda') \Gamma U(P, \Lambda)$ for products of Dirac spinors U , and where $\Delta = P' - P$, $t = \Delta^2$ and $\xi = -n \cdot \Delta/2$. In Eqs. (2) and (3) we suppress the dependence of the GPDs on the resolution scale μ^2 . An illustration of the GPDs parametrizing the lower part of the handbag diagram is given in Fig. 1. The momentum fractions x and ξ both have support

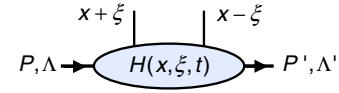


FIG. 1 (color online). GPDs as part of a scattering amplitude.

in the interval $[-1, +1]$. Depending on x , there are three kinematic regions, which offer different interpretations for the GPDs. For $x \in [\xi, 1]$ and $x \in [-1, -\xi]$, the GPDs describe the emission and reabsorption of quarks and antiquarks, respectively. In the case that x lies in the interval $[-\xi, \xi]$, they describe the emission of a $q\bar{q}$ -pair.

In our lattice calculations, we do not work directly with the bi-local operators in Eq. (1) but instead consider moments, defined by the integral $\int_{-1}^1 dx x^{n-1} f(x)$, of the operators in Eqs. (2) and (3), leading to towers of symmetrized, traceless local operators

$$\mathcal{O}_{[\gamma_5]}^{\{\mu_1 \dots \mu_n\}} = \bar{q}(0) \gamma^{\{\mu_1} [\gamma_5] i\vec{D}^{\mu_2} \dots i\vec{D}^{\mu_n\}} q(0), \quad (4)$$

where $[\gamma_5]$ denotes the possible inclusion of the corresponding matrix, the curly brackets represent a symmetrization over the indices μ_i and subtraction of traces, and $\vec{D} = 1/2(\vec{D} + \vec{D})$. We relate nucleon matrix elements of the tower of local operators in Eq. (4) to x -moments of the twist-2 GPDs. To this end, we parametrize off-forward matrix elements $\langle P', \Lambda' | \mathcal{O}^{\{\mu_1 \dots \mu_n\}} | P, \Lambda \rangle$ in terms of the generalized form factors $A_{ni}(t)$, $B_{ni}(t)$, $C_{n0}(t)$, $\tilde{A}_{ni}(t)$, and $\tilde{B}_{ni}(t)$. Apart from potential difficulties related to lattice operator mixing for higher moments n , lattice measurements of the operators in Eq. (4) become increasingly noisy as the number of derivatives increases, and we therefore restrict our calculations to $n \leq 3$. The parametrization of nucleon matrix elements of Eq. (4) in terms of generalized form factors (GFFs) for $n = 1, 2$ and 3 reads [4,22]

$$\begin{aligned} \langle P' | \mathcal{O}^{\mu_1} | P \rangle &= \langle \langle \gamma^{\mu_1} \rangle \rangle A_{10}(t) + \frac{i}{2m} \langle \langle \sigma^{\mu_1 \alpha} \rangle \rangle \Delta_\alpha B_{10}(t), \\ \langle P' | \mathcal{O}^{\{\mu_1 \mu_2\}} | P \rangle &= \bar{P}^{\{\mu_1} \langle \langle \gamma^{\mu_2\} \rangle \rangle A_{20}(t) + \frac{i}{2m} \bar{P}^{\{\mu_1} \langle \langle \sigma^{\mu_2\} \alpha \rangle \rangle \Delta_\alpha B_{20}(t) + \frac{1}{m} \Delta^{\{\mu_1} \Delta^{\mu_2\}} C_{20}(t), \\ \langle P' | \mathcal{O}^{\{\mu_1 \mu_2 \mu_3\}} | P \rangle &= \bar{P}^{\{\mu_1} \bar{P}^{\mu_2} \langle \langle \gamma^{\mu_3\} \rangle \rangle A_{30}(t) + \frac{i}{2m} \bar{P}^{\{\mu_1} \bar{P}^{\mu_2} \langle \langle \sigma^{\mu_3\} \alpha \rangle \rangle \Delta_\alpha B_{30}(t) + \Delta^{\{\mu_1} \Delta^{\mu_2} \langle \langle \gamma^{\mu_3\} \rangle \rangle A_{32}(t) \\ &\quad + \frac{i}{2m} \Delta^{\{\mu_1} \Delta^{\mu_2} \langle \langle \sigma^{\mu_3\} \alpha \rangle \rangle \Delta_\alpha B_{32}(t), \end{aligned} \quad (5)$$

for the unpolarized case, and

$$\begin{aligned} \langle P' | \mathcal{O}_{\gamma_5}^{\mu_1} | P \rangle &= \langle \langle \gamma^{\mu_1} \gamma_5 \rangle \rangle \tilde{A}_{10}(t) + \frac{1}{2m} \Delta^{\mu_1} \langle \langle \gamma_5 \rangle \rangle \tilde{B}_{10}(t), \\ \langle P' | \mathcal{O}_{\gamma_5}^{\{\mu_1 \mu_2\}} | P \rangle &= \bar{P}^{\{\mu_1} \langle \langle \gamma^{\mu_2\} \gamma_5 \rangle \rangle \tilde{A}_{20}(t) + \frac{1}{2m} \Delta^{\{\mu_1} \bar{P}^{\mu_2\}} \langle \langle \gamma_5 \rangle \rangle \tilde{B}_{20}(t), \\ \langle P' | \mathcal{O}_{\gamma_5}^{\{\mu_1 \mu_2 \mu_3\}} | P \rangle &= \bar{P}^{\{\mu_1} \bar{P}^{\mu_2} \langle \langle \gamma^{\mu_3\} \gamma_5 \rangle \rangle \tilde{A}_{30}(t) + \frac{1}{2m} \Delta^{\{\mu_1} \bar{P}^{\mu_2} \bar{P}^{\mu_3\}} \langle \langle \gamma_5 \rangle \rangle \tilde{B}_{30}(t) + \Delta^{\{\mu_1} \Delta^{\mu_2} \langle \langle \gamma^{\mu_3\} \gamma_5 \rangle \rangle \tilde{A}_{32}(t) \\ &\quad + \frac{1}{2m} \Delta^{\{\mu_1} \Delta^{\mu_2} \Delta^{\mu_3\}} \langle \langle \gamma_5 \rangle \rangle \tilde{B}_{32}(t), \end{aligned} \quad (6)$$

for the polarized case. Here and in the following we set $\bar{P} = (P' + P)/2$.

Using Eqs. (2), (3), (5), and (6), it is easy to show that Mellin-moments of the GPDs,

$$\begin{aligned} H^n(\xi, t) &\equiv \int_{-1}^1 dx x^{n-1} H(x, \xi, t), \\ E^n(\xi, t) &\equiv \int_{-1}^1 dx x^{n-1} E(x, \xi, t), \\ \tilde{H}^n(\xi, t) &\equiv \int_{-1}^1 dx x^{n-1} \tilde{H}(x, \xi, t), \\ \tilde{E}^n(\xi, t) &\equiv \int_{-1}^1 dx x^{n-1} \tilde{E}(x, \xi, t), \end{aligned} \quad (7)$$

are given by polynomials in the longitudinal momentum transfer ξ and the GFFs. For the lowest three moments, the corresponding relations read

$$\begin{aligned} H^{n=1}(\xi, t) &= A_{10}(t), & H^{n=2}(\xi, t) &= A_{20}(t) + (2\xi)^2 C_{20}(t), \\ H^{n=3}(\xi, t) &= A_{30}(t) + (2\xi)^2 A_{32}(t), \\ E^{n=1}(\xi, t) &= B_{10}(t), & E^{n=2}(\xi, t) &= B_{20}(t) - (2\xi)^2 C_{20}(t), \\ E^{n=3}(\xi, t) &= B_{30}(t) + (2\xi)^2 B_{32}(t), \\ \tilde{H}^{n=1}(\xi, t) &= \tilde{A}_{10}(t), & \tilde{H}^{n=2}(\xi, t) &= \tilde{A}_{20}(t), \\ \tilde{H}^{n=3}(\xi, t) &= \tilde{A}_{30}(t) + (2\xi)^2 \tilde{A}_{32}(t), \\ \tilde{E}^{n=1}(\xi, t) &= \tilde{B}_{10}(t), & \tilde{E}^{n=2}(\xi, t) &= \tilde{B}_{20}(t), \\ \tilde{E}^{n=3}(\xi, t) &= \tilde{B}_{30}(t) + (2\xi)^2 \tilde{B}_{32}(t). \end{aligned} \quad (8)$$

The aim of our calculation is to extract the GFFs as functions of the momentum transfer squared, t , from nucleon two- and three-point-functions as described below. Once the GFFs have been obtained, the complete ξ -dependence of the moments of the GPDs is directly given by Eqs. (8). Let us note that the Mellin-moments in Eq. (7) are taken with respect to the entire interval from $x = -1$ to $+1$. Following our discussion below Eq. (3), we find that the moments of the GPDs at $\xi = 0$ correspond to sums and differences of contributions from quarks q and antiquarks \bar{q} . For example,

$$\begin{aligned} H_q^n(\xi = 0, t) &= \int_0^1 dx x^{n-1} (H_q(x, 0, t) + (-1)^n H_{\bar{q}}(x, 0, t)), \\ E_q^n(0, t) &= \int_0^1 dx x^{n-1} (E_q(x, 0, t) + (-1)^n E_{\bar{q}}(x, 0, t)), \\ \tilde{H}_q^n(0, t) &= \int_0^1 dx x^{n-1} (\tilde{H}_q(x, 0, t) + (-1)^{(n-1)} \tilde{H}_{\bar{q}}(x, 0, t)), \\ \tilde{E}_q^n(0, t) &= \int_0^1 dx x^{n-1} (\tilde{E}_q(x, 0, t) + (-1)^{(n-1)} \tilde{E}_{\bar{q}}(x, 0, t)). \end{aligned} \quad (9)$$

Such a simple decomposition is not possible for nonzero longitudinal momentum transfer $\xi \neq 0$. We denote the forward limit values of the moments of H and \tilde{H} in Eq. (9) by $\langle x^{n-1} \rangle_q = H_q^n(0, 0) = A_{n0}^q(0)$ and $\langle x^{n-1} \rangle_{\Delta q} =$

$\tilde{H}_q^n(0, 0) = \tilde{A}_{n0}^q(0)$, where $\langle x^{n-1} \rangle_q$ and $\langle x^{n-1} \rangle_{\Delta q}$ correspond to the moments of unpolarized and polarized quark parton distributions.

Below, we give a brief summary of the methods and techniques we used to extract moments of generalized parton distributions in lattice QCD. For details, we refer the reader to [13,23]. As usual, the matrix elements, Eqs. (5) and (6), are calculated from the ratio of nucleon three-point and two-point functions:

$$\begin{aligned} C^{2\text{pt}}(\tau, P) &= \sum_{j,k} (\Gamma_{\text{unpol}})_{jk} \langle N_k(\tau, P) \bar{N}_j(\tau_{\text{src}}, P) \rangle, \\ C_O^{3\text{pt}}(\tau, P', P) &= \sum_{j,k} (\Gamma_{\text{pol}})_{jk} \langle N_k(\tau_{\text{snk}}, P') \\ &\quad \times \mathcal{O}(\tau, \Delta) \bar{N}_j(\tau_{\text{src}}, P) \rangle, \end{aligned} \quad (10)$$

where $\Gamma_{\text{unpol}} = (1 + \gamma_4)/4$ and $\Gamma_{\text{pol}} = (1 + \gamma_4) \times (1 + i\gamma_5\gamma_3)/2$. The nucleon source, $\bar{N}(\tau, P)$, and sink, $N(\tau, P)$, create and annihilate states with the quantum numbers of the nucleon. To maximize the overlap with the ground state, we used the smeared sources given in [23]. The three-point-function $C_O^{3\text{pt}}(\tau, P', P)$ with the operator insertion at τ is illustrated in Fig. 2 in terms of quark propagators, showing examples of connected and disconnected contributions in an unquenched lattice calculation.

Using the transfer matrix formalism, we can rewrite Eqs. (10) to obtain

$$\begin{aligned} C^{2\text{pt}}(\tau, P) &= e^{-E_0(P)(\tau - \tau_{\text{src}})} (Z(P) \bar{Z}(P))^{1/2} \frac{E_0(P) + m}{E_0(P)} \\ &\quad + \text{higher states}, \end{aligned} \quad (11)$$

$$\begin{aligned} C_O^{3\text{pt}}(\tau, P', P) &= e^{-E_0(P)(\tau - \tau_{\text{src}}) - E_0(P')(\tau_{\text{snk}} - \tau)} \frac{(Z(P) \bar{Z}(P'))^{1/2}}{4E_0(P')E_0(P)} \\ &\quad \times \text{Tr}\{\Gamma_{\text{pol}}(i\not{P}' - m)(aA(t) + bB(t) + \dots) \\ &\quad \times (i\not{P} - m)\} + \text{higher states}, \end{aligned} \quad (12)$$

where the factors a, b, \dots represent the prefactors (including Dirac-matrices) of the corresponding GFFs $A(t), B(t), \dots$ in the parametrizations in Eqs. (5) and (6), transformed to Euclidean space. Higher states with energies $E_1 > E_0$ in Eqs. (11) and (12) are suppressed when $\tau_{\text{snk}} - \tau \gg 1/(E_1 - E_0)$ and $\tau - \tau_{\text{src}} \gg 1/(E_1 - E_0)$.

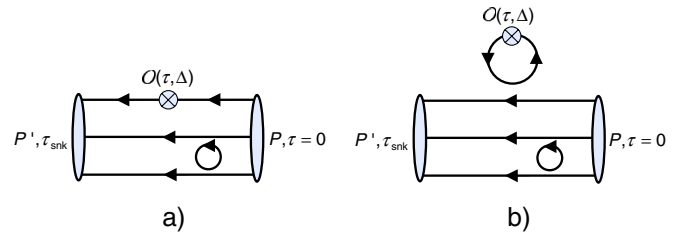


FIG. 2 (color online). Connected (a) and disconnected (b) diagrams in unquenched lattice QCD with an operator-insertion at τ and finite momentum transfer Δ .

In order to cancel the exponentials and Z-factors in Eq. (12) for zero and nonzero momentum transfer Δ , we construct the ratio of two- and three-point-functions

$$R_{\mathcal{O}}(\tau, P', P) = \frac{C_{\mathcal{O}}^{3\text{pt}}(\tau, P', P)}{C_{\mathcal{O}}^{2\text{pt}}(\tau_{\text{snk}}, P')} \left[\frac{C^{2\text{pt}}(\tau_{\text{snk}} - \tau + \tau_{\text{src}}, P) C^{2\text{pt}}(\tau, P') C^{2\text{pt}}(\tau_{\text{snk}}, P')}{C^{2\text{pt}}(\tau_{\text{snk}} - \tau + \tau_{\text{src}}, P') C^{2\text{pt}}(\tau, P) C^{2\text{pt}}(\tau_{\text{snk}}, P)} \right]^{1/2}. \quad (13)$$

For an operator-insertion sufficiently far away from the source and the sink in the Euclidean time direction, higher states are negligible, and the ratio $R_{\mathcal{O}}(\tau, P', P)$ exhibits a plateau in τ . We finally average over the plateau region from τ_{min} to τ_{max} to obtain an averaged ratio $\bar{R}_{\mathcal{O}}(P', P)$. On a finite periodic lattice with spatial extent L_s , three-momenta are given by $\vec{P} = 2\pi/(aL_s)\vec{n}$ with integer components $n_i = -L_s/2, \dots, L_s/2$, and for the nucleon energy we use the continuum dispersion relation $P_4 = \sqrt{m^2 + \vec{P}^2}$. Therefore, the discrete lattice momenta result in a finite set of values for the momentum transfer squared t which can be realized in our calculation.

In order to obtain symmetric and traceless operators $\mathcal{O}^{\{\mu_1\mu_2\dots\}}$, we have to choose specific linear combinations of the indices. For the diagonal operators typical examples are $\mathcal{O}_{i=1}^{n=2} = (\mathcal{O}^{11} + \mathcal{O}^{22} - \mathcal{O}^{33} - \mathcal{O}^{44})/2$ and $\mathcal{O}_{i=2}^{n=3} = (\mathcal{O}^{122} + \mathcal{O}^{133} - 2\mathcal{O}^{144})/\sqrt{2}$, where $\mathcal{O}_1^{n=2}$ belongs to the 3-dimensional irreducible $H(4)$ -representation $\tau_1^{(3)}$ for $n = 2$ and $\mathcal{O}_{i=2}^{n=3}$ is a member of the 8-dimensional representation $\tau_1^{(8)}$ for $n = 3$ [24]. The sets of operators \mathcal{O}_i^n we are using are the same as in [13]. Altogether, there are 9 linearly independent index combinations for $n = 2$ and 12 for $n = 3$. In order to be able to compare our results with experiment, the operators have to be renormalized and transformed to the $\overline{\text{MS}}$ -scheme at a renormalization scale μ^2 . In general, operators mix under renormalization, and the renormalization matrix $Z^{\mathcal{O}}$ is nondiagonal. We will denote the renormalized operators in the $\overline{\text{MS}}$ -scheme by $\mathcal{O}_i^{n,\overline{\text{MS}}} = Z_{ij}^{\mathcal{O}} \mathcal{O}_j^n$. Some details concerning the renormalization procedure and numerical results for the renormalization constants will be discussed at the end of the next section.

Based on the renormalized operators, we compute the averaged ratio $\bar{R}_{\mathcal{O}}(P', P)$ and equate it with the continuum parametrization in terms of the GFFs given in Eq. (12). This is done simultaneously for all momentum combinations P and P' corresponding to the same momentum transfer squared t and all contributing symmetric and traceless operators $\mathcal{O}_i^{n,\overline{\text{MS}}}$, giving a finite set of linear equations

$$\begin{aligned} \bar{R}_{\mathcal{O},k}(P'_1, P_1) &= c_{11}A(t) + c_{12}B(t) + \dots, \\ \bar{R}_{\mathcal{O},l}(P'_2, P_2) &= c_{21}A(t) + c_{22}B(t) + \dots, \\ \bar{R}_{\mathcal{O},m}(P'_3, P_3) &= c_{31}A(t) + c_{32}B(t) + \dots, \\ &\dots, \end{aligned} \quad (14)$$

where $(P'_j - P_j)^2 = t$ for all $j = 1, 2, 3, \dots$. The coefficients c_{ij} in Eqs. (14) only depend on the nucleon mass

m and the momenta P, P' and are calculated from the traces in Eq. (12). Finally, the set of Eqs. (14), which in general is overdetermined, is solved numerically to extract the GFFs. The statistical errors for the GFFs are obtained from a jackknife analysis.

III. LATTICE SIMULATION USING DOMAIN-WALL VALENCE QUARKS WITH STAGGERED SEA QUARKS

Since calculations at physical quark masses are prohibitively expensive with current algorithms and machines, we have used dynamical quark configurations at the lightest masses available, and where feasible, have used chiral perturbation theory to extrapolate to the physical mass. Staggered sea quarks with the Asqtad improved action were chosen because the computational economy of staggered quarks enabled the MILC Collaboration to generate large samples of configurations at low masses on large spatial volumes [25,26], which they freely made available to the lattice community.

Chiral symmetry is crucial for avoiding some operator mixing, convenient for operator renormalization, and valuable for chiral extrapolation. Furthermore, the four tastes associated with staggered fermions immensely complicate calculating operator matrix elements in nucleon states. Hence, we chose a hybrid action utilizing chirally symmetric valence domain-wall fermions (DWF) on an improved staggered fermion sea. Although this hybrid scheme breaks unitarity at finite lattice spacing, given the arguments that the valence and sea actions separately approach the physical continuum limit [27], we expect that the hybrid action also approaches the physical continuum limit. Furthermore, partially quenched mixed action chiral perturbation theory calculations are now becoming available for quantitative control of the continuum limit. We also note that hybrid actions have been successfully used in other contexts where, for example, the NRQCD action for valence quarks was combined with improved staggered sea quarks [28] and was successful in predicting mass splitting in heavy quark systems.

In our calculation, we used MILC configurations [29] both from the NERSC archive and provided directly by the collaboration. We then applied HYP-smearing [30] and bisected the lattice in the time direction. We have chosen gauge fields separated by 6 trajectories. Furthermore, we alternate between the first temporal half (time slices 0 to 31) and the second temporal half (time slices 32 to 63) on successive gauge configurations. In these samples we did not find residual autocorrelations. The scale is set by the

lattice spacing $a = 0.1241$ fm determined from heavy quark spectroscopy [31] with an uncertainty of 2%.

Domain-wall fermions [32–34] introduce an additional fifth dimension, L_5 . They preserve the Ward-Takahashi identity [35] even at finite lattice spacing in the limit $L_5 \rightarrow \infty$. At finite values of L_5 a residual explicit breaking of chiral symmetry is still present which can be parametrized by an additional mass term in the Ward-Takahashi identity [36,37]. In our calculations, we have kept this additional mass, $(am)_{\text{res}}$, at least an order of magnitude smaller than the quark mass, $(am)_q^{\text{DWF}}$ [19]. To the extent that $(am)_{\text{res}}$ is negligible, perturbative renormalization of $\mathcal{O}_{[\gamma_5]}$ is independent of γ_5 in the chiral limit and the nonperturbative renormalization of quark bilinear currents yields the same renormalization coefficients for the axial and the vector currents in the chiral limit [38].

We now consider the parameters entering the DWF action. The domain-wall action realizes chiral symmetry by producing right-handed states on one domain wall that decay exponentially away from the wall and exponentially decaying left-handed states on the other wall. To the extent that no low eigenmodes associated with dislocations (or rough fields) destroy the exponential decay and that the fifth dimension L_5 is large enough, chiral symmetry will be nearly exact and $(am)_{\text{res}}$ will be small. HYP-smearing was essential to reduce the effect of low eigenmodes, but it is still necessary to use spectral flow to determine a value of the domain-wall mass, M , for which the density of low eigenmodes is as small as possible. This was done on an ensemble of test configurations, with the result that we use $M = 1.7$. As discussed below, L_5 was then tuned to keep $(am)_{\text{res}}$ below 10% of the quark mass and to have negligible effect on our lattice observables. Finally, the quark mass was tuned to produce a pion mass equal to the Goldstone pion mass for the corresponding MILC configurations.

A. Tuning the fifth dimension

The extent of the fifth dimension, L_5 , has been adjusted such that the residual mass, $(am)_{\text{res}}$, is at least an order of magnitude smaller than the quark mass itself. This tuning is most relevant at the lightest quark mass since in that case the computational cost is largest and thus our tuning should be optimal. In addition, the breaking of chiral symmetry is also expected to be the largest and the resulting L_5 provides a minimum value needed for our calculations at the higher masses. The residual explicit chiral symmetry breaking characterized by $(am)_{\text{res}}$ is obtained from [36]

$$\Delta^\mu \mathcal{A}_\mu^a = 2m_q J_q^a(x) + 2J_{5q}^a(x), \quad (15)$$

where

$$J_{5q}^a(x) \approx m_{\text{res}} J_5^a(x), \quad (16)$$

which holds up to $\mathcal{O}(a^2)$.

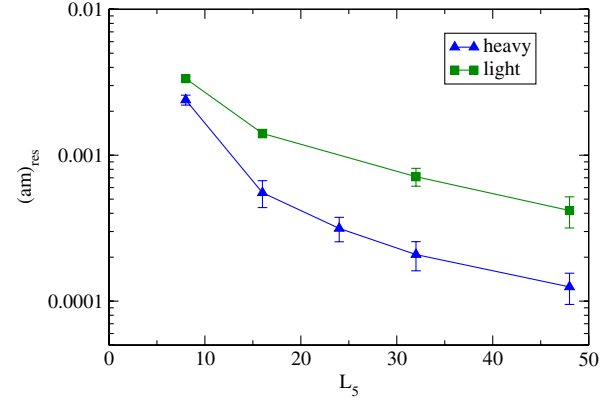


FIG. 3 (color online). Residual quark mass as a function of L_5 for the two samples (heavy and light) of 25 configurations each.

We have run simulations using two samples of 25 configurations with volume $\Omega = 20^3 \times 32$: three degenerate dynamical Asqtad quarks with bare masses $(am)_q^{\text{Asqtad,sea}} = 0.050$ (denoted as “heavy” and corresponding to $m_\pi \sim 760$ MeV) and two plus one quarks with masses $(am)_q^{\text{Asqtad,sea}} = 0.010, 0.050$ (termed “light” and corresponding to $m_\pi \sim 350$ MeV). The corresponding bare DWF masses have been adjusted to $(am)_q^{\text{DWF}} = 0.0810$ and 0.0138 for the heavy and light cases, respectively, cf. Sec. III B.

The resulting residual masses obtained from Eqs. (15) and (16) are plotted in Fig. 3. In the light quark case, $L_5 = 16$ just fulfills our requirement, while in the heavy quark case $L_5 = 16$ more than satisfies it. This confirms our expectation that the value of L_5 chosen at the lightest quark mass sets the lower limit for the other masses as well.

One quantitative check that $L_5 = 16$ is adequate is provided by the dependence of masses on L_5 as shown in Figs. 4–7. The leading effect of m_{res} is to shift the quark mass, so that when L_5 is sufficiently large this is the only effect, $m_\pi^2 \propto (m_q + m_{\text{res}})$. Figures 4 and 5 show the differ-

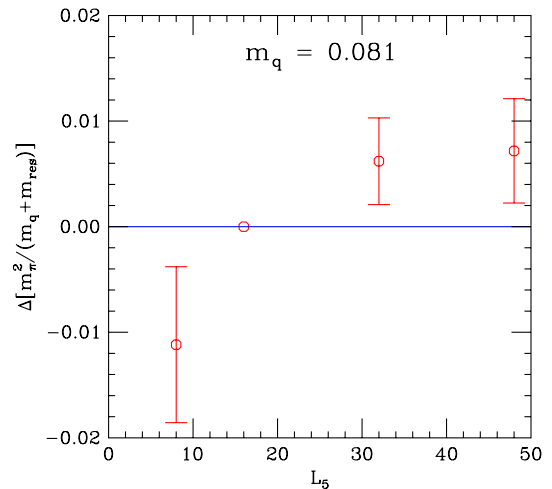


FIG. 4 (color online). Dependence of the pion mass on the extent of the fifth dimension L_5 for heavy quarks.

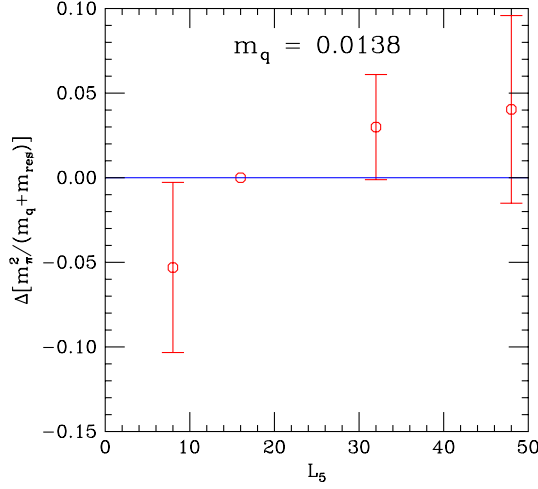


FIG. 5 (color online). Dependence of the pion mass on the extent of the fifth dimension L_5 for light quarks.

ence in the ratio $m_\pi^2/(m_q + m_{\text{res}})$ at a general value of L_5 and at $L_5 = 16$, and indicate that the difference is essentially consistent with zero for $L_5 > 16$. We expect the shifts in the nucleon mass induced by these small shifts in the pion mass to be negligible, and indeed, Figs. 6 and 7 show that the differences between the nucleon mass at a general value of L_5 and at $L_5 = 16$ are consistent with zero for $L_5 > 16$. Hence, we choose $L_5 = 16$ to be a good compromise between accuracy and performance.

B. Tuning the quark mass

We define the light quark masses in our hybrid theory by matching the pion mass in two calculations: (i) using two plus one flavors of dynamical Asqtad sea fermions and Asqtad valence fermions [29] and (ii) using the pion mass in our hybrid calculation with Asqtad dynamical sea fermions and valence domain-wall fermions with $L_5 = 16$. Because of the four tastes and correspondingly 16 light

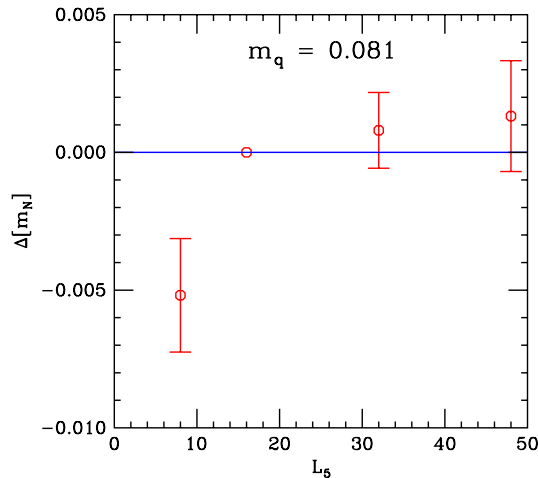


FIG. 6 (color online). Dependence of the nucleon mass on the extent of the fifth dimension L_5 for heavy quarks.

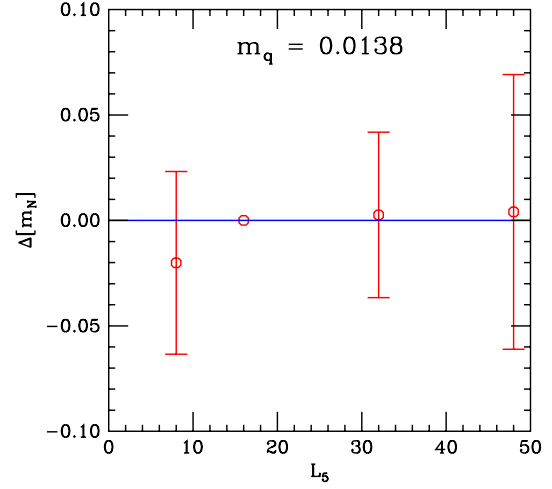


FIG. 7 (color online). Dependence of the nucleon mass on the extent of the fifth dimension L_5 for light quarks.

pseudoscalar mesons in the staggered theory, it is necessary to choose between matching the lightest pseudoscalar mass, corresponding to the Goldstone pion of the theory, or some appropriately defined average. In this work, we have chosen to match the Goldstone pion, and the results of tuning the domain-wall quark mass such that the domain-wall pion mass agrees within 1% with the Asqtad Goldstone pion mass are shown in Table I. The substantial difference between the bare quark masses for Asqtad and DWF valence quarks reflects the significant difference in renormalization for the two actions. An observable physical difference is the fact that once the DWF quark masses have been adjusted to fit the Asqtad Goldstone pion masses, the DWF nucleon masses are approximately 6% lower than the corresponding Asqtad nucleon masses. We attribute this to the range of pseudoscalar masses in the staggered theory and note that had we used a heavier quark mass so that the DWF pion fit some appropriately weighted average of the staggered pion masses, then the DWF nucleon would have been heavier.

C. Operator renormalization

The quark bilinear operators in Eq. (4) are renormalized using a combination of one-loop perturbation theory and nonperturbative renormalization of the axial vector current.

Our lattice calculations using lattice regularization with cutoff $1/a$ are related to physical observables at scale μ^2 in the $\overline{\text{MS}}$ renormalization scheme in 1-loop perturbation theory by

$$\begin{aligned} \mathcal{O}_i^{\overline{\text{MS}}}(\mu^2) &= \sum_j \left(\delta_{ij} + \frac{g_0^2}{16\pi^2} \frac{N_c^2 - 1}{2N_c} (\gamma_{ij}^{\overline{\text{MS}}} \log(\mu^2 a^2) \right. \\ &\quad \left. - (B_{ij}^{\text{LATT}} - B_{ij}^{\overline{\text{MS}}})) \right) \cdot \mathcal{O}_j^{\text{LATT}}(a^2) \\ &= Z_{ij}^{\mathcal{O}} \cdot \mathcal{O}_j^{\text{LATT}}(a^2), \end{aligned} \quad (17)$$

TABLE I. The lattice volume Ω and number of configurations used for the DWF calculations and a comparison of the quark, pion, and nucleon masses in the DWF and Asqtad calculations as described in the text.

Dataset	Ω	#	$(am)_q^{\text{Asqtad}}$	$(am)_q^{\text{DWF}}$	$(am)_\pi^{\text{Asqtad}}$	$(am)_\pi^{\text{DWF}}$	$(am)_N^{\text{Asqtad}}$	$(am)_N^{\text{DWF}}$	m_π^{DWF} [MeV]
1	$20^3 \times 32$	425	0.050/0.050	0.0810	0.4836(2)	0.4773(9)	1.057(5)	0.986(5)	758.9(1.4)
2		350	0.040/0.050	0.0478	0.4340(3)	0.4293(10)	1.003(3)	0.938(8)	682.6(1.6)
3		564	0.030/0.050	0.0644	0.3774(2)	0.3747(10)	0.930(3)	0.869(6)	595.8(1.6)
4		486	0.020/0.050	0.0313	0.3109(2)	0.3121(11)	0.854(3)	0.814(7)	496.2(1.7)
5		655	0.010/0.050	0.0138	0.2242(2)	0.2243(10)	0.779(6)	0.730(12)	356.6(1.6)
6	$28^3 \times 32$	270	0.010/0.050	0.0138		0.2220(9)		0.766(15)	352.3(1.4)

where the anomalous dimensions γ_{ij} and the finite constants B_{ij} have been calculated for domain-wall fermions with HYP-smearing in Refs. [39,40]. Because the renormalization factors for operators with and without γ_5 are identical at quark mass zero, we use mass independent renormalization with all renormalization constants defined at quark mass zero. The renormalization factors $Z_{ij}^{\mathcal{O}}$ for domain-wall mass $M = 1.7$ used in this work are tabulated in Table II, using the results for the one-loop coupling constant $g^2/(12\pi^2) = 1/53.64$ from Refs. [39,40]. By virtue of the suppression of loop integrals by HYP-smearing, the ratio of the one-loop perturbative renormalization factor for a general bilinear operator to the renormalization factor for the axial current is within a few percent of unity, suggesting adequate convergence for this ratio at one-loop level. Since one element in the calculation common to all operators arising from the wave function renormalization in the fifth dimension is not small, it is desirable to determine this one common factor nonperturbatively. This is accomplished using the fact that the renormalization factor, Z_A , for the 4-dimensional axial current operator $A_\mu = \bar{q}\gamma_\mu\gamma_5q$ may be calculated using the 5-dimensional conserved axial current for domain-wall fermions \mathcal{A}_μ by the relation [36] $\langle \mathcal{A}_\mu(t)A_\mu(0) \rangle = Z_A \langle A_\mu(t)A_\mu(0) \rangle$. Hence the complete renormalization factor is written as the exact axial current renormalization factor times the ratio of the perturbative renormalization factor for the desired operator divided by the perturbative renormalization factor for the axial current. That is,

$$Z^{\mathcal{O}} = \frac{Z^{\mathcal{O},\text{pert}}}{Z_A^{\text{pert}}} \cdot Z_A^{\text{nonpert}}. \quad (18)$$

In the continuum, because of Lorentz invariance, the to-

 TABLE II. Perturbative 1-loop lattice renormalization constants for the $\overline{\text{MS}}$ scheme at a scale $\mu^2 = 1/a^2$.

Operator	$H(4)$	$Z^{\mathcal{O},\text{pert}}$
$\bar{q}[\gamma_5]\gamma_{\{\mu}D_{\nu\}}q$	$\tau_1^{(3)}$	0.962
$\bar{q}[\gamma_5]\gamma_{\{\mu}D_{\nu\}}q$	$\tau_1^{(6)}$	0.968
$\bar{q}[\gamma_5]\gamma_{\{\mu}D_{\nu}D_{\rho\}}q$	$\tau_2^{(4)}$	0.980
$\bar{q}[\gamma_5]\gamma_{\{\mu}D_{\nu}D_{\rho\}}q$	$\tau_1^{(8)}$	0.982

tally symmetric operator $\bar{q}[\gamma_5]\gamma_{\{\mu}D_{\nu}D_{\rho\}}q$ cannot mix with the mixed symmetry operator $\bar{q}[\gamma_5]\gamma_{[\mu}D_{\nu]}D_{\rho}q$, where the square brackets denote antisymmetrization. In contrast, on the lattice, both operators appear in the same representation, $\tau_1^{(8)}$, so that they can and do mix. However, the mixing coefficient [39,40], $Z_{ij}^{\mathcal{O}} = 2.88 \times 10^{-3}$, is very small, so that we have ignored the contribution of the mixed symmetry operator in this present work.

All results below have been transformed to a scale of $\mu^2 = 4 \text{ GeV}^2$.

IV. NUMERICAL RESULTS FOR THE GENERALIZED FORM FACTORS

Since two-point functions taken at the sink $\tau = \tau_{\text{snk}}$, $C^{2\text{pt}}(\tau_{\text{snk}}, P')$ and $C^{2\text{pt}}(\tau_{\text{snk}}, P)$ in the ratio Eq. (13) decay exponentially for the full Euclidean distance $\tau_{\text{snk}} - \tau_{\text{src}}$, they are particularly subject to statistical noise. In the worst case, they may become negative, which we observe for three values of the momentum transfer for the data set $m = 0.01, 20^3$. The corresponding data points are excluded from our analysis. Our numerical results for the complete set of unpolarized and polarized $n = 1, 2, 3$ isovector and isosinglet GFFs as functions of the momentum transfer squared are provided in Tables VI through XXIX in the Appendix.

In Figs. 8 and 9 we show results for the vector generalized form factors A_{20}, B_{20}, C_{20} and axial vector GFFs $\tilde{A}_{20}, \tilde{B}_{20}$ as functions of the momentum transfer squared t . We observe that the absolute values in the isovector and isosinglet channels are in qualitative agreement with the predictions from large N_c counting rules, see e.g. [41], for the unpolarized GFFs

$$\begin{aligned} |A_{20}^{u+d}| &\sim N_c^2 \gg |A_{20}^{u-d}| \sim N_c, \\ |B_{20}^{u-d}| &\sim N_c^3 \gg |B_{20}^{u+d}| \sim N_c^2, \\ |C_{20}^{u+d}| &\sim N_c^2 \gg |C_{20}^{u-d}| \sim N_c. \end{aligned} \quad (19)$$

In the polarized case, the inequalities from the counting rules are not satisfied nearly as strongly. Whereas the counting rules predict

$$\begin{aligned} |\tilde{A}_{20}^{u-d}| &\sim N_c^2 \gg |\tilde{A}_{20}^{u+d}| \sim N_c, \\ |\tilde{B}_{20}^{u-d}| &\sim N_c^4 \gg |\tilde{B}_{20}^{u+d}| \sim N_c^3, \end{aligned} \quad (20)$$

our results for \tilde{A}_{20}^{u-d} are only slightly larger than \tilde{A}_{20}^{u+d} , and although the errors are large, \tilde{B}_{20}^{u-d} appears to be comparable to \tilde{B}_{20}^{u+d} rather than dominating it. Finally, our results disagree with the predicted hierarchy between different types of GFFs:

$$|B_{20}^{u-d}| \sim N_c^3 \gg |A_{20}^{u+d}| \sim N_c^2, \quad (21)$$

since the lattice results (at nonzero t) clearly give $A_{20}^{u+d} > B_{20}^{u-d}$. It would be valuable to understand why these counting rules are only partially satisfied.

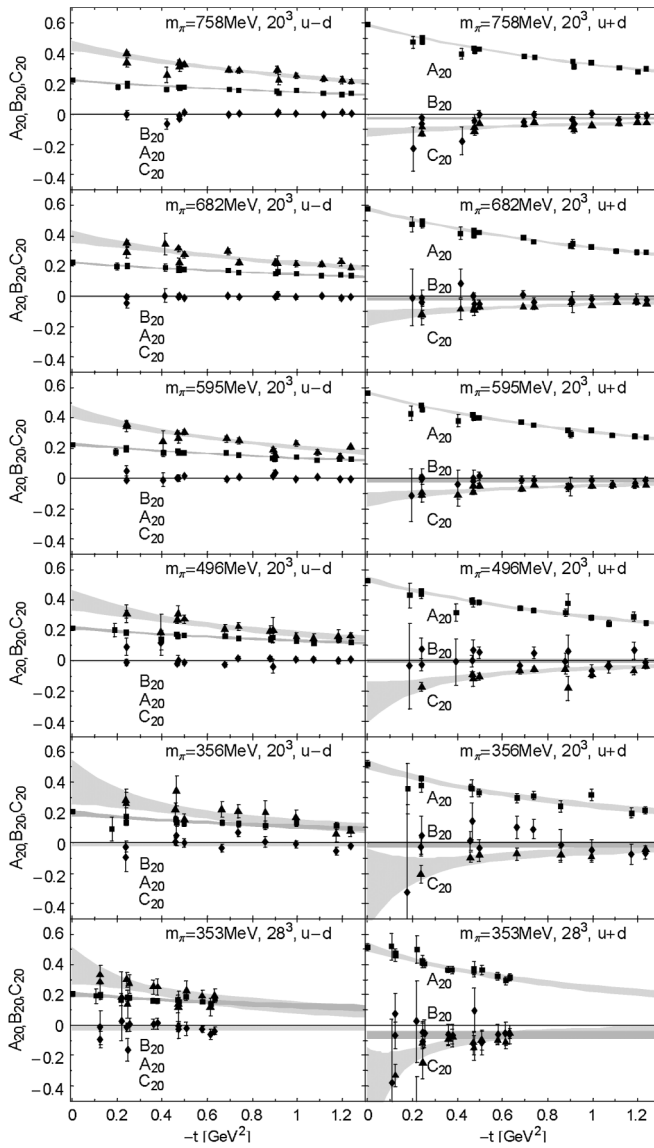


FIG. 8. Unpolarized (vector) generalized $n = 2$ form factors for the flavor combinations $u - d$ (left) and $u + d$ (right). Disconnected contributions are not included.

For future reference, it is important to note that the GFF C_{20} , which gives rise to the ξ -dependence of the $n = 2$ moment of the GPDs $H(x, \xi, t)$ and $E(x, \xi, t)$, is compatible with zero for $u - d$, over the full range of momentum transfer squared $t \approx -0.12 \dots -1.2 \text{ GeV}^2$. Similarly, the isosinglet GFF B_{20}^{u+d} , which is one of the terms in the contribution of the total angular momentum to the nucleon spin, is compatible with zero within errors. We will study both these GFFs in detail in Sec. V.

We now consider the behavior of the slopes of the GFFs A_{n0} and their relation to the transverse size of the nucleon. Since $\int_{-1}^1 dx x^{n-1} H(x, \xi = 0, t) = A_{n0}(t)$, it is evident that the GFFs for increasing n correspond to increasing average momentum fractions $\langle x \rangle$. As the average momentum fraction gets larger, or equivalently as $n \rightarrow \infty$, we expect the

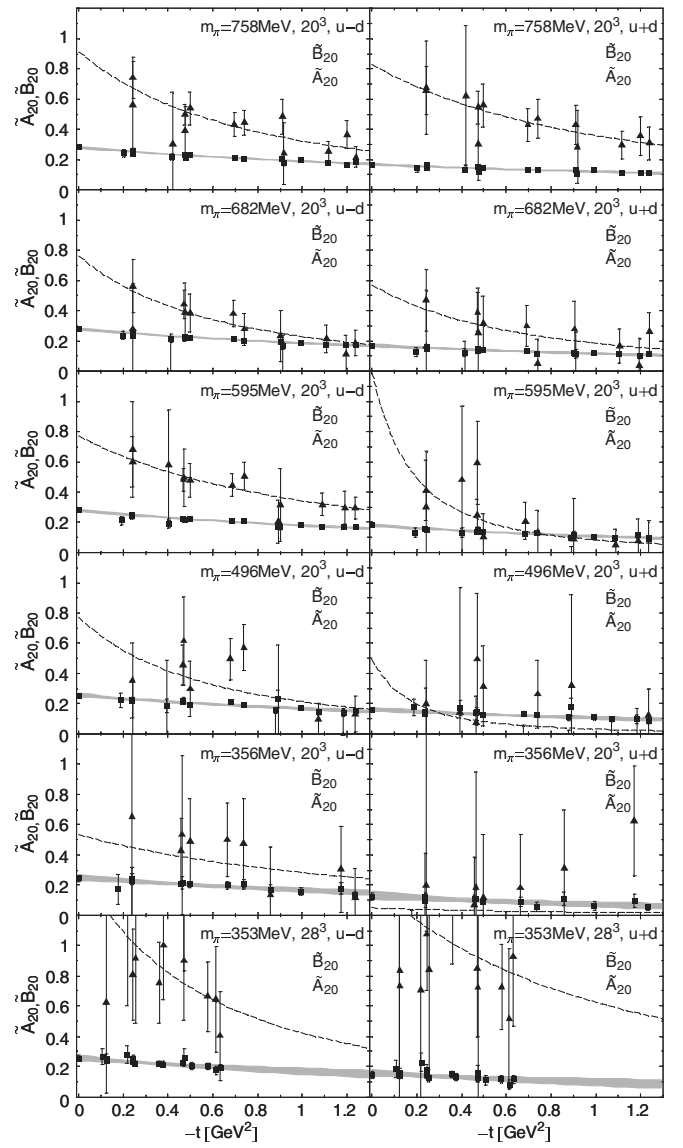


FIG. 9. Polarized (axial vector) generalized $n = 2$ form factors for the flavor combinations $u - d$ (left) and $u + d$ (right). Disconnected contributions are not included.

t -slope of the GFFs A_{n0} to flatten. This may be understood in terms of the light cone Fock representation [42,43] by the fact that the final state nucleon wave function for a struck quark with momentum fraction x and initial transverse momentum k_{\perp}^{in} depends on the transverse momentum $k_{\perp} = k_{\perp}^{\text{in}} - (1-x)\Delta_{\perp}$. Hence, a large transverse momentum transfer $t = -\Delta_{\perp}^2$ can be better absorbed without causing breakup of the bound state by quarks with large momentum fraction x . Additional insight is obtained by considering the impact parameter dependent GPD, $H(x, b_{\perp}^2)$, which has a probability interpretation and is the Fourier transform [6] with respect to transverse momentum transfer of $H(x, \xi = 0, t = -\Delta_{\perp}^2)$:

$$H(x, b_{\perp}^2) = \int \frac{d^2\Delta_{\perp}}{(2\pi)^2} e^{-ib_{\perp} \cdot \Delta_{\perp}} H(x, \xi = 0, t = -\Delta_{\perp}^2), \quad (22)$$

where Δ_{\perp} is the transverse momentum transfer. The impact parameter b_{\perp} corresponds to the distance of the active quark from the center of momentum of the nucleon. As $x \rightarrow 1$, a single quark will carry all the longitudinal momentum of the nucleon and therefore represent its center of momentum, so that the impact parameter distribution in this limit is strongly peaked around the origin, $H(x \rightarrow 1, b_{\perp}^2) \propto \delta^2(b_{\perp}^2)$. The corresponding flattening of the GFFs in the momentum transfer t is clearly visible in Fig. 10, where we compare the slopes of the GFFs $A_{(n=1,2,3)0}$ which have been normalized to unity at $t = 0$.

Dipole fits to the GFFs in Fig. 10, denoted by the solid lines and statistical error bands, enable us to determine the slopes of the form factors and thus express the 2- and 3-dimensional rms radii $\langle r_{\perp}^2 \rangle_{\perp}^{1/2}$ and $\langle r^2 \rangle^{1/2}$ in terms of the dipole masses m_D

$$\langle r_{\perp}^2 \rangle = \frac{2}{3} \langle r^2 \rangle = \frac{8}{m_D^2}. \quad (23)$$

Since the range of values for the momentum transfer t is much smaller for the large volume ($L^3 = 28^3$) data set, we have restricted the dipole fits for all data sets to the overlapping region of $t = 0 \dots -0.8 \text{ GeV}^2$. Our results for the 2-dimensional rms radii versus the pion mass squared are presented in Figs. 11 and 12. These results confirm the dramatic dependence of the transverse rms radius on the moment and thus the average momentum fraction as first observed [14] for pion masses 750 MeV and higher, and show that this dependence increases as the pion mass decreases. Indeed, considering the ratio of the $n = 3$ moment to the $n = 1$ moment, which both correspond to the same sum or difference of quarks and antiquarks, we observe that for vector GFFs this ratio decreases from approximately 0.58 to 0.22 as the pion mass decreases from 750 MeV to 350 MeV, and for axial vector GFFs, it decreases from roughly 0.71 to 0.43.

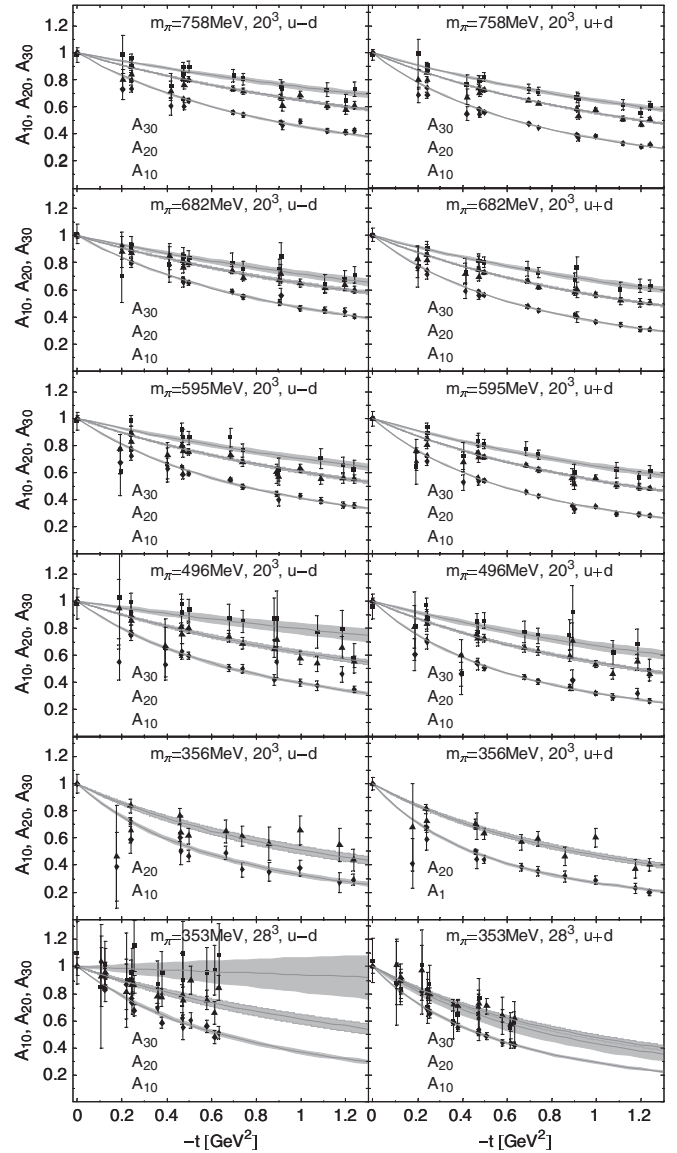


FIG. 10. Flattening of the slope of the A_{n0} GFFs with increasing n for flavor combinations $u - d$ (left) and $u + d$ (right). The solid curves and error bands correspond to dipole fits described in the text. Disconnected contributions are not included.

In Figs. 13 and 14 we present a first comparison of our results for ratios of generalized form factors $A_{30}(t)/A_{10}(t)$ and $\tilde{A}_{30}(t)/\tilde{A}_{10}(t)$ to the parametrization by Diehl *et al.* [11] as function of the momentum transfer squared t . As the pion mass decreases, the slope of our results approaches that of the phenomenological parametrization. Our results clearly indicate that a factorized ansatz for the GPDs in x and t , which would lead to constant ratios in Figs. 13 and 14 breaks down already for small values of the momentum transfer squared $|t| \ll 1 \text{ GeV}^2$.

The GFFs $A_{20}^q(t=0) = \langle x \rangle_q$ and $B_{20}^q(t=0)$ enable us to compute the total quark angular momentum contribution to the nucleon spin [5], $J^q = 1/2(A_{20}^q(0) + B_{20}^q(0))$. Figs. 15

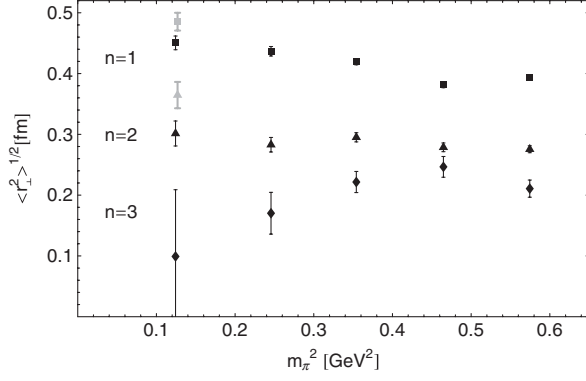


FIG. 11. Two-dimensional rms radii of the vector GFFs versus m_{π}^2 for the flavor combination $u - d$. The results for $m_{\pi} = 354$ MeV, $L^3 = 20^3$ are displayed in gray.

and 16 show results for the quark spin $\tilde{A}_{10}^q(t=0)/2 = \Delta\Sigma^q/2$ and the orbital angular momentum $L^q = J^q - \Delta\Sigma^q/2$ contributions to the nucleon spin $S = 1/2$ versus the pion mass squared. Preliminary chiral extrapolations of $\Delta\Sigma^q$ based on self-consistently improved one-loop chiral perturbation theory (ChPT) [44–48] for $\Delta\Sigma^{u+d}$ and ChPT including the Δ resonance [49,50] for $g_A = \Delta\Sigma^{u-d}$ are shown as shaded bands. The values for $B_{20}^q(t=0)$ have been obtained from a linear extrapolation of $B_{20}^{u+d}(t)$ and a dipole extrapolation for $B_{20}^{u,d}(t)$ in t . The resulting uncertainty in $B_{20}^q(t=0)$, which contributes to the uncertainty in L_q , depends on the details of the corresponding fit, such as the functional form and range of t , and is therefore partially systematic. To allow the reader to assess the absolute statistical errors, we represent the errors for L_q coming from the extrapolation in t by error bands around the m_{π}^2 -axis in Figs. 15 and 16. Experimental results for the quark spin fractions $\Delta\Sigma^{u+d}$ and $\Delta(u, d) = \Delta\Sigma^{u,d}$ are represented by open stars for the prediction given in the HERMES publication from 1999 [51] and filled stars for the 2007 HERMES re-

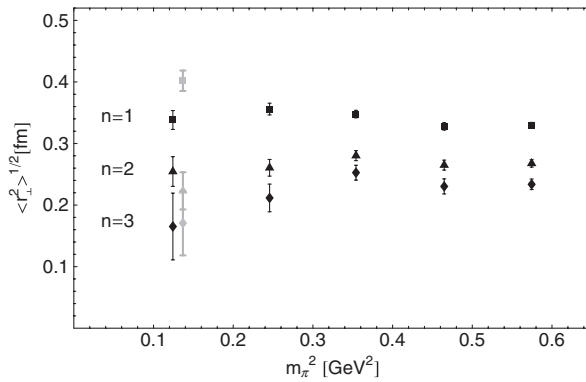


FIG. 12. Two-dimensional rms radii of the axial vector GFFs versus m_{π}^2 for the flavor combination $u - d$. The results for $m_{\pi} = 354$ MeV, $L^3 = 20^3$ are displayed in gray and slightly shifted to the right for clarity.

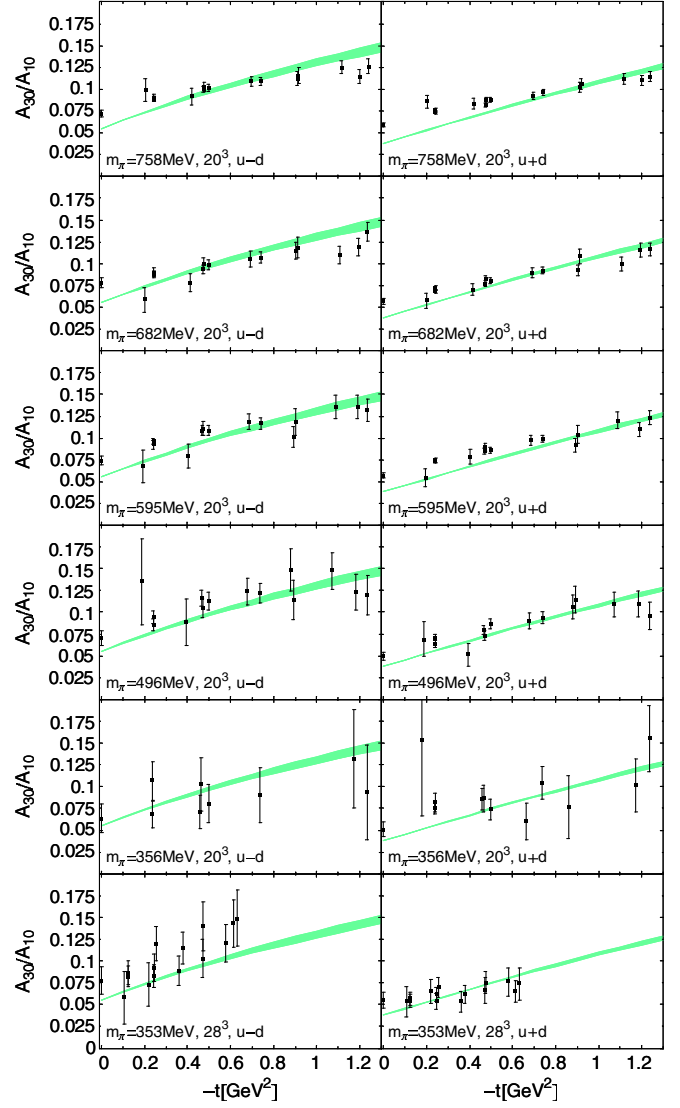


FIG. 13 (color online). Ratio of generalized form factors $A_{30}(t)/A_{10}(t)$ for the flavor combinations $u - d$ (left) and $u + d$ (right) compared with the parametrization in Ref. [11]. Disconnected contributions are not included.

sults [52]. The significant difference between the new HERMES results, which are consistent with recent COMPASS results [53], and the values given in [51] is probably to a large extent due to the simple Regge-parametrization which has been used in [51] to compute the contribution to $\Delta\Sigma$ coming from the low x -region. It is gratifying that the new values are much closer to our lattice results.

These results reveal two remarkable features of the quark contributions to the nucleon spin. The first is that the magnitude of the orbital angular momentum contributions of the up- and down-quarks, L^u and L^d , are separately quite substantial, starting at 0.15 at $m_{\pi} = 750$ MeV and increasing to nearly 0.20 at 350 MeV, and yet they cancel nearly completely at all pion masses. The second is the

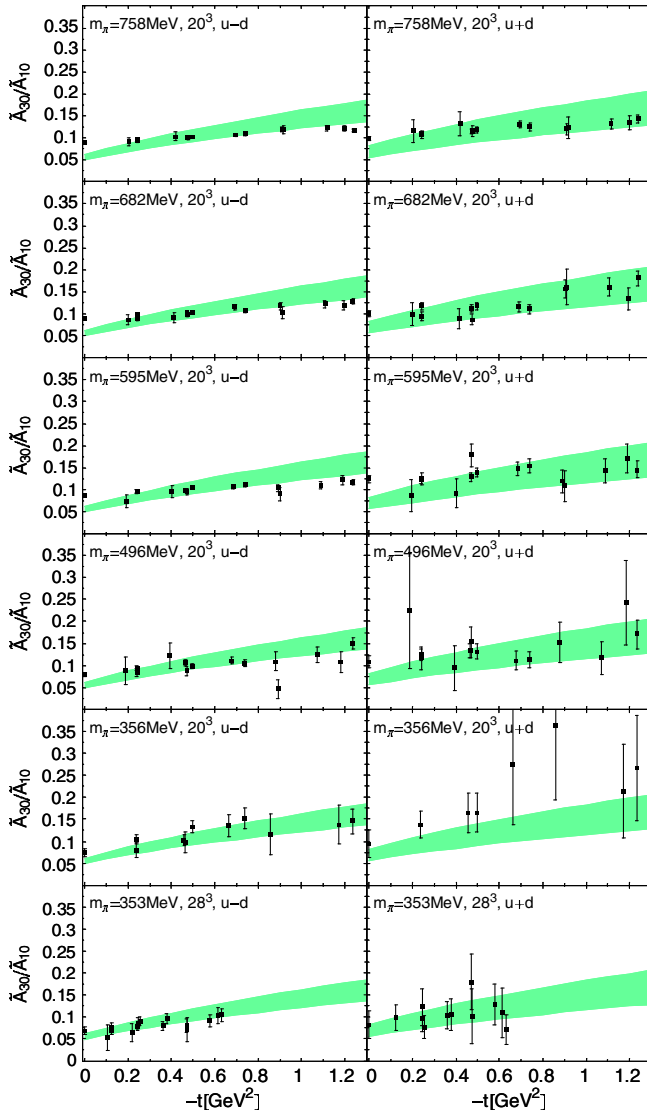


FIG. 14 (color online). Ratio of polarized generalized form factors $\tilde{A}_{30}(t)/\tilde{A}_{10}(t)$ for the flavor combinations $u - d$ (left) and $u + d$ (right) compared with the parametrization in Ref. [11]. Disconnected contributions are not included.

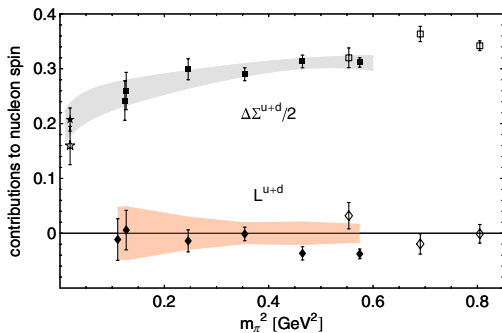


FIG. 15 (color online). Total quark spin and orbital angular momentum contributions to the spin of the nucleon. The filled and open stars represent values given in HERMES 2007 [52] and 1999 [51] respectively, and open symbols represent earlier LHPC/SESAM calculations. The error bands are explained in the text. Disconnected contributions are not included.

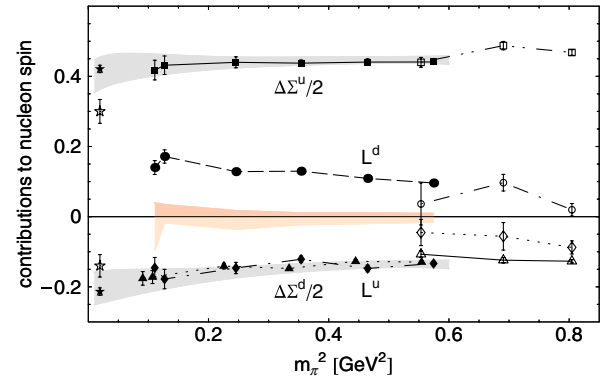


FIG. 16 (color online). Quark spin and orbital angular momentum contributions to the spin of the nucleon for up- and down-quarks. Squares and triangles denote $\Delta\Sigma^u$ and $\Delta\Sigma^d$ respectively, and diamonds and circles denote L^u and L^d respectively. The filled and open stars represent values given in HERMES 2007 [52] and 1999 [51] respectively and open symbols represent earlier LHPC/SESAM calculations. The error bands are explained in the text. Disconnected contributions are not included.

close cancellation between the orbital and spin contributions of the d quarks, L^d and $\Delta\Sigma^d/2$ for all pion masses. It would be valuable to understand the physical origin of both features.

V. CHIRAL EXTRAPOLATIONS

Our ultimate goal is to use the combination of full QCD lattice calculations in the chiral regime and chiral perturbation theory to extrapolate to the physical pion mass, to extrapolate to infinite volume, to extrapolate in momentum transfer, and to correct for lattice artifacts, with all the relevant low energy constants being determined solely from lattice data. Significant progress has been made in many aspects of chiral perturbation theory relevant to the nucleon observables addressed in this work [47,50,54–66]. Although important developments have been made in correcting for our hybrid action [61,67–70] and finite volume [50,60], results for the relevant GFFs are not yet available. In this work we will focus on ChPT treatment of the pion mass and momentum dependence.

The basic problem is that currently there is not yet unambiguous evidence supporting a particular counting scheme and its convergence criteria, leading to a range of alternative resummations, and there is similar ambiguity concerning the choice of degrees of freedom, such as when and if it is essential to include the Δ resonance. When complete results for the observables of interest are available, it will be interesting to compare four approaches: heavy baryon ChPT (HBChPT) [62–64], covariant ChPT in the baryon sector (CBChPT) [65], self-consistently improved one-loop ChPT [44–48], and ChPT with finite-range regulators [57,59,66]. Although self-consistent improvement by utilizing values of parameters like f_π and g_A

TABLE III. Low-energy constants used in the chiral extrapolations.

f_π^0 [GeV]	m_N^0 [GeV]	g_A^0	$\langle x \rangle_{u+d}^{\pi,0}$	c_1 [GeV $^{-1}$]	c_2 [GeV $^{-1}$]	c_3 [GeV $^{-1}$]	$g_{\pi N\Delta}^0$	$\Delta = m_\Delta^0 - m_N^0$ [GeV]
0.092	0.89	1.2	0.5	-0.9	3.2	-3.4	$3/(2^{3/2})g_A^0$	0.3

calculated on the lattice at the relevant pion mass and finite-range regulators appear to improve the behavior of ChPT at larger values of the pion mass, based on the results available in the literature, we will focus on the two formulations HBChPT and CBChPT.

Heavy baryon ChPT, which we will subsequently always refer to as HBChPT, assumes that m_π and the magnitude of the spatial three-momentum, p , are much smaller than the nucleon mass in the chiral limit, $m_N^0 \sim 890$ MeV, and the chiral scale $\Lambda_\chi = 4\pi f_\pi = 1.17$ GeV, and simultaneously expands in powers of the four quantities $\epsilon = \{\frac{p}{\Lambda_\chi}, \frac{m_\pi}{\Lambda_\chi}, \frac{p}{m_N^0}, \frac{m_\pi}{m_N^0}\}$. In contrast, covariant baryon ChPT, which, slightly changing the notation of Ref. [65], we will subsequently always refer to as CBChPT, does not treat m_N^0 and Λ_χ as comparable scales, but rather keeps all powers $(\frac{1}{m_N^0})^n$ generated by the couplings included in the ChPT Lagrangian. Thus, it is a resummation that includes terms that would contribute in higher order to HBChPT and may be thought of as recoil corrections. The HBChPT results of Refs. [62–64] and the CBChPT results of Ref. [65] have the desirable property that they use the same regularization scheme, so that truncation of the higher-order terms in CBChPT yields the corresponding result in HBChPT, a feature that we will utilize below. One of our primary objectives will be to assess the regimes of applicability of these two alternative formulations. For notational convenience, we will refer to the generic momentum in both theories as p , and order both theories in powers of p^n . We would like to note, however, that the counting scheme of the HBChPT-approaches in [62–64] differs from the one used in the CBChPT-approach of [65].

The HBChPT [62–64] and CBChPT [65] results for GFFs, including the dependence on the momentum transfer squared, t , enable us to investigate for the first time possible nontrivial correlations in the m_π - and t -dependence of GFFs. It is interesting to note that to order $\mathcal{O}(p^2)$ in HBChPT, unpolarized and polarized GFFs are independent of each other and depend on separate chiral limit values and counter terms. In contrast, in CBChPT, the pion-mass dependence of the isovector momentum fraction of quarks $\langle x \rangle_{u-d}$ is *simultaneously* controlled by both the chiral limit values $\langle x \rangle_{u-d}^0$ and $\langle x \rangle_{\Delta u-\Delta d}^0$, as is also the case for $\langle x \rangle_{\Delta u-\Delta d}$. To $\mathcal{O}(p^2)$, however, CBChPT does not include insertions from pion operators, and it turns out that the t -dependence for the isosinglet (and isovector) case to this order is therefore essentially linear and decouples from the pion-mass dependence. Once CBChPT calculations have been pushed to higher orders, it will be interesting to study the combined nonanalytic (t, m_π)-dependence of the full set of

polarized and unpolarized GFFs based on this approach. For the time being, we will investigate possible nontrivial correlations in m_π and t in the framework of covariant CBChPT by including partial $\mathcal{O}(p^3)$ -corrections as discussed below.

The low energy constants used for the chiral extrapolations are summarized in Table III. Ultimately, all these values will be determined simultaneously by a global fit to a full set of lattice calculations of all the relevant observables using the same lattice action, but at present they are chosen as follows. We will use $f_\pi^0 = 0.092$ GeV, $m_N^0 = 0.89$ GeV and $g_A^0 = 1.2$ as the chiral limit values of the pion decay constant, nucleon mass and the axial vector coupling constant, respectively, and for notational simplicity, will subsequently omit the upper index 0 for these quantities. We note that these values are compatible within statistical errors with hybrid lattice calculations of f_π , m_N , and g_A . In addition, we need the low energy constants c_1 , c_2 and c_3 for the chiral extrapolation of C_{20}^{u+d} in the framework of HBChPT in Sec. V J. Here, $c_2 = 3.2$ GeV $^{-1}$ and $c_3 = -3.4$ GeV $^{-1}$ are taken from Refs. [65,71] and $c_1 = -0.90$ GeV $^{-1}$ has been obtained from a CBChPT fit to our nucleon mass lattice data, which provides us with a parametrization for the pion-mass dependence of the nucleon mass in our simulation needed for some of the chiral extrapolations below. Depending on the order of ChPT, diagrams with insertions of pion operators contribute for the isosinglet GFFs, introducing the momentum fraction of quarks in the pion in the chiral limit, $\langle x \rangle_{u+d}^{\pi,0}$, as an additional low energy constant. Ultimately, we will calculate this quantity from chiral fits to hybrid lattice results for the pion, but for now we use $\langle x \rangle_{u+d}^{\pi,0} = 0.5$ [72–74], which is obtained from lattice calculations that are in reasonable agreement with phenomenology [75–77]. Finally, for the chiral extrapolation of the total quark angular momentum in the framework of HBChPT including the Δ -resonance, we use the nucleon- Δ mass splitting $\Delta = 0.3$ GeV, which is consistent with lattice calculations and the large- N_c relation $g_{\pi N\Delta}^0 = 3/(2^{3/2})g_A^0$ for the pion-nucleon- Δ coupling $g_{\pi N\Delta}$. This latter result will soon be superseded by extrapolation of lattice calculations of the $N - \Delta$ transition form factor [78–80].

Our chiral extrapolations are organized as follows, and summarized in Table IV. We begin in Sec. V A with a comparison of CBChPT and HBChPT extrapolations of the isovector GFF $A_{20}^{u-d}(t)$ and show that whereas CBChPT yields a satisfactory fit over the range of pion masses used in the lattice calculations, HBChPT only produces fits to the lowest few points. Hence, in

TABLE IV. Overview of different approaches to the (m_π, t) -dependence of GFFs in ChPT studied in Secs. VA, VB, VC, VD, VE, VF, VG, VH, VI, VJ, and VK.

Section	GFF	HBChPT	CBChPT	Expected dependence on m_π, t
A	A_{20}^{u-d}	$\mathcal{O}(p^2)$	$\mathcal{O}(p^2)$	Nonanalytic in m_π , \approx linear in t
B	B_{20}^{u-d}		$\mathcal{O}(p^2) + \text{corr. of } \mathcal{O}(p^3)$	Nonanalytic in m_π , \approx linear in t
C	C_{20}^{u-d}		$\mathcal{O}(p^2) + \text{corr. of } \mathcal{O}(p^3)$	Nonanalytic in m_π , \approx linear in t
D	A_{20}^{u+d}		$\mathcal{O}(p^2) + \text{corr. of } \mathcal{O}(p^3)$	Nonanalytic in m_π and t
I, E	B_{20}^{u+d}	$\mathcal{O}(p^2)$	$\mathcal{O}(p^2) + \mathcal{O}(p^3) - \text{CTs}$	Nonanalytic in m_π and t
F	C_{20}^{u+d}		$\mathcal{O}(p^2) + \text{corr. of } \mathcal{O}(p^{3,4})$	Nonanalytic in m_π and t
G	$J^{u+d} = 1/2(A + B)_{20}^{u+d}$		$\mathcal{O}(p^2) + \text{corr. of } \mathcal{O}(p^3)$	
H	$E_{20}^{u+d} = (A + t/(4m_N)^2 B)_{20}^{u+d}$	$\mathcal{O}(p^2)$		Linear in m_π^2 and t
H	$M_{20}^{u+d} = (A + B)_{20}^{u+d}$	$\mathcal{O}(p^2)$		Nonanalytic in m_π and t
J	C_{20}^{u+d}	$\mathcal{O}(p^2)$		Nonanalytic in m_π and t
K	$J^{u+d} = 1/2(A + B)_{20}^{u+d}$	$\mathcal{O}(p^2)$		
K	$J^{u+d} = 1/2(A + B)_{20}^{u+d}$	$\mathcal{O}(p^2)$ with Δ		

Secs. VB through VF, we study the pion mass and t -dependence of the isovector GFFs B_{20}^{u-d} and C_{20}^{u-d} and of the isoscalar GFFs A_{20}^{u+d} , B_{20}^{u+d} and C_{20}^{u+d} . This is followed in Sec. VG by a discussion of our results for the angular momentum of quarks, based on the CBChPT extrapolations for $A_{20}(t=0)$ and $B_{20}(t=0)$. In the counting scheme of [62–64] insertions of pion operators occur at $\mathcal{O}(p^2)$ in HBChPT, leading to a nonanalytic combined dependence on m_π and t for the GFFs $B_{20}^{u+d}(t)$ and $C_{20}^{u+d}(t)$, which we study in Secs. VH, VI, and VJ. Finally, in Sec. VK, we study the pion-mass dependence of the total quark angular momentum J_q in HBChPT, both including [55] and excluding explicit Δ degrees of freedom and compare with the corresponding CBChPT results. The chiral extrapolations of $B_{20}^{u+d}(t)$ and $C_{20}^{u+d}(t)$ in Secs. VF, VI, and VJ are the first parametrizations of their combined (m_π, t) -dependence, providing valuable insights into non-trivial correlations of m_π and t . Although we have a considerable amount of lattice data available for reasonably small values of $|t| \leq 0.25 \text{ GeV}^2$ and $m_\pi \leq 500 \text{ MeV}$, we use an extended set of results for $|t| < 0.48 \text{ GeV}^2$, $m_\pi < 700 \text{ MeV}$ in most of the fits to improve the statistics.

A. CBChPT extrapolation of $A_{20}^{u-d}(t)$

The $\mathcal{O}(p^2)$ CBChPT result [65] for the isovector GFF $A_{20}^{u-d}(t)$ is

$$\begin{aligned}
 A_{20}^{u-d}(t, m_\pi) = & A_{20}^{0,u-d} \left(f_A^{u-d}(m_\pi) + \frac{g_A^2}{192\pi^2 f_\pi^2} h_A(t, m_\pi) \right) \\
 & + \tilde{A}_{20}^{0,u-d} j_A^{u-d}(m_\pi) + A_{20}^{m_\pi, u-d} m_\pi^2 \\
 & + A_{20}^{t, u-d} t,
 \end{aligned} \tag{24}$$

where $f_A^{u-d}(m_\pi)$, $h_A(t, m_\pi)$ and $j_A^{u-d}(m_\pi)$ contain the non-analytic dependence on the pion mass and momentum transfer squared and $A_{20}^{0,u-d} \equiv A_{20}^{u-d}(t=0, m_\pi=0)$. Because of the small prefactor, the term $\propto h_A(t, m_\pi)$ is of $\mathcal{O}(10^{-3})$ for $m_\pi \leq 700 \text{ MeV}$, $|t| < 1 \text{ GeV}^2$ and therefore

numerically negligible. Thus, there are essentially no correlations of t and m_π present, and the dependence on t is only due to the counter term ($A_{20}^{t, u-d} t$). We use the value $\tilde{A}_{20}^{0,u-d} = 0.17$ obtained from a chiral fit to our lattice results for $\tilde{A}_{20}^{u-d}(t=0) = \langle x \rangle_{\Delta u - \Delta d}$ [47]. Since the low energy constant $A_{20}^{0,u-d}$ is a common parameter in the CBChPT formulae for the GFFs A_{20}^{u-d} , B_{20}^{u-d} and C_{20}^{u-d} , we performed a simultaneous fit based on Eq. (24) (for A_{20}^{u-d}), Eq. (25) (for B_{20}^{u-d}) and Eq. (26) (for C_{20}^{u-d}) with a total of 9 (1 common and 8 separate) fit parameters to over 120 lattice data points. The details of the CBChPT extrapolations and the results for the GFFs B_{20}^{u-d} and C_{20}^{u-d} will be discussed below in Secs. VB and VC, respectively. We find $A_{20}^{0,u-d} = 0.133(9)$ and $\langle x \rangle_{u-d} = A_{20}^{u-d}(t=0, m_{\pi, \text{phys}}) = 0.157(10)$ at the physical point. This is in very good agreement with phenomenological results from CTEQ and MRST [81] PDF parametrizations,

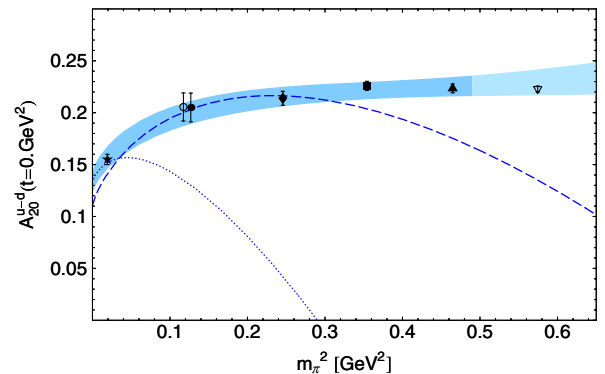


FIG. 17 (color online). Lattice results for A_{20}^{u-d} at $t = 0 \text{ GeV}^2$ versus m_π^2 . The error band is the result of a global simultaneous chiral fit using Eqs. (24)–(26). The phenomenological result from CTEQ6 is indicated by the star. The heavy-baryon-limit of the CBChPT fit is shown by the dotted line, and a HBChPT fit to the lattice data for $|t| < 0.3 \text{ GeV}^2$ and $m_\pi < 0.5 \text{ GeV}$ is shown by the dashed line.

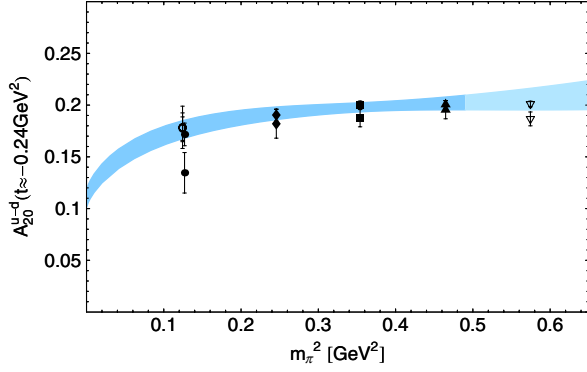


FIG. 18 (color online). Lattice results for A_{20}^{u-d} at $t \approx -0.24 \text{ GeV}^2$ versus m_π^2 together with the result of a global simultaneous chiral fit using Eqs. (24)–(26).

$\langle x \rangle_{u-d}^{\text{MRST2001}} = 0.157(5)$ and $\langle x \rangle_{u-d}^{\text{CTEQ6}} = 0.155(5)$. The results of the fit are shown in Figs. 17 and 18. The dependence of $A_{20}^{u-d}(t)$ on the momentum transfer squared is presented in Figs. 19 and 20, where we again obtain a good description of the lattice data.

To study the difference between HBChPT and CBChPT, we took the heavy-baryon-limit of CBChPT while keeping the same values of the fit parameters, and obtained the dotted line in Fig. 19. This curve only overlaps the CBChPT curve for $m_\pi < m_{\pi,\text{phys}}$ and drops off sharply for $m_\pi > m_{\pi,\text{phys}}$, indicating the quantitative importance of the truncated terms when using the coefficients from the CBChPT fit. In addition, it is important to ask the separate question of how well the lattice data can be fit with the HBChPT expression when the coefficients are determined directly by a best fit to the data. The dashed curve in Fig. 17 shows the result of fitting our lattice data for $|t| < 0.3 \text{ GeV}^2$ and $m_\pi < 0.5 \text{ GeV}$, and indicates that HBChPT describes the behavior of our lattice data over a significantly smaller range of pion masses than CBChPT.

Because limitations in computational resources presently require us to include lattice data extending to such

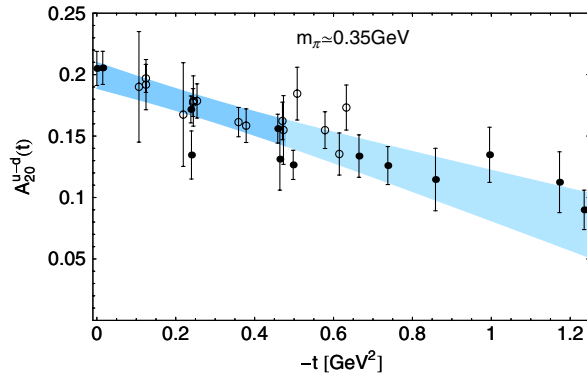


FIG. 19 (color online). Lattice results for $A_{20}^{u-d}(t)$ at $m_\pi \approx 0.35 \text{ GeV}$ together with the result of a global simultaneous chiral fit using Eqs. (24)–(26).

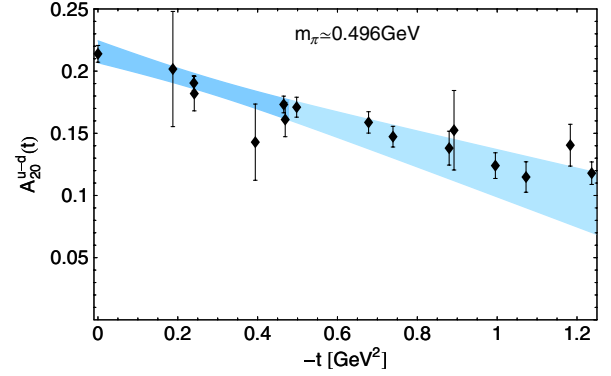


FIG. 20 (color online). Lattice results for $A_{20}^{u-d}(t)$ at $m_\pi \approx 0.496 \text{ GeV}$ together with the result of a global simultaneous chiral fit using Eqs. (24)–(26).

large pion masses, it would clearly be desirable to carry out a chiral perturbation theory analysis consistently including all terms of $\mathcal{O}(p^3)$. In the absence of the requisite full ChPT analysis, we have studied uncertainties in the chiral extrapolations by repeating the fit for different maximal values of the included pion masses. Figure 21 shows a comparison of the chiral extrapolations of A_{20}^{u-d} , based on fits to the lattice data in the regions $m_\pi < 500, 600, 685$ and 760 MeV . We find that the extrapolations to the chiral limit fully agree within statistical errors in all four cases. Note that the experimental point shown in Fig. 21 was not included in the fits, but each of the four analyses is consistent with it. This insensitivity to the upper mass cutoff shows that the strong bending towards the physical point is not driven by the large pion-mass region, where $\mathcal{O}(p^3)$ -corrections would be largest. Furthermore, all four chiral fits are, within statistical errors, in agreement with the lattice data points at large pion masses. This indicates that the present statistical error envelope is comparable to any systematic effects due to higher-order corrections.

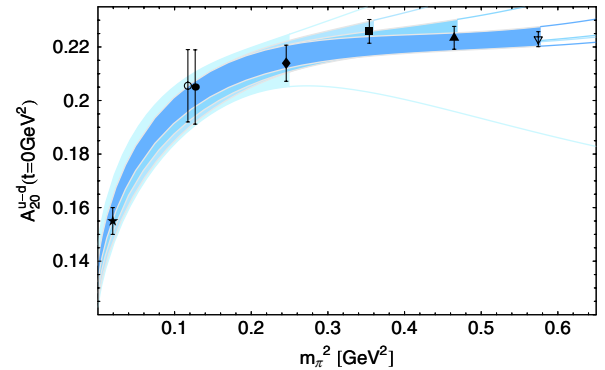


FIG. 21 (color online). Lattice results for A_{20}^{u-d} at $t = 0 \text{ GeV}^2$ versus m_π^2 together with chiral fits based on Eq. (24). The four different error bands represent chiral fits to lattice results including pion masses in the regions $m_\pi < 500, 600, 685$ and 760 MeV .

Another prescription to estimate $\mathcal{O}(p^3)$ -corrections that has been advocated in the literature, Ref. [65] is simply adding a single m_π^3 -term and, assuming both ‘‘naturalness’’ of the coefficient and the lack of other functional forms, seeing what error band arises from varying the coefficient from -1 to $+1$. Thus, to explore this possibility, following Ref. [65], we have added to the result in Eq. (24) the term $\delta_A^{(3),u-d} m_\pi^3 / (\Lambda_\chi^2 m_N^0)$, where $\Lambda_\chi \approx 1.2$ GeV is the chiral symmetry breaking scale, and varied the constant $\delta_A^{(3),u-d}$ in the range $-1, \dots, +1$. The results of fits to the lattice data for A_{20}^{u-d} including this additional term are shown in Fig. 22, where the error band corresponds to $\delta_A^{(3),u-d} = 0$, the dashed line corresponds to $\delta_A^{(3),u-d} = +1$ and the dotted line corresponds to $\delta_A^{(3),u-d} = -1$. From the figure, we note that this m_π^3 -term alone with coefficients $+1$ and -1 is clearly inconsistent with the behavior of the data. Theoretically, this is not unreasonable, since the foundation of the $\overline{\text{IR}}$ regularization scheme is a resummation of classes of terms, and here a single cubic term has been arbitrarily singled out. Analogous fits with similar qualitatively inconsistent behavior were also obtained for A_{20}^{u+d} , treated in a later section. Hence, although this prescription may provide useful estimates in other contexts, we do not believe it is useful in this work, and hence we do not include it in subsequent fits.

B. CBChPT extrapolation of $B_{20}^{u-d}(t)$

The $\mathcal{O}(p^2)$ CBChPT calculation [65] for the isovector B_{20} GFF gives

$$B_{20}^{u-d}(t, m_\pi) = \frac{m_N(m_\pi)}{m_N} B_{20}^{0,u-d} + A_{20}^{0,u-d} h_B^{u-d}(t, m_\pi) + \frac{m_N(m_\pi)}{m_N} \{ \delta_B^{t,u-d} t + \delta_B^{m_\pi,u-d} m_\pi^2 \}, \quad (25)$$

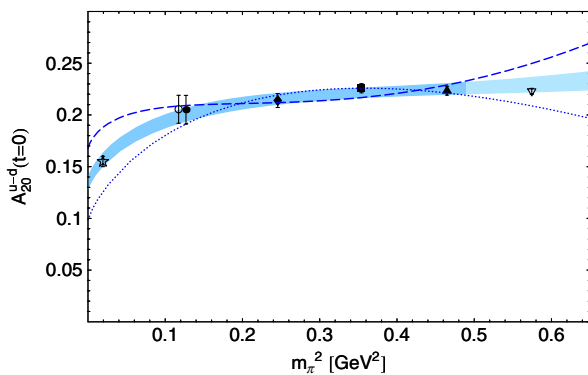


FIG. 22 (color online). Chiral fits including the terms in Eq. (24) plus an additional m_π^3 -term as described in the text. The narrow band is the original band omitting this term, the dashed line corresponds to $\delta_A^{(3),u-d} = 1$, and the dotted line to $\delta_A^{(3),u-d} = -1$.

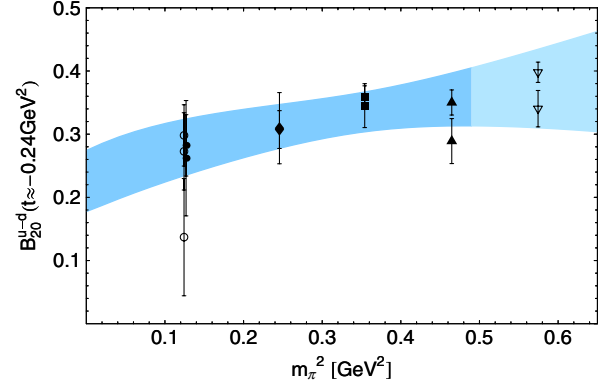


FIG. 23 (color online). Lattice results for B_{20}^{u-d} at $t \approx -0.24$ GeV² versus m_π^2 together with the result of a global simultaneous chiral fit using Eqs. (24)–(26).

where $m_N(m_\pi)$ is the pion-mass dependent nucleon mass, $B_{20}^{0,u-d} \equiv B_{20}^{u-d}(t=0, m_\pi=0)$, and where we have included estimates of $\mathcal{O}(p^3)$ -corrections in the form of $(\delta_B^{t,u-d} t)$ and $(\delta_B^{m_\pi,u-d} m_\pi^2)$. The low energy constants $B_{20}^{0,u-d}$, $\delta_B^{t,u-d}$ and $\delta_B^{m_\pi,u-d}$ are treated as free parameters and may be obtained from a fit to the lattice data. The nonanalytic dependence on m_π and t is given by $h_B^{u-d}(t, m_\pi)$, but it turns out that this function is approximately independent of t , $h_B^{u-d}(t, m_\pi) \approx h_B^{u-d}(m_\pi)$ for $m_\pi \leq 700$ MeV, $|t| < 1$ GeV². The t -dependence is therefore in practice linear due to the $\mathcal{O}(p^3)$ -correction term. For the m_π -dependent nucleon mass we use $\mathcal{O}(p^4)$ CBChPT [65,82] fitted to our lattice results for m_N . The chiral extrapolation of B_{20}^{u-d} is based on a global simultaneous fit as discussed in the previous section with $A_{20}^{0,u-d}$ as common fit parameter in Eqs. (24)–(26). We obtain $B_{20}^{0,u-d} = 0.263(62)$ and $B_{20}^{u-d}(t=0, m_{\pi,\text{phys}}) = 0.273(63)$ at the physical pion mass. Results of the fit are shown in Figs. 23 and 24.

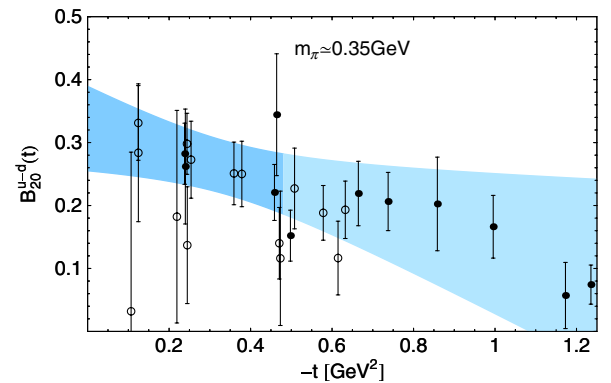


FIG. 24 (color online). Lattice results for $B_{20}^{u-d}(t)$ at $m_\pi \approx 350$ MeV versus $(-t)$ together with the result of a global simultaneous chiral fit using Eqs. (24)–(26).

C. CBChPT extrapolation of $C_{20}^{u-d}(t)$

The pion-mass dependence of the isovector GFF C_{20} in CBChPT to $\mathcal{O}(p^2)$ is very similar to that of the isovector B_{20} above and given by [65]

$$C_{20}^{u-d}(t, m_\pi) = \frac{m_N(m_\pi)}{m_N} C_{20}^{0,u-d} + A_{20}^{0,u-d} h_C^{u-d}(t, m_\pi) + \frac{m_N(m_\pi)}{m_N} \{ \delta_C^{t,u-d} t + \delta_C^{m_\pi, u-d} m_\pi^2 \}, \quad (26)$$

where $C_{20}^{0,u-d} \equiv C_{20}^{u-d}(t=0, m_\pi=0)$. As in the case of B_{20}^{u-d} , $(\delta_C^{t,u-d} t)$ and $(\delta_C^{m_\pi, u-d} m_\pi^2)$ represent $\mathcal{O}(p^3)$ -correction terms, and it turns out that $h_C^{u-d}(t, m_\pi)$ is practically independent of t . From a global simultaneous chiral fit based on Eqs. (24)–(26) with common fit parameter $A_{20}^{0,u-d}$ as discussed in Sec. VA, we obtain $C_{20}^{0,u-d} = -0.017(39)$ and $C_{20}^{u-d}(t=0, m_{\pi, \text{phys}}) = -0.017(41)$ at the physical point. The results are presented in Figs. 25 and 26. We note that $C_{20}^{u-d}(t)$ is roughly one order of magnitude smaller than $A_{20}^{u-d}(t)$ and $B_{20}^{u-d}(t)$ and fully compatible with zero within errors, $C_{20}^{u-d}(t) \approx 0$. This implies a rather mild dependence of the $n=2$ moment of the GPDs $H^{u-d}(x, \xi, t)$ and $E^{u-d}(x, \xi, t)$ on the longitudinal momentum transfer ξ (at least for small ξ), so that $H_{u-d}^{n=2}(\xi, t) \approx A_{20}^{u-d}(t)$ and $E_{u-d}^{n=2}(\xi, t) \approx B_{20}^{u-d}(t)$.

D. CBChPT extrapolation of $A_{20}^{u+d}(t)$

The (total) isosinglet momentum fraction of quarks, $A_{20}^{u+d}(t=0) = \langle x \rangle_{u+d}$ is not only an important hadron structure observable on its own but is in addition an essential ingredient for the computation of the total angular momentum contribution of quarks to the nucleon spin, $J^{u+d} = 1/2(A_{20}^{u+d}(0) + B_{20}^{u+d}(0))$. The combined (t, m_π) -dependence in CBChPT is given by [65]

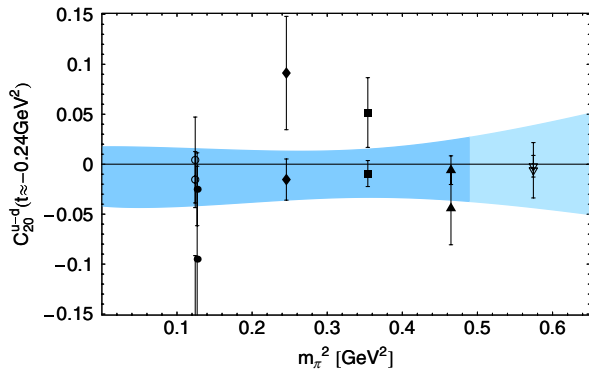


FIG. 25 (color online). Lattice results for C_{20}^{u-d} at $t \approx -0.24 \text{ GeV}^2$ versus m_π^2 together with the result of a global simultaneous chiral fit using Eqs. (24)–(26).

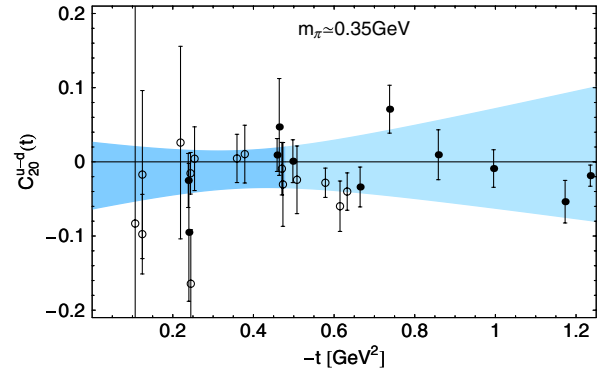


FIG. 26 (color online). Lattice results for $C_{20}^{u-d}(t)$ at $m_\pi \approx 350 \text{ MeV}$ versus $(-t)$ together with the result of a global simultaneous chiral fit using Eqs. (24)–(26).

$$A_{20}^{u+d}(t, m_\pi) = A_{20}^{0,u+d} \left(f_A^{u+d}(m_\pi) - \frac{g_A^2}{64\pi^2 f_\pi^2} h_A(t, m_\pi) \right) + A_{20}^{m_\pi, u+d} m_\pi^2 + A_{20}^{t, u+d} t + \Delta A_{20}^{u+d}(t, m_\pi) + \mathcal{O}(p^3), \quad (27)$$

where $A_{20}^{0,u+d} \equiv A_{20}^{u+d}(t=0, m_\pi=0)$, $f_A^{u+d}(m_\pi)$ and $h_A(t, m_\pi)$ contain the nonanalytic dependence on the pion mass and momentum transfer squared, and the constants $A_{20}^{m_\pi, u+d}$ and $A_{20}^{t, u+d}$ may be obtained from a fit to the lattice data. In this counting scheme, contributions from operator insertions in the pion line proportional to the momentum fraction of quarks in the pion in the chiral limit, $\langle x \rangle_{u+d}^{\pi, 0}$, are of order $\mathcal{O}(p^3)$. However, in order to see if such contributions could be relevant for the pion masses and values of the momentum transfer squared accessible in our calculation, we include the estimate of the $\mathcal{O}(p^3)$ -contribution ΔA_{20}^{u+d} provided in [65] in the fit to the lattice data points.

Similar to the isovector case discussed in the previous sections, the low energy constant $A_{20}^{0,u+d}$ is a common parameter in the chiral extrapolation formulae for the isosinglet GFFs A_{20}^{u+d} , B_{20}^{u+d} and C_{20}^{u+d} . Using $\langle x \rangle_{u+d}^{\pi, 0} = 0.5$ from Table III as an input parameter, we performed a simultaneous fit to over 120 lattice data points for these three GFFs, based on Eqs. (27)–(29), with 1 common and 8 separate low energy constants as fit parameters. For the details of the CBChPT results for B_{20}^{u+d} and C_{20}^{u+d} we refer to Secs. VE and VF below. The chiral fit gives $A_{20}^{0,u+d} = 0.524(25)$ and $\langle x \rangle_{u+d} = A_{20}^{u+d}(t=0, m_{\pi, \text{phys}}) = 0.520(24)$ at the physical point. Again, this is in very good agreement with phenomenological results from CTEQ and MRST [81] parametrizations, $\langle x \rangle_{u+d}^{\text{MRST2001}} = 0.538(22)$ and $\langle x \rangle_{u+d}^{\text{CTEQ6}} = 0.537(22)$. A variation of the input parameter $\langle x \rangle_{u+d}^{\pi, 0}$ by $\pm 10\%$ only leads to a small change in $A_{20}^{0,u+d}(t=0)$ of $\mathcal{O}(1\%)$, which is significantly smaller than the statistical error of $\approx 5\%$. The results of the fit are shown in Figs. 27 and 28. We would like to note that the slight upwards bending in Fig. 27 at low m_π , and therefore the

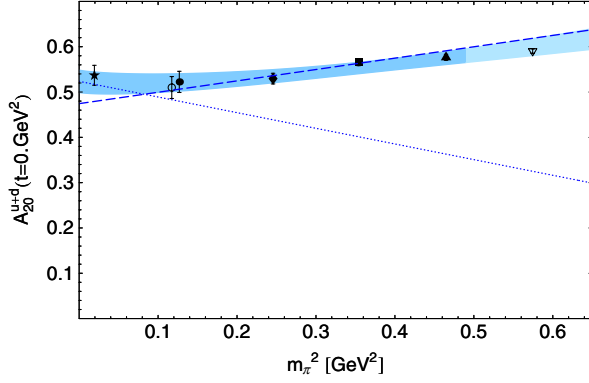


FIG. 27 (color online). Lattice results for A_{20}^{u+d} at $t = 0 \text{ GeV}^2$ versus m_{π}^2 . The error band is the result of a global simultaneous chiral fit using Eqs. (27)–(29). The phenomenological value from CTEQ6 is denoted by a star. The heavy-baryon-limit of the CBChPT fit is shown by the dotted line, and a HBChPT fit to the lattice data for $|t| < 0.3 \text{ GeV}^2$ and $m_{\pi} < 0.5 \text{ GeV}$ is shown by the dashed line.

good agreement with the phenomenological value, is due to the $\mathcal{O}(p^3)$ -contribution ΔA_{20}^{u+d} . It has to be seen if this somewhat unusual curvature persists once the full $\mathcal{O}(p^3)$ -contribution is available and fitted to the lattice results. The inclusion of contributions from disconnected diagrams could also require a different extrapolation in m_{π} . The dependence of $A_{20}^{u+d}(t)$ on t at fixed values of m_{π} is presented in Figs. 29 and 30.

As in the case of A^{u-d} , we also consider the heavy-baryon-limit of the CBChPT fit, giving the result $A_{20}^{u+d}(t = 0, m_{\pi}) = A_{20}^{0,u+d} + A_{20}^{m_{\pi},u+d} m_{\pi}^2$ represented by the dotted line in Fig. 27, which agrees with the CBChPT result only over a very limited range at low pion masses. Notably, while the lattice results for A_{20}^{u+d} are rising for larger pion masses, the heavy-baryon-limit curve has the opposite slope with negative $A_{20}^{m_{\pi},u+d}$. However, a direct HBChPT fit with free coefficients (see also Sec. VH) shown by the dashed curve leads to a positive $A_{20}^{m_{\pi},u+d}$ and a reasonable description of the lattice data points.

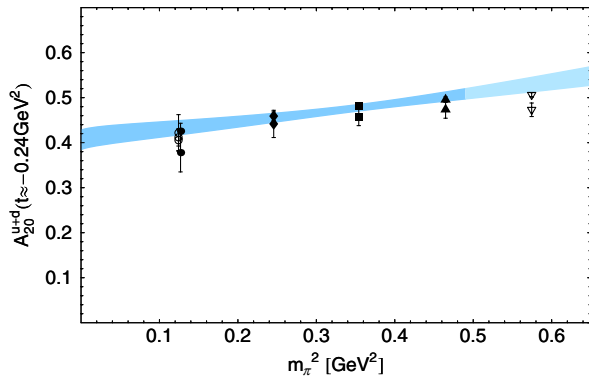


FIG. 28 (color online). Lattice results for $A_{20}^{u+d}(t)$ at $t \approx -0.24 \text{ GeV}^2$ versus m_{π}^2 together with the result of a global simultaneous chiral fit using Eqs. (27)–(29).

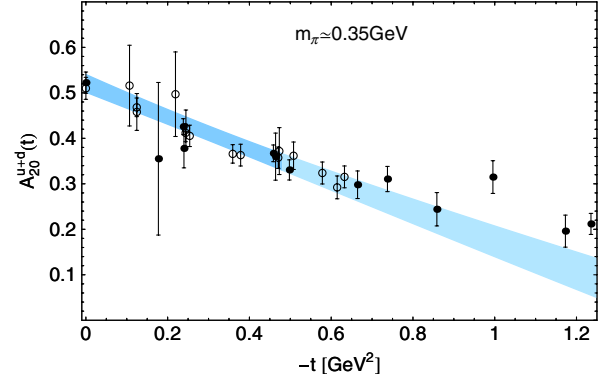


FIG. 29 (color online). Lattice results for $A_{20}^{u+d}(t)$ at $m_{\pi} \approx 0.35 \text{ GeV}$ together with the result of a global simultaneous chiral fit using Eqs. (27)–(29).

E. CBChPT extrapolation of $B_{20}^{u+d}(t)$

The dependence on the pion mass and the momentum transfer squared of the isosinglet B_{20} GFF in $\mathcal{O}(p^2)$ CBChPT is given by [65]

$$B_{20}^{u+d}(t, m_{\pi}) = \frac{m_N(m_{\pi})}{m_N} B_{20}^{0,u+d} + A_{20}^{0,u+d} h_B^{u+d}(t, m_{\pi}) + \Delta B_{20}^{u+d}(t, m_{\pi}) + \frac{m_N(m_{\pi})}{m_N} \times \{ \delta_B^{t,u+d} t + \delta_B^{m_{\pi},u+d} m_{\pi}^2 \} + \mathcal{O}(p^3), \quad (28)$$

where $B_{20}^{0,u+d} \equiv B_{20}^{u+d}(t = 0, m_{\pi} = 0)$, and the terms ΔB_{20} , $\delta_B^{t,u+d} t$ and $\delta_B^{m_{\pi},u+d} m_{\pi}^2$ are of $\mathcal{O}(p^3)$ and represent only a part of the full $\mathcal{O}(p^3)$ -contribution. The *a priori* unknown constants $B_{20}^{0,u+d}$, $\delta_B^{t,u+d}$ and $\delta_B^{m_{\pi},u+d}$ may be obtained from a fit to the lattice data. A fit to our lattice results based on Eq. (28) turns out to be unstable and produces large values for the counter term parameter $\delta_B^{m_{\pi},u+d} \approx 15$. This can be seen as an indication that other higher-order correction terms of $\mathcal{O}(p^3)$ not yet included in Eq. (28) are numerically important and needed to stabilize the extrapolation. We note that the counting scheme of [65] suggests that ΔB_{20} is not a dominant $\mathcal{O}(p^3)$ -contribution

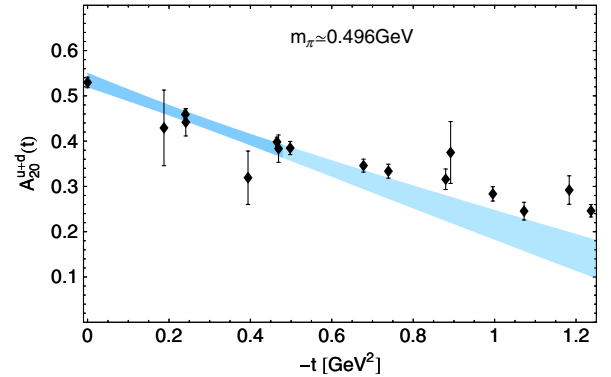


FIG. 30 (color online). Lattice results for $A_{20}^{u+d}(t)$ at $m_{\pi} \approx 0.496 \text{ GeV}$ together with the result of a global simultaneous chiral fit using Eqs. (27)–(29).

concerning the pion-mass dependence, at least for $t = 0$. This can be seen to some extent from the heavy-baryon-limit of Eq. (28), which does not reproduce the full coefficient, $\propto (A + B)_{20}^{0,u+d}$, of the $m_\pi^2 \log(m_\pi^2)$ -term in HBChPT (see e.g. [55,62,63]), but rather gives a term $\propto A_{20}^{0,u+d} m_\pi^2 \log(m_\pi^2)$ without the $B_{20}^{0,u+d} m_\pi^2 \log(m_\pi^2)$ contribution.

Since the instability of the fit can be traced back to the term $\Delta B_{20}^{u+d}(t, m_\pi)$, we performed the final fit dropping this contribution but keeping the counter terms $\propto t$ and $\propto m_\pi^2$. Based on this approach, we find that a global simultaneous fit to the GFFs A_{20}^{u+d} , B_{20}^{u+d} and C_{20}^{u+d} , using Eqs. (27) and (29) as described in the previous section, leads to a stable chiral extrapolation of all three GFFs. In particular the counter term parameters $\delta_B^{t,u+d}$ and $\delta_B^{m_\pi,u+d}$ turn out to be very small and fully compatible with zero within errors. We obtain $B_{20}^{0,u+d} = -0.140(84)$ and $B_{20}^{u+d}(t = 0, m_{\pi,\text{phys}}) = -0.095(86)$ at the physical pion mass. Results of the fit are shown in Figs. 31 and 32. We cannot rule out that the inclusion of the full $\mathcal{O}(p^3)$ -contributions to B_{20}^{u+d} will lead to a qualitatively different dependence on t and m_π in the region where lattice results are available, so that the results above should to be taken with due caution.

In Sec. V H, we will study the combined (t, m_π) -dependence of B_{20}^{u+d} in HBChPT at $\mathcal{O}(p^2)$ [64]. One-loop graphs with insertions of pion operators are fully included, leading to a nonanalytic dependence on the pion mass and the momentum transfer that is quite different from that shown in Figs. 31 and 32.

F. CBChPT extrapolation of $C_{20}^{u+d}(t)$

The (t, m_π) -dependence of the isosinglet GFF C_{20} in CBChPT to $\mathcal{O}(p^2)$ is given by [65]

$$C_{20}^{u+d}(t, m_\pi) = \frac{m_N(m_\pi)}{m_N} C_{20}^{0,u+d} + A_{20}^{0,u+d} h_C^{u+d}(t, m_\pi) + \Delta C_{20}^{u+d}(t, m_\pi) + \mathcal{O}(p^3), \quad (29)$$

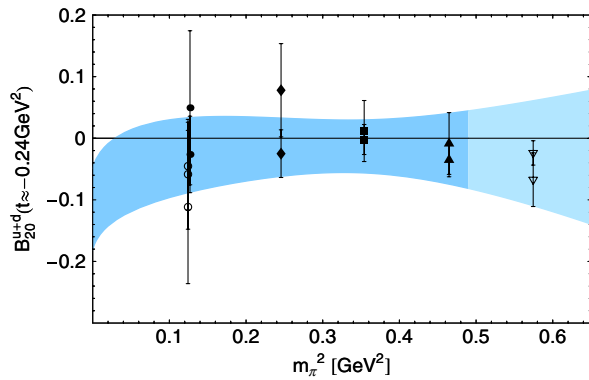


FIG. 31 (color online). Lattice results for B_{20}^{u+d} at $t \approx -0.24 \text{ GeV}^2$ versus m_π^2 together with the result of a global simultaneous chiral fit based on Eqs. (27) and (29) and a variant of Eq. (28), as described in the text.

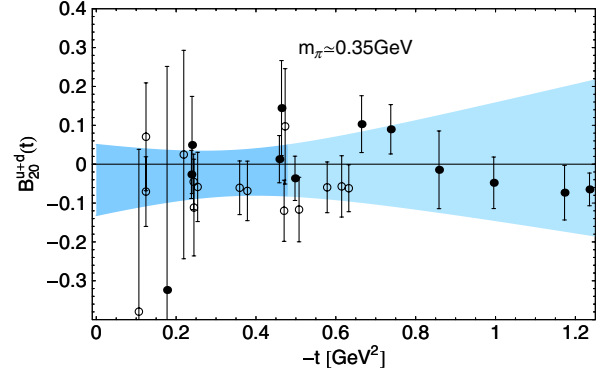


FIG. 32 (color online). Lattice results for $B_{20}^{u+d}(t)$ at $m_\pi \approx 350 \text{ MeV}$ versus $(-t)$ together with the result of a global simultaneous chiral fit based on Eqs. (27) and (29) and a variant of Eq. (28), as described in the text.

where $C_{20}^{0,u+d} \equiv C_{20}^{u+d}(t = 0, m_\pi = 0)$, and the term $\Delta C_{20}^{u+d} \propto \langle x \rangle_{u+d}^{\pi,0}$ is a part of the full $\mathcal{O}(p^3)$ -corrections [65]. In this counting scheme, counter terms of the form $\delta_C^{t,u+d} t$ and $\delta_C^{m_\pi,u+d} m_\pi^2$ first appear at $\mathcal{O}(p^4)$. In order to get a first idea about the possible t - and m_π -dependence of C_{20}^{u+d} in CBChPT, we have included the formally higher-order counter terms $\delta_C^{t,u+d} t$ and $\delta_C^{m_\pi,u+d} m_\pi^2$ in the fit to our lattice data, resulting in a stable chiral extrapolation. With $\langle x \rangle_{u+d}^{\pi,0} = 0.5$ from Table III as an input parameter, and taking into account the CBChPT results for A_{20}^{u+d} and B_{20}^{u+d} discussed in Secs. V D and V E, respectively, we obtain from a global simultaneous fit $C_{20}^{0,u+d} = -0.317(59)$ for the forward value in the chiral limit, and $C_{20}^{u+d}(t = 0, m_{\pi,\text{phys}}) = -0.267(62)$ at the physical pion mass. The parameters $\delta_C^{t,u+d}$ and $\delta_C^{m_\pi,u+d}$ turn out to be small. Changing $\langle x \rangle_{u+d}^{\pi,0}$ by $\pm 10\%$ results in a variation of $C_{20}^{0,u+d}(t = 0)$ by $\pm 5\%$, which is significantly smaller than the statistical error of 19%. The corresponding extrapolations are shown in Figs. 33 and 34. These results indicate a nontrivial dependence of the $n = 2$ moment of the isosing-

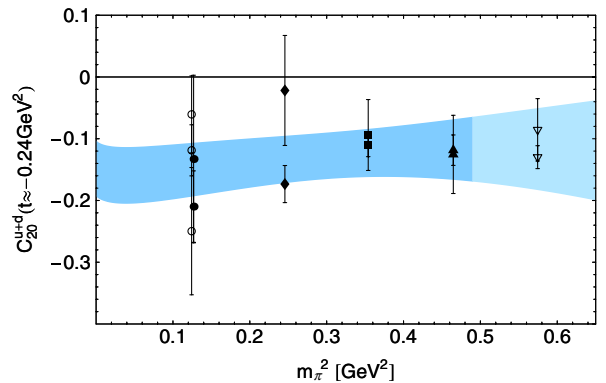


FIG. 33 (color online). Lattice results for C_{20}^{u+d} at $t \approx -0.24 \text{ GeV}^2$ versus m_π^2 together with the result of a global simultaneous chiral fit using Eqs. (27)–(29).

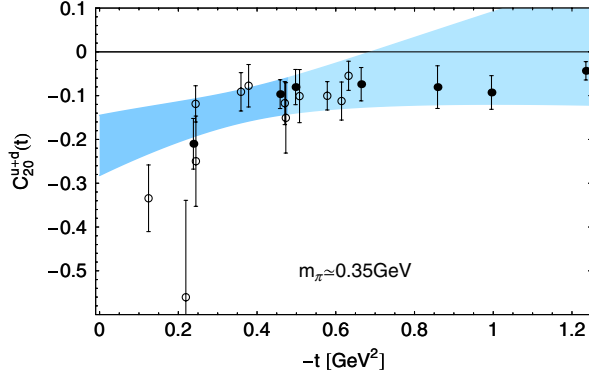


FIG. 34 (color online). Lattice results for $C_{20}^{u+d}(t)$ at $m_{\pi} \approx 350$ MeV versus $(-t)$ together with the result of a global simultaneous chiral fit using Eqs. (27)–(29).

let GPDs H and E on the longitudinal momentum transfer ξ .

A 3-dimensional plot showing the combined (t, m_{π}) -dependence of C_{20}^{u+d} is presented in Fig. 35, where the error bars of the lattice data points are illustrated by the stretched cuboids. The lattice data are superimposed with the result from the chiral fit discussed above, which is shown as a surface. The statistical error bars of the fit are shown for clarity only as bands for $t = 0$ and $m_{\pi} = 0$, respectively. In Sec. V J below, we will compare the results based on CBChPT with a fit to C_{20}^{u+d} in the framework of HBChPT.

G. Quark angular momentum J in CBChPT

The forward limit values of the isovector and isosinglet GFFs $A_{20}(t=0)$ and $B_{20}(t=0)$ we have studied in Secs. VA, VB, VD, and VE allow us to compute the angular momentum contributions of up- and down-quarks

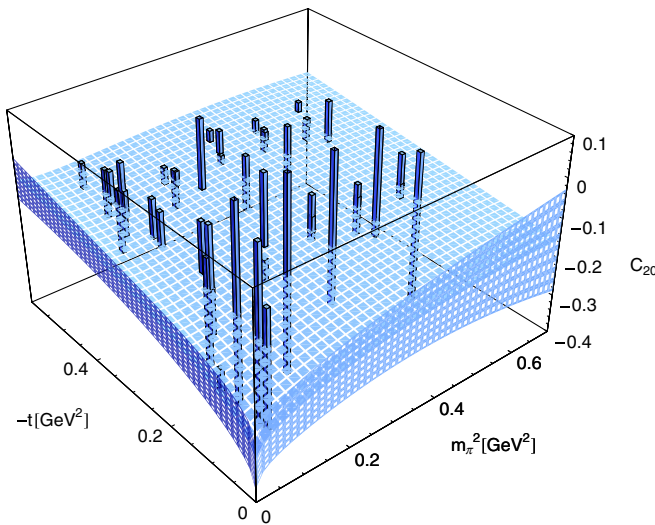


FIG. 35 (color online). Combined (t, m_{π}) -dependence of C_{20}^{u+d} from a global simultaneous chiral fit using Eqs. (27)–(29) compared to lattice data.

to the spin of the nucleon, $J^q = 1/2(A_{20}^q(0) + B_{20}^q(0)) = 1/2(\langle x \rangle^q + B_{20}^q(0))$. From the separate chiral extrapolations of the isosinglet A_{20} and B_{20} in CBChPT, we find for the total $u + d$ quark angular momentum at the physical pion mass $J^{u+d}(m_{\pi, \text{phys}}) = 0.213(44)$, corresponding to 43% of the total nucleon spin $S = 1/2$. Together with the chiral extrapolations for the isovector $u - d$ combination, we obtain the surprising result that the total quark angular momentum is carried by the up-quarks, $J^u(m_{\pi, \text{phys}}) = 0.214(27)$ and that the contribution from down-quarks is zero $J^d(m_{\pi, \text{phys}}) = -0.001(27)$. From Fig. 16, we note that the cancellation of $\Sigma^d/2$ and L^d appears to be systematic for all m_{π} , and it will be interesting to understand whether this is accidental or has a physical origin. Taking into account preliminary results for the quark spin $\tilde{A}_{10}^q/2(t=0) = \Delta \Sigma^q/2$, as obtained from a ChPT extrapolation including the Δ resonance [49,50] of $g_A = \Delta \Sigma^{u-d}$ and a self-consistently improved one-loop ChPT extrapolation of $\Delta \Sigma^{u+d}$ [48], we find that the quark orbital angular momentum $L^q = J^q - \Delta \Sigma^q/2$ contributions to the nucleon spin are $L^u = -0.195(44)$ and $L^d = 0.200(44)$ at the physical pion mass. The nearly complete cancellation of up- and down-quark OAM contributions that we observe for pion masses above 350 MeV therefore also holds at $m_{\pi, \text{phys}}$, where we find $L^{u+d} = 0.005(52)$. We emphasize again that no phenomenological values for $\Delta \Sigma = \langle 1 \rangle_{\Delta q}$, $\langle x \rangle_q$ and $\langle x \rangle_{\Delta q}$ have been included in the extrapolations, and that we have omitted disconnected diagrams in the lattice calculations. We will compare these CBChPT results with corresponding HBChPT results below in Sec. V J.

H. HBChPT extrapolation of E_{20}^{u+d} and M_{20}^{u+d}

In heavy baryon chiral perturbation theory [62,64] to $\mathcal{O}(p^2)$, the combined (t, m_{π}) -dependence of the GFF-combination $E_{20}^{u+d}(t) = A_{20}^{u+d}(t) + t/(4m_N^2)B_{20}^{u+d}(t)$ is quite different from that of $M_{20}^{u+d}(t) = A_{20}^{u+d}(t) + B_{20}^{u+d}(t)$, which in the forward limit is equal to 2 times the total quark angular momentum $2J_q = M_{20}^{u+d}(t=0)$. While at this order M_{20}^{u+d} shows a nonanalytic dependence on t and m_{π} as discussed below, E_{20}^{u+d} is constant up to analytic tree-level contributions,

$$E_{20}^{u+d}(t, m_{\pi}) = E_{20}^{0, u+d} + E_{20}^{m_{\pi}, u+d} m_{\pi}^2 + E_{20}^{t, u+d} t. \quad (30)$$

A fit to our lattice results based on Eq. (30) is shown in Figs. 36–39. The linear dependence on t and m_{π}^2 works well even beyond the fitted range, i.e. for $-t \geq 0.48$ GeV². This is not surprising since E_{20}^{u+d} is clearly dominated by the GFF A_{20}^{u+d} , which does not show a strong curvature in t as seen in Figs. 8 and 10. However, it is obvious that the HBChPT result in Eq. (30) lacks structures which would allow for an upwards bending of $E_{20}^{u+d}(t=0) = A_{20}^{u+d}(t=0)$ at small pion masses towards the phenomenological value, in contrast to the covariant approach studied in Sec. VA.

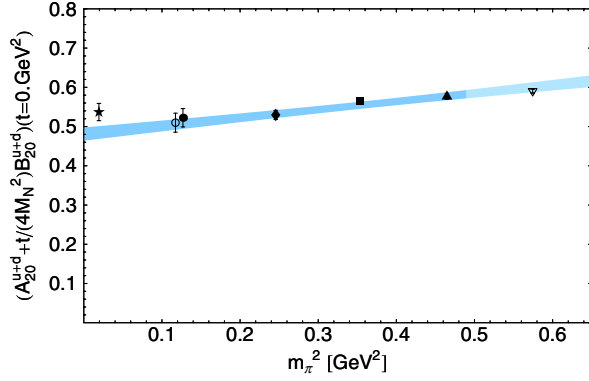


FIG. 36 (color online). Lattice results for E_{20}^{u+d} at $t = 0$ versus m_{π}^2 together with the result of a global chiral fit using Eq. (30).

The fit gives $E_{20}^{0,u+d} = 0.481(15)$ in the chiral limit, which we will use for the chiral extrapolations based on HBChPT of the total angular momentum and the anomalous gravitomagnetic moment $B_{20}^{u+d}(t = 0)$ below. At the physical pion mass, we find $E_{20}^{u+d}(t = 0, m_{\pi, \text{phys}}) = \langle x \rangle_{u+d} = 0.485(14)$, which is approximately 10% below the phenomenological results, $\langle x \rangle_{u+d}^{\text{CTEQ6}} = 0.537(22)$ and $\langle x \rangle_{u+d}^{\text{MRST2001}} = 0.538(22)$ [81].

The pion-mass dependence of $M_{20}^{u+d}(t)$ for nonzero t is given by [62,64]

$$M_{20}^{u+d}(t, m_{\pi}) = M_{20}^{0,u+d} \left\{ 1 - \frac{3g_A^2 m_{\pi}^2}{(4\pi f_{\pi})^2} \ln\left(\frac{m_{\pi}^2}{\Lambda_{\chi}^2}\right) \right\} + M_2^{(2,\pi)}(t, m_{\pi}) + M_{20}^{m_{\pi},u+d} m_{\pi}^2 + M_{20}^{t,u+d} t, \quad (31)$$

with new counter terms $M_{20}^{m_{\pi},u+d}$ and $M_{20}^{t,u+d}$. The non-analytic dependence on t and m_{π} in $M_2^{(2,\pi)}(t, m_{\pi})$ results from pion-operator insertions and is directly proportional to the (isosinglet) momentum fraction of quarks in the pion in the chiral limit, $\langle x \rangle_{u+d}^{\pi,0}$. We use $\langle x \rangle_{u+d}^{\pi,0} = 0.5$ from Table III for the fit. No additional parameters are needed to this order. The results of chiral fits based on Eq. (31) are

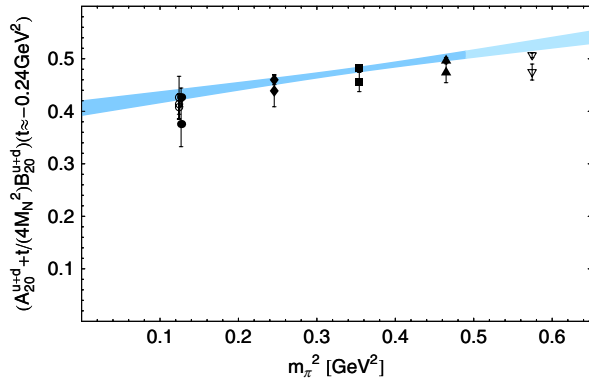


FIG. 37 (color online). Lattice results for E_{20}^{u+d} at $-t \approx 0.24 \text{ GeV}^2$ versus m_{π}^2 together with the result of a global chiral fit using Eq. (30).

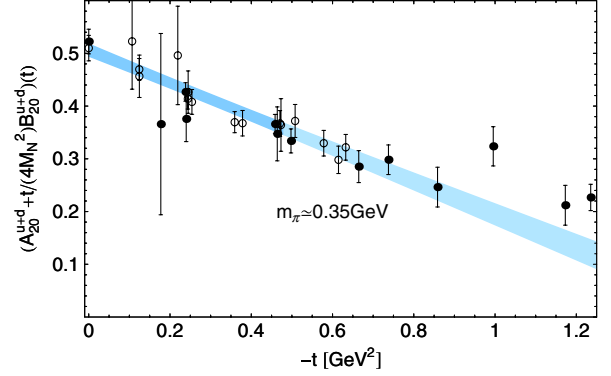


FIG. 38 (color online). Lattice results for E_{20}^{u+d} at $m_{\pi} \approx 350 \text{ MeV}$ versus $-t$ together with the result of a global chiral fit using Eq. (30).

presented in Figs. 40 and 41. We find $M_{20}^{0,u+d} = 0.522(41)$ and $M_{20}^{u+d}(t = 0, m_{\pi, \text{phys}}) = 0.526(48)$.

I. HBChPT extrapolation of B_{20}^{u+d}

Total momentum and angular momentum conservation implies that the total anomalous gravitomagnetic moment of quarks and gluons in the nucleon has to vanish, $\sum_{q,g} B_{20}(t = 0) = 0$. An interesting question is whether the individual quark and gluon contributions to B_{20} are separately zero or very small, as previously speculated [83,84]. The first lattice calculations [12,13] showed that B_{20}^{u+d} is compatible with zero for $(-t) \geq 0.5 \text{ GeV}^2$ at pion masses of $m_{\pi} \geq 600 \text{ MeV}$. Based on our new results and the ChPT fits performed above, we are now in a position to study B_{20}^{u+d} more carefully as a function of t and m_{π} . The GFF B_{20}^{u+d} can be written as a linear combination of Eq. (30) and (31). A separate fit to the data with fixed $E_{20}^{0,u+d} = 0.481(15)$ gives $B_{20}^{u+d}(t = 0, m_{\pi, \text{phys}}) = 0.050(49)$, which is compatible with the fits to M_{20}^{u+d} and E_{20}^{u+d} above that in combination give $(M - E)_{20}^{u+d}(t = 0, m_{\pi, \text{phys}}) = 0.041(50)$. Although the absolute value of $B_{20}^{u+d}(t = 0)$ is

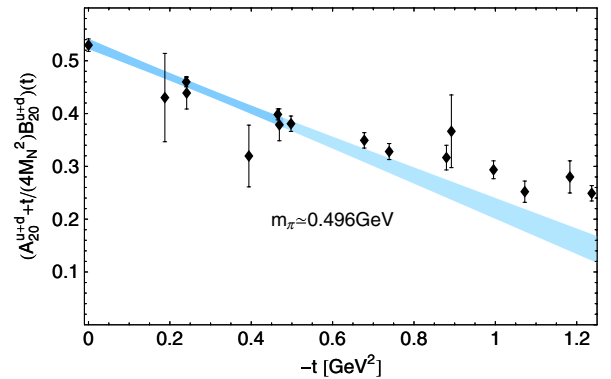


FIG. 39 (color online). Lattice results for E_{20}^{u+d} at $m_{\pi} \approx 496 \text{ MeV}$ versus $-t$ together with the result of a global chiral fit using Eq. (30).

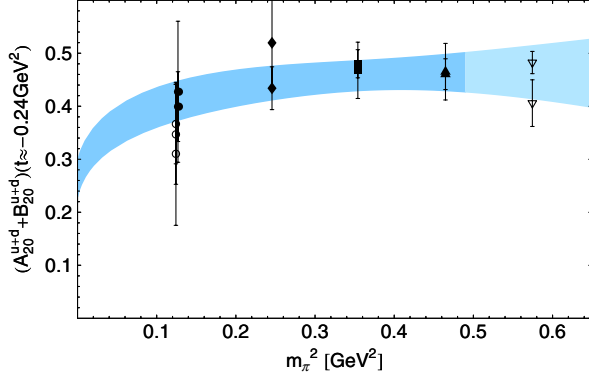


FIG. 40 (color online). Lattice results for M_{20}^{u+d} at $|t| \approx 0.24 \text{ GeV}^2$ versus m_π^2 together with the result of a global chiral fit using Eq. (31).

again rather small, we note that the sign is different from that found in Sec. VE based on the CBChPT fit. A 10% variation of the input parameter $\langle x \rangle_{u+d}^{\pi,0}$ leads to change of 0.023 in $B_{20}^{u+d}(t, m_{\pi,\text{phys}})$ at $t = 0$, which is well below the statistical error of 0.049, and a change of 0.008 at a momentum transfer of $|t| \approx 0.24 \text{ GeV}^2$, which is well below the statistical error of 0.031.

The dependence of B_{20}^{u+d} on t and on the pion mass is shown in Figs. 42 and 43. The dependence on the momentum transfer squared turns out to be somewhat different from the CBChPT result in Fig. 32 where contributions from pion-operator insertions $\propto \langle x \rangle_{u+d}^{\pi,0}$ have not been included, but the two results are statistically consistent. The combined dependence of B_{20}^{u+d} on t and m_π from the HBChPT fit compared to lattice data points is presented in a 3-dimensional plot in Fig. 44. It is interesting to note that the fit based on Eq. (31) leads to a clearly visible nonanalytic dependence of B_{20}^{u+d} on the pion mass and the momentum transfer. In particular, we find a nonzero, negative B_{20}^{u+d} for $|t| > 0.05 \text{ GeV}^2$, $m_\pi^2 \lesssim 0.1 \text{ GeV}^2$ from the chiral extrapolation, which may be confirmed in future lattice calculations or experimental measurements.

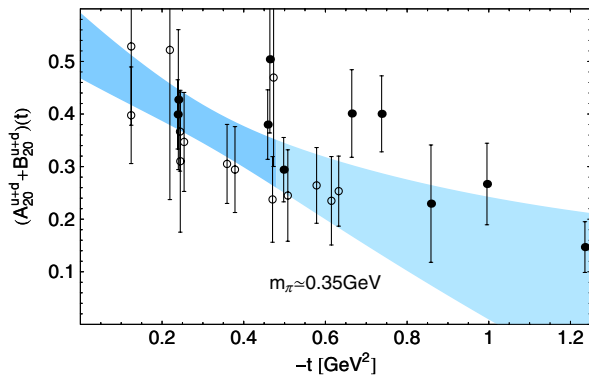


FIG. 41 (color online). Lattice results for M_{20}^{u+d} at $m_\pi \approx 350 \text{ MeV}$ versus $(-t)$ together with the result of a global chiral fit using Eq. (31).

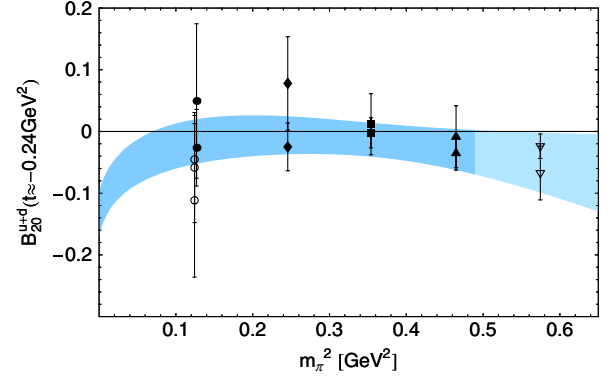


FIG. 42 (color online). Lattice results for B_{20}^{u+d} at $|t| \approx 0.24 \text{ GeV}^2$ versus m_π^2 together with the result of a global chiral fit using a linear combination of Eqs. (30) and (31).

J. HBChPT extrapolation of C_{20}^{u+d}

At order $\mathcal{O}(p^2)$, the pion-mass dependence of the GFF $C_{20}^{u+d}(t)$ is given by [62–64]

$$C_{20}^{u+d}(t, m_\pi) = \frac{1}{1 - t/(4m_N^2)} \{ C_{20}^{0,u+d} + E_2^{(1,\pi)}(t, m_\pi) + E_2^{(2,\pi)}(t, m_\pi) + C^{m_\pi, u+d} m_\pi^2 + C^{t, u+d} t \}, \quad (32)$$

where $C_{20}^{0,u+d} \equiv C_{20}^{u+d}(t=0, m_\pi=0)$. The terms $E_2^{(1,\pi)}(t, m_\pi)$ and $E_2^{(2,\pi)}(t, m_\pi)$ contain nonanalytic terms in t and m_π that come from insertions of pion operators proportional to $\langle x \rangle_{u+d}^{\pi,0}$. Additionally, $E_2^{(2,\pi)}(t, m_\pi)$ depends on the low energy constants c_1 , c_2 and c_3 . We fix these parameters to the values given in Table III. The result of a fit to our lattice data as a function of the pion mass squared for fixed $t \approx -0.24 \text{ GeV}^2$ is shown in Fig. 45. The t -dependence at a pion mass of $\approx 350 \text{ MeV}$ is presented in Fig. 46. We find $C_{20}^{0,u+d} = -0.507(55)$, and $C_{20}^{u+d}(t=0, m_{\pi,\text{phys}}) = -0.421(54)$ at the physical pion mass. We note that these values are approximately 60% larger in

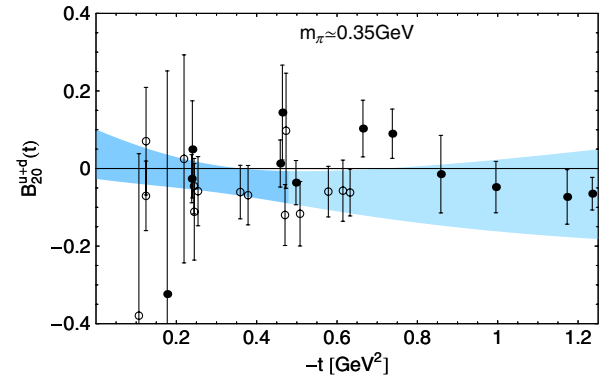


FIG. 43 (color online). Lattice results for B_{20}^{u+d} at $m_\pi \approx 350 \text{ MeV}$ versus $(-t)$ together with the result of a global chiral fit using a linear combination of Eqs. (30) and (31).

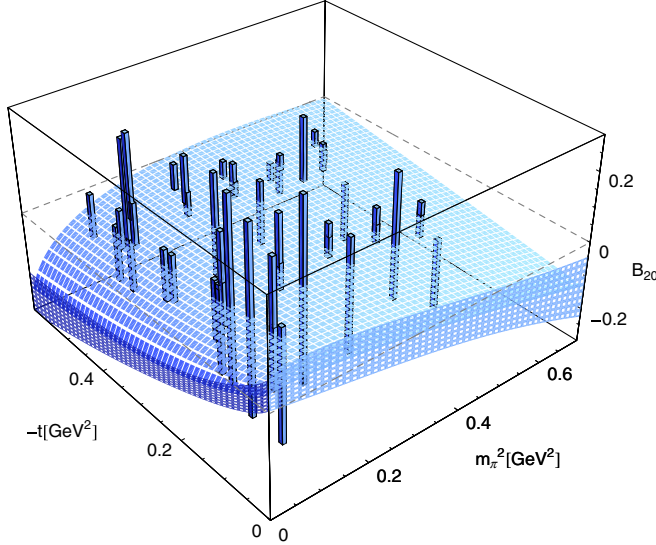


FIG. 44 (color online). Combined (t, m_π) -dependence of the quark anomalous gravitomagnetic moment B_{20}^{u+d} from a global chiral fit using a linear combination of Eqs. (30) and (31) compared to lattice data.

magnitude than the corresponding CBChPT results in Sec. V F based on covariant ChPT, which is directly related to the stronger downwards bending of C_{20}^{u+d} for $(-t) \rightarrow 0$ in Fig. 45 compared to the slight upwards bending in Fig. 33. As in the case of the CBChPT extrapolation, a variation of the input value $\langle x \rangle_{u+d}^{\pi,0}$ by 10% results in a $\approx 5\%$ change of $C_{20}^{0,u+d}(t=0)$, which is below the 11% statistical error.

Figure 47 shows our combined lattice results for C_{20}^{u+d} versus $(-t)$ and m_π in a single 3-dimensional plot, together with the result from the HBChPT fit discussed above, which is shown as a surface. The statistical error bars are shown for clarity as bands for $t = 0 \text{ GeV}^2$ and $m_\pi = 0 \text{ MeV}$, respectively. It is interesting to note that the overall shape of the extrapolation surface is similar to the CBChPT result in Sec. V F. The only behavior that differs by more

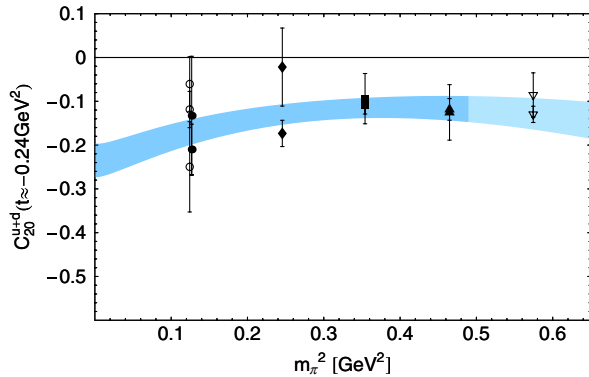


FIG. 45 (color online). Lattice results for C_{20}^{u+d} at $|t| \approx 0.24 \text{ GeV}^2$ versus m_π^2 together with the result of a global chiral fit using Eq. (32).

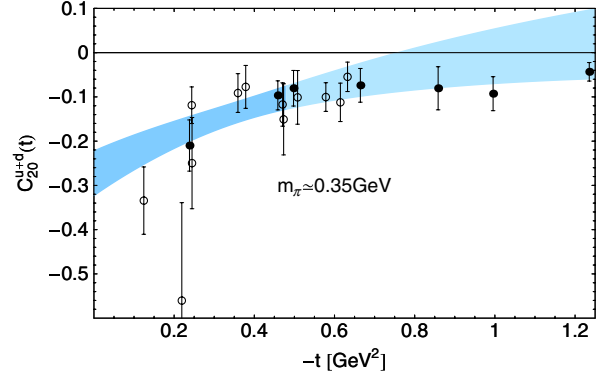


FIG. 46 (color online). Lattice results for C_{20}^{u+d} at $m_\pi \approx 350 \text{ MeV}$ versus $-t$ together with the result of a global chiral fit using Eq. (32).

than the statistical errors is the slightly stronger bending towards negative values of C_{20}^{u+d} at the origin in Fig. 47.

K. HBChPT extrapolation of quark angular momentum J

From our results for M_{20} above, we find a total quark angular momentum $J^{u+d} = 0.263(24)$ at the physical pion mass, which is larger than but statistically compatible with the CBChPT value in Sec. V G.

As an alternative, we can also calculate J^{u+d} by first extrapolating $B_{20}(t, m_\pi)$ to $t = 0$ and combining it with $A_{20}(t = 0, m_\pi)$ to obtain $J(m_\pi)$, and then extrapolating the values of $J(m_\pi)$ to the physical pion mass using HBChPT that explicitly includes the Δ resonance [55]. Evaluating Eq. (31) at $t = 0$ yields

$$J^{u+d}(m_\pi) = \frac{1}{2} \left\{ (A + B)_{20}^{0,u+d} + 3(\langle x \rangle_{u+d}^{\pi,0} - (A + B)_{20}^{0,u+d}) \times \frac{g_A^2 m_\pi^2}{(4\pi f_\pi)^2} \ln\left(\frac{m_\pi^2}{\Lambda_\chi^2}\right) \right\} + J^{m_\pi, u+d} m_\pi^2, \quad (33)$$

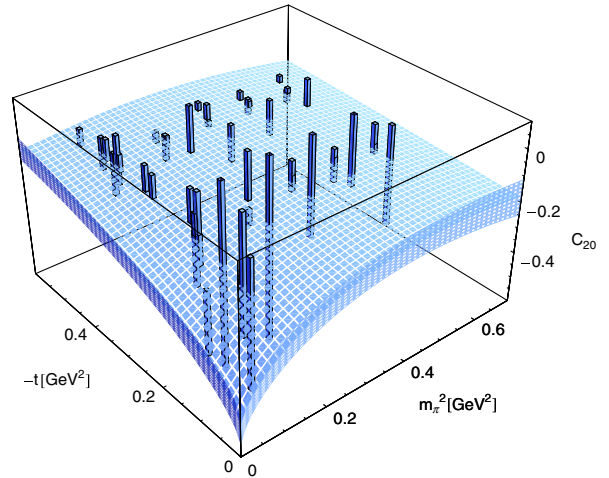


FIG. 47 (color online). Combined (t, m_π) -dependence of C_{20}^{u+d} from a global chiral fit using Eq. (32) compared to lattice data.

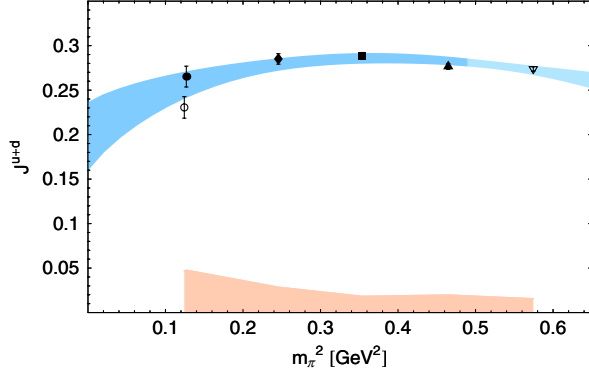


FIG. 48 (color online). Chiral extrapolation of J^{u+d} using HBChPT including the Δ resonance, Eq. (34). The fit and error band on the axis are explained in the text.

which agrees with [55]. Note that in the notation of [55] we have $b_{qN} = (A + B)_{20}^{0,u+d} = M^{0,u+d}$. Including explicitly the Δ resonance in the calculation, the ChPT result then reads [55]

$$\begin{aligned}
 J^{u+d}(m_\pi; \Delta) = & J^{u+d}(m_\pi) - \frac{1}{2} \left(\frac{9}{2} (A + B)_{20}^{0,u+d} + 3 \langle x \rangle_{u+d}^{\pi,0} \right. \\
 & \left. - \frac{15}{2} b_{q\Delta} \right) \times \frac{8g_{\pi N\Delta}^2}{9(4\pi f_\pi)^2} \left\{ (m_\pi^2 - 2\Delta^2) \right. \\
 & \times \ln \left(\frac{m_\pi^2}{\Lambda_\chi^2} \right) + 2\Delta \sqrt{\Delta^2 - m_\pi^2} \\
 & \left. \times \ln \left(\frac{\Delta - \sqrt{\Delta^2 - m_\pi^2}}{\Delta + \sqrt{\Delta^2 - m_\pi^2}} \right) \right\}, \quad (34)
 \end{aligned}$$

where $\Delta = m_\Delta - m_N$ denotes the Δ -nucleon mass difference. In order to reduce the number of free parameters in the fit, we use $\Delta = 0.3$ GeV and the large- N_c relation $g_{\pi N\Delta} = 3/(2^{3/2})g_A$ from Table III. We first extrapolate $B_{20}^{u+d}(t, m_\pi)$ linearly in t to $t = 0$. A fit based on Eq. (34) to the lattice results for $(A + B)_{20}^{u+d}(t = 0, m_\pi)$ with $m_\pi \leq 700$ MeV then gives $(A + B)_{20}^{0,u+d} = b_{qN} = 0.545(12)$,

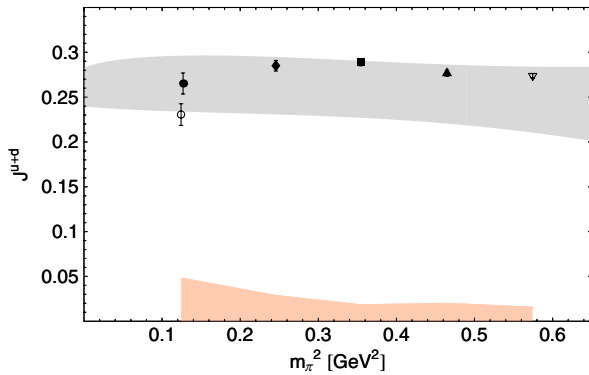


FIG. 49 (color online). Comparison of a global fit to $A_{20}^{u+d} + B_{20}^{u+d}$ using Eq. (31) and the lattice results for J^{u+d} . The fit and error band on the axis are explained in the text.

$b_{q\Delta} = 0.427(51)$ and $J^{u+d}(m_{\pi,\text{phys}}; \Delta) = 0.212(32)$ at the physical pion mass, which is very close to the CBChPT result in Sec. V G, $J^{u+d}(m_{\pi,\text{phys}}) = 0.213(44)$. The result for $J^{u+d}(m_\pi; \Delta)$ as a function of the pion mass is shown in Fig. 48, where the error due to the linear extrapolation of $B(t, m_\pi)$ to $t = 0$ is indicated by the error band at the m_π^2 -axis as explained at the end of Sec. IV and the error bars on the lattice data points for J only include the errors arising from $A_{20}(t = 0)$. In Fig. 49, we compare the result of the chiral extrapolation of $M_{20}^{u+d}(t)$ for nonzero t from the previous section with the lattice results for J^{u+d} corresponding to the extrapolated $B_{20}^{u+d}(t = 0)$. The two different ways of fitting and extrapolating J^{u+d} in m_π are compatible within errors, $J_{\text{from } t \neq 0}^{u+d} = 0.263(24)$ versus $J_{t \rightarrow 0}^{u+d}(m_{\pi,\text{phys}}; \Delta) = 0.212(32)$, where the chiral fit including the Δ leads to a stronger curvature at small m_π and therefore to a smaller central value for J^{u+d} at the physical point. Together with preliminary results for the quark spin $\bar{A}_{10}^{u+d}/2(t = 0) = \Delta \bar{\Sigma}^{u+d}/2$ as obtained from a self-consistently improved one-loop ChPT extrapolation [48], we find that the quark orbital angular momentum $L^{u+d} = J^{u+d} - \Delta \bar{\Sigma}^{u+d}/2$ contribution to the nucleon spin is zero within errors: $L^{u+d} = 0.005(43)$ for $J_{t \rightarrow 0}^{u+d}(m_{\pi,\text{phys}}; \Delta) = 0.212(32)$ and $L^{u+d} = 0.056(37)$ for $J_{\text{from } t \neq 0}^{u+d} = 0.263(24)$ at the physical pion mass.

VI. SUMMARY AND CONCLUSIONS

This work presents the first comprehensive full lattice QCD study of the lowest three moments of unpolarized and polarized GPDs in the chiral regime with pion masses as low as 350 MeV. We find good overall agreement with existing experimental results. We note, however, that we have omitted disconnected diagrams, which in principle contribute to isoscalar observables.

As in our previous study of the axial vector coupling constant [85], the consistency of these moments in lattice volumes of $(2.5 \text{ fm})^3$ and $(3.5 \text{ fm})^3$ at $m_\pi = 350$ MeV indicates that finite volume effects are negligible within statistical errors.

One significant result of this work is the clear indication that the transverse size of the nucleon, as characterized by the transverse 2-dimensional rms radius, is a strongly decreasing function of the momentum fraction x carried by the quarks. At the lightest quark mass, the isovector transverse rms radius drops by almost 60% between the zeroth moment, which roughly corresponds to an average momentum fraction [86] $\langle x \rangle \approx 0.2$ and the second moment, which roughly corresponds to an average momentum fraction $\langle x \rangle \approx 0.4$. This decrease in the chiral regime is even stronger than our original observation of the decrease of the transverse size with momentum fraction in the ‘‘heavy pion world’’ [14].

In a first direct comparison with phenomenological parametrizations of the GPDs $H(x, \xi = 0, t)$ and $\bar{H}(x, \xi = 0, t)$

constrained by structure function and form factor data [11], we find qualitative consistency for the ratios of GFFs in both the isovector and isosinglet cases.

Our results provide insight into the contributions of the spin and orbital angular momentum of u and d quarks to the spin of the proton. Although the individual orbital angular momentum contributions of the u and d quarks are sizeable, $L^d \approx -L^u \approx 30\%$, they cancel within errors so that the total contribution is $L^{u+d} \approx 0$. In addition, the spin and orbital contributions of the d quark also cancel within errors, so $J^d \approx 0$. The total quark angular momentum contribution is $J^{u+d} \approx 40 - 50\%$ at our lowest pion masses.

More quantitatively, we performed a variety of chiral fits to the unpolarized $n = 2$ moments using covariant BChPT [65] and HBChPT results [55,62–64]. A summary of our results for various observables at the physical pion mass and vanishing momentum transfer $t = 0$ is given in Table V, where the quoted errors are statistical only. We note that a consistent inclusion of all $\mathcal{O}(p^3)$ -terms in our fits, which may involve additional constants, would have the potential to increase the statistical errors on the physical quantities at the chiral limit. However, for the reasons described in Sec. VA, the prescription of adding a single m_π^3 -term with extremal values of “natural” coefficients does not lead to reasonable χ^2 fits, so we have not attempted to include quantitative estimates of these errors in the present work.

With the exception of a fit to J_q based on HBChPT including the Δ resonance, we have consistently extrapolated the GFFs simultaneously in the pion mass and the momentum transfer squared t . The simultaneous covariant BChPT fits to the GFFs A_{20} , B_{20} and C_{20} , which include approximately 120 lattice data points and typically 9 unknown low energy constants, produce reasonable parameterizations of the (t, m_π) -dependences of the generalized form factors in the ranges $m_\pi \leq 700$ MeV and $|t| \leq 0.5$ GeV². In particular, the covariant extrapolations for the isovector and isosinglet momentum fractions $\langle x \rangle$ yield values at the physical point remarkably close to phenomenology. This represents a significant advance in our understanding of the pion-mass dependence of these important observables. The first exploration of the combined non-analytic dependence of the isosinglet GFFs B_{20}^{u+d} and C_{20}^{u+d} on t and m_π was made using covariant BChPT and HBChPT, and visualizations of the resulting

(t, m_π) -dependences of these GFFs in 3-dimensional plots reveal interesting nonlinear correlations in the pion mass and the momentum transfer squared.

In spite of the overall success of the chiral extrapolations, it is clear that the ChPT analysis has not yet been carried to sufficiently high order to be applicable to the full range of pion masses included in this work. The facts that HBChPT fits to A_{20}^{u-d} and A_{20}^{u+d} cannot describe the behavior of the lattice data over as large a range or as accurately as covariant BChPT, and that the fitted counter terms are so different indicates that the higher-order terms in $1/m_N$ included in CBChPT are important for these observables. Similarly, the fact that it was important to include some particular terms of order $\mathcal{O}(p^3)$ and $\mathcal{O}(p^4)$ in some CBChPT fits indicates the need to fully determine these orders in ChPT so that they can be consistently included in fits to lattice data. Finally, the significant effect of including the Δ in J^{u+d} , its known importance in the axial charge, and large N_c arguments [87] indicates the desirability of consistent inclusion of the Δ . Thus, future progress requires both the extension of lattice calculations to lower pion mass and the inclusion of higher-order terms and Δ degrees of freedom in ChPT.

ACKNOWLEDGMENTS

The authors wish to thank M. Diehl, M. Dorati, T. Gail, T. Hemmert, J.-W. Chen and A. Manohar for stimulating discussions. This work was supported in part by U.S. DOE Contract No. DE-AC05-06OR23177 under which JSA operates Jefferson Laboratory, by the DOE Office of Nuclear Physics under Grant Nos. DE-FG02-94ER40818, DE-FG02-04ER41302, DE-FG02-96ER40965, the Jeffress Memorial Trust Grant No. J-813, the DFG (Forschergruppe Gitter-Hadronen-Phänomenologie) and in part by the EU Integrated Infrastructure Initiative Hadron Physics (I3HP) under Contract No. RII3-CT-2004-506078. Ph.H. and B.M. acknowledge support by the Emmy-Noether program of the DFG. Ph.H. and W.S. would like to thank the A. v. Humboldt Foundation for support by the Feodor-Lynen program. It is a pleasure to acknowledge the use of computer resources provided by the DOE through the USQCD project at Jefferson Lab and ORNL and through its support of the MIT Blue Gene/L. We are indebted to members of the MILC and SESAM Collaborations for providing the dynamical quark configurations which made our full QCD calculations possible.

TABLE V. Summary of proton observables at $t = 0$ and $m_{\pi,\text{phys}}$ from chiral extrapolations, in the $\overline{\text{MS}}$ scheme at a scale of $\mu^2 = 4$ GeV².

	A_{20}^{u-d}	B_{20}^{u-d}	C_{20}^{u-d}	A_{20}^{u+d}	B_{20}^{u+d}	C_{20}^{u+d}	J^{u+d}	J^u	J^d
Covariant BChPT	0.157(10)	0.273(63)	-0.017(41)	0.520(24)	-0.095(86)	-0.267(62)	0.213(44)	0.214(27)	-0.001(27)
HBChPT				0.485(14)	0.050(49)	-0.421(54)	0.263(24)		
HBChPT with Δ							0.212(32)		
Phenomenology	0.155(5)			0.537(22)					

APPENDIX: TABLES

Lattice parameters of the datasets 1, ..., 6 are provided in Table I. The GFFs are given in the $\overline{\text{MS}}$ scheme at a scale of $\mu^2 = 4 \text{ GeV}^2$.

TABLE VI. Results for the isovector unpolarized generalized form factors for dataset 1.

$-t[\text{GeV}^2]$	A_{10}^{u-d}	B_{10}^{u-d}	A_{20}^{u-d}	B_{20}^{u-d}	C_{20}^{u-d}	A_{30}^{u-d}	B_{30}^{u-d}
0.000	1.000(1)	...	0.223(3)	0.072(4)	...
0.203	0.731(73)	2.331(347)	0.179(17)	0.331(91)	-0.094(113)	0.072(10)	0.051(59)
0.243	0.796(6)	2.645(55)	0.201(3)	0.398(16)	-0.002(11)	0.071(2)	0.109(9)
0.243	0.735(29)	2.570(120)	0.187(7)	0.340(29)	-0.006(28)	0.066(3)	0.078(13)
0.420	0.606(64)	1.748(239)	0.160(16)	0.258(53)	-0.065(32)	0.055(7)	0.078(29)
0.475	0.659(9)	2.093(48)	0.180(3)	0.341(15)	-0.008(6)	0.066(3)	0.092(8)
0.477	0.605(29)	2.000(110)	0.170(7)	0.311(29)	-0.027(14)	0.062(3)	0.069(13)
0.498	0.646(15)	1.994(60)	0.179(4)	0.325(16)	0.014(7)	0.066(3)	0.088(9)
0.697	0.561(12)	1.665(51)	0.163(4)	0.294(15)	-0.001(6)	0.061(3)	0.084(8)
0.741	0.542(16)	1.611(57)	0.160(5)	0.288(16)	0.006(6)	0.059(3)	0.075(8)
0.911	0.487(17)	1.434(65)	0.149(6)	0.292(23)	0.005(8)	0.055(4)	0.102(12)
0.918	0.462(31)	1.317(125)	0.136(9)	0.226(33)	0.012(15)	0.053(4)	0.057(15)
0.996	0.493(16)	1.289(47)	0.154(5)	0.254(16)	0.006(8)	...	0.070(5)
1.117	0.425(17)	1.152(58)	0.137(6)	0.233(18)	-0.001(5)	0.053(4)	0.074(9)
1.199	0.412(21)	1.100(70)	0.129(6)	0.225(21)	0.014(7)	0.047(4)	0.073(10)
1.239	0.426(15)	1.077(42)	0.137(5)	0.214(13)	0.004(5)	0.054(4)	0.069(7)

TABLE VII. Results for the isovector unpolarized generalized form factors for dataset 2.

$-t[\text{GeV}^2]$	A_{10}^{u-d}	B_{10}^{u-d}	A_{20}^{u-d}	B_{20}^{u-d}	C_{20}^{u-d}	A_{30}^{u-d}	B_{30}^{u-d}
0.000	1.000(2)	...	0.223(4)	0.078(6)	...
0.200	0.924(100)	3.454(490)	0.196(26)	0.461(125)	0.261(149)	0.054(15)	0.168(76)
0.242	0.798(8)	2.540(67)	0.201(4)	0.350(20)	-0.006(14)	0.070(3)	0.072(11)
0.243	0.804(38)	2.384(146)	0.196(9)	0.289(36)	-0.044(37)	0.072(5)	0.057(17)
0.414	0.782(85)	2.226(301)	0.189(22)	0.346(69)	0.005(43)	0.061(10)	0.137(34)
0.473	0.678(11)	2.034(57)	0.181(4)	0.314(18)	-0.001(7)	0.063(4)	0.073(10)
0.475	0.656(37)	1.697(133)	0.171(9)	0.221(35)	0.000(19)	0.066(5)	0.053(18)
0.498	0.651(17)	1.873(65)	0.177(5)	0.274(18)	-0.008(10)	0.064(4)	0.050(10)
0.693	0.587(16)	1.682(63)	0.166(6)	0.297(20)	0.001(8)	0.062(5)	0.077(11)
0.741	0.549(18)	1.441(57)	0.153(5)	0.222(17)	-0.007(8)	0.059(4)	0.045(9)
0.904	0.506(23)	1.391(80)	0.150(8)	0.224(24)	-0.002(11)	0.058(6)	0.067(15)
0.911	0.556(56)	1.361(202)	0.160(15)	0.218(49)	0.007(22)	0.066(8)	0.039(23)
0.996	0.464(20)	1.189(51)	0.146(7)	0.212(18)	-0.005(10)	...	0.058(6)
1.106	0.450(23)	1.147(68)	0.137(8)	0.210(20)	0.005(7)	0.049(5)	0.052(11)
1.195	0.437(29)	1.085(88)	0.143(9)	0.226(27)	-0.010(11)	0.052(5)	0.044(12)
1.238	0.404(18)	0.987(41)	0.134(6)	0.189(14)	-0.001(6)	0.055(5)	0.045(9)

TABLE VIII. Results for the isovector unpolarized generalized form factors for dataset 3.

$-t[\text{GeV}^2]$	A_{10}^{u-d}	B_{10}^{u-d}	A_{20}^{u-d}	B_{20}^{u-d}	C_{20}^{u-d}	A_{30}^{u-d}	B_{30}^{u-d}
0.000	1.000(1)	...	0.226(4)	0.074(5)	...
0.193	0.674(83)	2.147(465)	0.176(24)	0.226(119)	-0.044(152)	0.046(13)	0.058(87)
0.241	0.770(8)	2.399(62)	0.200(4)	0.358(18)	-0.009(13)	0.074(3)	0.094(12)
0.242	0.724(35)	2.232(154)	0.187(8)	0.345(35)	0.052(35)	0.067(4)	0.075(17)
0.403	0.627(78)	1.723(305)	0.165(20)	0.243(68)	-0.010(45)	0.049(9)	0.118(38)
0.469	0.640(12)	1.890(54)	0.181(4)	0.300(17)	0.000(7)	0.069(4)	0.078(10)
0.472	0.584(34)	1.713(142)	0.171(9)	0.265(34)	0.003(20)	0.065(5)	0.075(17)
0.498	0.593(17)	1.819(61)	0.169(5)	0.305(19)	0.013(9)	0.064(4)	0.087(11)
0.685	0.546(17)	1.543(62)	0.165(6)	0.263(20)	-0.007(9)	0.065(5)	0.075(11)
0.740	0.495(20)	1.412(65)	0.152(6)	0.249(19)	0.007(9)	0.058(4)	0.075(10)
0.891	0.439(20)	1.101(66)	0.136(7)	0.186(20)	0.015(11)	0.045(5)	0.039(15)
0.901	0.397(41)	1.065(180)	0.128(13)	0.155(42)	0.034(19)	0.047(6)	0.044(22)
0.996	0.426(19)	1.131(51)	0.142(7)	0.232(17)	-0.001(9)	...	0.053(7)
1.089	0.391(23)	0.938(63)	0.124(8)	0.172(17)	0.011(7)	0.053(5)	0.046(12)
1.189	0.359(26)	0.867(71)	0.127(9)	0.143(22)	-0.001(10)	0.049(5)	0.046(11)
1.238	0.356(18)	0.939(43)	0.125(7)	0.207(14)	-0.004(6)	0.047(5)	0.055(9)

TABLE IX. Results for the isovector unpolarized generalized form factors for dataset 4.

$-t[\text{GeV}^2]$	A_{10}^{u-d}	B_{10}^{u-d}	A_{20}^{u-d}	B_{20}^{u-d}	C_{20}^{u-d}	A_{30}^{u-d}	B_{30}^{u-d}
0.000	1.000(2)	...	0.214(7)	0.070(8)	...
0.188	0.548(129)	3.044(876)	0.202(46)	0.505(205)	-0.059(262)	0.074(28)	0.045(165)
0.240	0.753(13)	2.281(96)	0.190(6)	0.307(30)	-0.015(21)	0.071(5)	0.059(20)
0.241	0.765(60)	2.335(250)	0.182(14)	0.309(56)	0.091(57)	0.066(6)	0.095(28)
0.394	0.529(110)	1.927(522)	0.143(31)	0.188(118)	0.119(81)	0.047(16)	0.001(71)
0.465	0.601(19)	1.696(83)	0.173(7)	0.271(26)	-0.020(12)	0.070(6)	0.072(16)
0.469	0.630(57)	2.034(223)	0.161(14)	0.311(52)	0.003(32)	0.066(7)	0.083(28)
0.498	0.595(28)	1.642(99)	0.171(8)	0.272(28)	-0.011(15)	0.067(6)	0.093(15)
0.678	0.505(27)	1.306(95)	0.159(9)	0.208(29)	-0.024(13)	0.063(8)	0.072(19)
0.739	0.501(30)	1.273(94)	0.147(8)	0.224(28)	0.015(14)	0.061(6)	0.063(14)
0.880	0.420(38)	1.113(126)	0.138(14)	0.196(37)	0.012(17)	0.062(11)	0.032(28)
0.892	0.549(115)	1.470(396)	0.152(32)	0.202(83)	-0.036(45)	0.062(15)	0.052(39)
0.996	0.400(28)	1.018(70)	0.124(10)	0.159(26)	0.007(13)	...	0.030(11)
1.072	0.376(34)	0.840(96)	0.115(12)	0.148(30)	0.010(11)	0.055(8)	0.052(21)
1.183	0.462(58)	0.800(143)	0.140(17)	0.159(43)	0.000(17)	0.057(10)	0.066(22)
1.237	0.347(25)	0.737(54)	0.118(9)	0.163(21)	0.007(9)	0.041(8)	0.048(15)

TABLE X. Results for the isovector unpolarized generalized form factors for dataset 5.

$-t[\text{GeV}^2]$	A_{10}^{u-d}	B_{10}^{u-d}	A_{20}^{u-d}	B_{20}^{u-d}	C_{20}^{u-d}	A_{30}^{u-d}	B_{30}^{u-d}
0.000	1.000(3)	...	0.205(14)	0.063(16)	...
0.177	0.387(251)	2.385(1.795)	0.095(79)	0.717(475)	0.129(518)	-0.033(63)	0.537(408)
0.238	0.723(24)	1.957(166)	0.172(11)	0.282(49)	-0.025(36)	0.049(11)	0.020(40)
0.240	0.587(97)	1.541(396)	0.135(20)	0.262(91)	-0.095(93)	0.063(12)	0.045(52)
0.378
0.459	0.604(35)	1.566(137)	0.156(12)	0.221(44)	0.009(22)	0.043(12)	0.065(33)
0.464	0.502(100)	1.072(373)	0.131(25)	0.344(97)	0.047(65)	0.052(15)	0.069(52)
0.498	0.466(42)	1.191(149)	0.127(12)	0.152(40)	0.001(29)	0.037(10)	0.025(29)
0.665	0.491(51)	1.228(166)	0.134(17)	0.219(51)	-0.034(27)	0.004(18)	0.011(40)
0.738	0.368(54)	1.091(156)	0.126(15)	0.206(46)	0.071(32)	0.033(11)	0.045(30)
0.858	0.349(67)	0.540(208)	0.115(25)	0.203(74)	0.010(34)	0.012(24)	0.048(61)
0.875
0.996	0.377(60)	0.606(121)	0.135(22)	0.166(50)	-0.009(25)	...	0.036(22)
1.042
1.173	0.270(75)	0.411(176)	0.112(25)	0.057(53)	-0.054(29)	0.036(13)	0.039(34)
1.235	0.291(42)	0.589(88)	0.090(16)	0.074(31)	-0.019(14)	0.027(16)	0.014(25)

TABLE XI. Results for the isovector unpolarized generalized form factors for dataset 6.

$-t[\text{GeV}^2]$	A_{10}^{u-d}	B_{10}^{u-d}	A_{20}^{u-d}	B_{20}^{u-d}	C_{20}^{u-d}	A_{30}^{u-d}	B_{30}^{u-d}
0.000	1.000(4)	...	0.206(14)	0.078(16)	...
0.107	1.035(192)	3.055(997)	0.190(45)	0.032(253)	-0.083(435)	0.060(32)	-0.303(221)
0.124	0.850(19)	2.756(233)	0.197(11)	0.331(59)	-0.097(54)	0.070(10)	0.099(46)
0.125	0.829(84)	2.262(376)	0.192(20)	0.284(110)	-0.017(113)	0.072(12)	0.094(62)
0.219	0.868(190)	2.749(823)	0.167(42)	0.182(169)	0.026(130)	0.063(24)	-0.084(109)
0.244	0.767(28)	2.330(193)	0.177(11)	0.298(49)	-0.015(28)	0.063(10)	0.091(34)
0.245	0.733(79)	1.883(328)	0.179(20)	0.137(93)	-0.164(73)	0.068(12)	0.099(64)
0.254	0.678(39)	2.074(219)	0.179(14)	0.273(61)	0.004(43)	0.081(13)	0.067(42)
0.359	0.693(36)	1.910(170)	0.161(12)	0.251(50)	0.005(33)	0.061(12)	0.087(36)
0.379	0.584(40)	1.786(192)	0.158(14)	0.250(52)	0.010(39)	0.067(11)	0.040(36)
0.471	0.617(42)	1.625(185)	0.162(15)	0.140(57)	-0.009(35)	0.064(14)	0.019(50)
0.473	0.551(91)	1.910(448)	0.155(28)	0.116(107)	-0.030(56)	0.077(17)	0.065(67)
0.508	0.602(56)	1.533(172)	0.185(21)	0.227(64)	-0.024(46)	...	0.044(26)
0.578	0.561(45)	1.447(150)	0.155(15)	0.188(43)	-0.028(20)	0.068(13)	0.031(34)
0.615	0.478(49)	1.324(186)	0.135(17)	0.117(59)	-0.060(34)	0.068(13)	0.012(37)
0.632	0.512(45)	1.268(131)	0.173(18)	0.193(46)	-0.040(25)	0.076(17)	0.002(36)

TABLE XII. Results for the isosinglet unpolarized generalized form factors for dataset 1.

$-t[\text{GeV}^2]$	A_{10}^{u+d}	B_{10}^{u+d}	A_{20}^{u+d}	B_{20}^{u+d}	C_{20}^{u+d}	A_{30}^{u+d}	B_{30}^{u+d}
0.000	3.000(2)	...	0.590(5)	0.176(7)	...
0.203	2.068(180)	-0.828(581)	0.473(40)	-0.230(145)	-0.201(196)	0.178(19)	-0.123(95)
0.243	2.229(14)	0.067(67)	0.506(5)	-0.024(20)	-0.130(19)	0.163(4)	-0.009(13)
0.243	2.067(71)	0.083(150)	0.473(15)	-0.067(44)	-0.086(51)	0.158(6)	-0.024(20)
0.420	1.649(153)	-0.380(350)	0.398(35)	-0.178(91)	-0.056(53)	0.137(14)	-0.082(45)
0.475	1.756(17)	0.008(60)	0.437(5)	-0.042(19)	-0.090(10)	0.144(5)	-0.013(12)
0.477	1.633(63)	0.117(135)	0.415(15)	-0.044(43)	-0.116(23)	0.143(7)	-0.024(19)
0.498	1.689(28)	0.148(78)	0.428(7)	-0.001(23)	-0.062(12)	0.148(5)	-0.007(14)
0.697	1.430(24)	-0.026(64)	0.383(7)	-0.048(20)	-0.072(10)	0.132(7)	-0.015(13)
0.741	1.342(28)	0.147(72)	0.371(8)	0.000(21)	-0.057(10)	0.129(5)	-0.009(12)
0.911	1.177(34)	0.049(78)	0.345(9)	-0.040(24)	-0.086(13)	0.120(8)	0.002(16)
0.918	1.105(61)	0.112(156)	0.316(17)	-0.067(44)	-0.100(26)	0.117(8)	-0.015(21)
0.996	1.157(25)	0.098(64)	0.343(8)	0.003(24)	-0.074(11)	...	0.061(8)
1.117	0.992(35)	0.024(71)	0.303(10)	-0.040(21)	-0.066(9)	0.111(7)	-0.009(13)
1.199	0.911(35)	0.086(80)	0.281(10)	-0.016(24)	-0.053(11)	0.100(6)	0.009(13)
1.239	0.955(24)	0.090(52)	0.301(8)	-0.009(18)	-0.058(7)	0.110(6)	-0.004(12)

TABLE XIII. Results for the isosinglet unpolarized generalized form factors for dataset 2.

$-t[\text{GeV}^2]$	A_{10}^{u+d}	B_{10}^{u+d}	A_{20}^{u+d}	B_{20}^{u+d}	C_{20}^{u+d}	A_{30}^{u+d}	B_{30}^{u+d}
0.000	3.000(3)	...	0.577(7)	0.170(9)	...
0.200	2.286(222)	0.641(651)	0.478(51)	-0.010(188)	0.077(243)	0.131(26)	-0.029(131)
0.242	2.227(17)	0.049(88)	0.496(6)	-0.035(27)	-0.119(25)	0.152(5)	-0.033(17)
0.243	2.134(91)	0.186(183)	0.474(19)	-0.009(50)	-0.125(63)	0.153(8)	-0.022(25)
0.414	1.773(178)	0.352(392)	0.416(42)	0.083(95)	-0.087(67)	0.124(16)	0.064(49)
0.473	1.763(23)	0.055(75)	0.431(7)	0.000(23)	-0.081(11)	0.137(7)	-0.006(15)
0.475	1.666(86)	0.191(179)	0.403(19)	-0.048(50)	-0.093(30)	0.138(8)	-0.014(26)
0.498	1.684(36)	0.001(98)	0.419(10)	-0.050(27)	-0.069(16)	0.136(6)	-0.055(19)
0.693	1.430(34)	0.073(79)	0.383(10)	0.013(25)	-0.068(12)	0.128(9)	0.010(17)
0.741	1.336(38)	0.049(88)	0.357(10)	-0.035(26)	-0.069(14)	0.123(6)	-0.040(16)
0.904	1.229(48)	0.009(99)	0.334(14)	-0.026(31)	-0.045(18)	0.114(9)	-0.020(23)
0.911	1.193(119)	-0.001(229)	0.347(32)	-0.040(68)	-0.035(39)	0.129(13)	-0.046(35)
0.996	1.094(33)	-0.023(73)	0.326(11)	-0.017(27)	-0.061(13)	...	0.059(10)
1.106	1.023(49)	-0.008(83)	0.299(15)	-0.007(24)	-0.040(13)	0.102(10)	-0.001(17)
1.195	0.925(57)	-0.067(120)	0.292(16)	-0.021(36)	-0.033(17)	0.107(9)	-0.031(20)
1.238	0.916(31)	-0.045(65)	0.292(10)	-0.025(21)	-0.050(9)	0.107(7)	-0.018(15)

TABLE XIV. Results for the isosinglet unpolarized generalized form factors for dataset 3.

$-t[\text{GeV}^2]$	A_{10}^{u+d}	B_{10}^{u+d}	A_{20}^{u+d}	B_{20}^{u+d}	C_{20}^{u+d}	A_{30}^{u+d}	B_{30}^{u+d}
0.000	3.000(3)	...	0.565(7)	0.171(9)	...
0.193	2.036(204)	0.517(614)	0.429(47)	-0.111(175)	-0.034(247)	0.111(23)	-0.086(131)
0.241	2.172(16)	-0.034(82)	0.482(6)	-0.002(24)	-0.110(20)	0.159(5)	-0.014(18)
0.242	2.047(87)	0.024(170)	0.456(18)	0.012(50)	-0.094(57)	0.152(7)	-0.012(25)
0.403	1.578(169)	0.071(377)	0.382(41)	-0.040(95)	-0.113(71)	0.123(17)	0.001(54)
0.469	1.688(23)	-0.023(70)	0.420(7)	-0.019(22)	-0.092(11)	0.143(6)	-0.014(14)
0.472	1.608(80)	-0.156(161)	0.401(19)	0.005(50)	-0.049(29)	0.143(9)	-0.014(26)
0.498	1.615(33)	0.002(81)	0.402(9)	0.017(25)	-0.048(14)	0.138(5)	0.003(16)
0.685	1.365(35)	-0.065(75)	0.369(10)	-0.010(25)	-0.072(13)	0.133(9)	-0.013(16)
0.740	1.268(35)	-0.048(81)	0.351(10)	-0.010(25)	-0.042(13)	0.125(6)	0.006(15)
0.891	1.067(39)	-0.116(85)	0.316(12)	-0.057(28)	-0.054(16)	0.098(10)	-0.052(21)
0.901	0.979(81)	0.123(180)	0.292(23)	-0.051(60)	-0.013(30)	0.102(11)	0.007(32)
0.996	1.036(31)	-0.024(67)	0.317(11)	-0.011(25)	-0.050(12)	...	0.056(10)
1.089	0.882(46)	-0.111(74)	0.286(14)	-0.039(25)	-0.046(11)	0.106(10)	-0.029(17)
1.189	0.874(47)	-0.098(91)	0.279(15)	-0.033(30)	-0.041(15)	0.096(8)	-0.003(17)
1.238	0.841(29)	-0.041(56)	0.273(10)	-0.008(19)	-0.042(8)	0.103(7)	-0.001(14)

TABLE XV. Results for the isosinglet unpolarized generalized form factors for dataset 4.

$-t[\text{GeV}^2]$	A_{10}^{u+d}	B_{10}^{u+d}	A_{20}^{u+d}	B_{20}^{u+d}	C_{20}^{u+d}	A_{30}^{u+d}	B_{30}^{u+d}
0.000	3.000(3)	...	0.530(12)	0.149(14)	...
0.188	1.817(355)	-1.870(1.160)	0.429(84)	-0.034(281)	-0.254(389)	0.126(39)	-0.019(243)
0.240	2.127(26)	-0.167(128)	0.459(9)	-0.025(39)	-0.173(30)	0.150(8)	-0.007(29)
0.241	2.098(153)	0.165(296)	0.442(30)	0.078(76)	-0.022(89)	0.134(11)	0.038(43)
0.394	1.382(262)	-0.670(677)	0.319(59)	-0.007(153)	0.038(110)	0.071(23)	-0.110(94)
0.465	1.632(35)	-0.085(113)	0.398(10)	-0.002(35)	-0.090(18)	0.131(9)	0.000(24)
0.469	1.611(130)	-0.008(263)	0.383(30)	0.067(70)	-0.121(49)	0.119(11)	0.007(40)
0.498	1.521(55)	0.016(131)	0.385(15)	0.054(37)	-0.104(21)	0.132(9)	0.066(25)
0.678	1.317(50)	-0.180(116)	0.346(14)	-0.033(38)	-0.064(21)	0.119(13)	0.005(28)
0.739	1.225(59)	0.033(131)	0.334(15)	0.051(37)	-0.056(20)	0.115(9)	0.038(23)
0.880	1.090(79)	0.081(152)	0.316(23)	-0.006(54)	-0.058(26)	0.116(17)	-0.046(44)
0.892	1.246(232)	0.252(387)	0.375(68)	0.063(105)	-0.182(79)	0.143(29)	0.070(63)
0.996	0.960(45)	0.026(101)	0.284(16)	-0.067(38)	-0.095(21)	...	0.019(16)
1.072	0.878(68)	-0.009(122)	0.245(20)	-0.041(40)	-0.026(18)	0.096(14)	-0.018(29)
1.183	0.960(113)	0.032(182)	0.292(31)	0.068(58)	-0.068(28)	0.106(17)	0.051(33)
1.237	0.789(39)	-0.024(81)	0.246(14)	-0.015(29)	-0.038(13)	0.076(13)	0.007(22)

TABLE XVI. Results for the isosinglet unpolarized generalized form factors for dataset 5.

$-t[\text{GeV}^2]$	A_{10}^{u+d}	B_{10}^{u+d}	A_{20}^{u+d}	B_{20}^{u+d}	C_{20}^{u+d}	A_{30}^{u+d}	B_{30}^{u+d}
0.000	3.000(5)	...	0.522(23)	0.153(25)	...
0.177	1.231(560)	-1.770(2.373)	0.355(168)	-0.324(575)	-0.461(825)	0.189(112)	0.033(574)
0.238	2.030(48)	-0.140(211)	0.426(18)	-0.026(62)	-0.210(58)	0.154(16)	-0.028(55)
0.240	1.767(225)	-0.592(516)	0.378(43)	0.049(125)	-0.133(136)	0.145(20)	0.055(80)
0.378
0.459	1.503(55)	-0.013(184)	0.367(18)	0.013(61)	-0.097(33)	0.129(19)	-0.082(45)
0.464	1.328(202)	-0.943(508)	0.360(52)	0.144(122)	-0.090(93)	0.115(22)	0.012(73)
0.498	1.325(89)	0.049(201)	0.331(22)	-0.036(57)	-0.080(40)	0.098(16)	-0.054(40)
0.665	1.157(85)	0.040(208)	0.298(30)	0.103(73)	-0.074(38)	0.070(25)	-0.087(56)
0.738	1.067(101)	0.140(212)	0.311(28)	0.090(64)	0.003(39)	0.111(21)	-0.013(43)
0.858	0.948(119)	-0.136(266)	0.244(37)	-0.014(100)	-0.081(49)	0.073(36)	-0.066(83)
0.875
0.996	0.865(86)	-0.173(175)	0.315(36)	-0.048(66)	-0.093(38)	...	0.057(31)
1.042
1.173	0.686(113)	-0.033(235)	0.196(35)	-0.073(70)	-0.041(39)	0.070(21)	-0.005(46)
1.235	0.593(65)	0.073(118)	0.212(23)	-0.065(42)	-0.043(21)	0.092(22)	-0.017(37)

TABLE XVII. Results for the isosinglet unpolarized generalized form factors for dataset 6.

$-t[\text{GeV}^2]$	A_{10}^{u+d}	B_{10}^{u+d}	A_{20}^{u+d}	B_{20}^{u+d}	C_{20}^{u+d}	A_{30}^{u+d}	B_{30}^{u+d}
0.000	3.000(6)	...	0.510(24)	0.164(26)	...
0.107	2.610(460)	3.374(1.535)	0.516(89)	-0.379(418)	-0.766(673)	0.139(50)	-0.325(359)
0.124	2.437(35)	-0.087(285)	0.468(20)	-0.071(90)	-0.334(76)	0.131(18)	0.091(71)
0.125	2.465(229)	-0.247(499)	0.458(40)	0.071(139)	-0.156(202)	0.140(20)	-0.060(90)
0.219	2.445(482)	1.221(1.054)	0.497(93)	0.025(268)	-0.560(221)	0.159(41)	-0.094(165)
0.244	2.067(42)	-0.102(238)	0.412(19)	-0.045(71)	-0.119(41)	0.110(19)	0.043(52)
0.245	2.113(213)	-0.505(455)	0.422(40)	-0.112(124)	-0.250(103)	0.130(20)	0.025(84)
0.254	1.956(91)	-0.355(327)	0.405(24)	-0.058(89)	-0.061(62)	0.137(22)	0.072(67)
0.359	1.763(54)	-0.237(229)	0.366(20)	-0.061(69)	-0.091(44)	0.094(21)	0.066(52)
0.379	1.644(91)	-0.475(274)	0.363(24)	-0.069(77)	-0.077(48)	0.101(17)	0.055(58)
0.471	1.541(72)	-0.274(261)	0.357(24)	-0.120(79)	-0.117(49)	0.102(23)	0.021(71)
0.473	1.601(234)	0.283(552)	0.372(52)	0.097(148)	-0.151(80)	0.120(24)	-0.011(91)
0.508	1.468(81)	-0.035(253)	0.362(30)	-0.117(83)	-0.101(61)	...	0.101(42)
0.578	1.318(68)	-0.286(204)	0.324(24)	-0.060(65)	-0.100(32)	0.100(22)	0.001(53)
0.615	1.306(104)	-0.386(290)	0.292(25)	-0.057(79)	-0.112(43)	0.086(18)	-0.022(52)
0.632	1.257(73)	-0.104(188)	0.315(24)	-0.062(60)	-0.055(33)	0.093(24)	0.066(55)

TABLE XVIII. Results for the isovector polarized generalized form factors for dataset 1.

$-t[\text{GeV}^2]$	\tilde{A}_{10}^{u-d}	\tilde{B}_{10}^{u-d}	\tilde{A}_{20}^{u-d}	\tilde{B}_{20}^{u-d}	\tilde{A}_{30}^{u-d}	\tilde{B}_{30}^{u-d}
0.000	1.141(12)	...	0.280(4)	...	0.100(2)	...
0.203	0.963(91)	...	0.244(22)	...	0.087(10)	...
0.243	0.973(12)	9.251(403)	0.256(4)	0.740(136)	0.093(2)	0.066(71)
0.243	0.930(37)	9.159(853)	0.234(10)	0.562(286)	0.086(4)	0.090(120)
0.420	0.786(80)	4.361(1.326)	0.216(21)	0.303(343)	0.081(9)	0.129(186)
0.475	0.849(13)	6.514(227)	0.231(4)	0.497(71)	0.085(2)	0.063(39)
0.477	0.780(37)	5.515(570)	0.208(10)	0.390(161)	0.078(4)	0.017(78)
0.498	0.831(18)	6.798(305)	0.226(5)	0.539(107)	0.084(2)	0.188(55)
0.697	0.742(17)	4.682(232)	0.211(6)	0.432(81)	0.079(3)	0.094(46)
0.741	0.713(18)	4.604(222)	0.203(6)	0.445(81)	0.077(3)	0.164(48)
0.911	0.683(24)	3.913(286)	0.203(8)	0.486(116)	0.081(4)	0.117(64)
0.918	0.595(45)	3.175(512)	0.173(15)	0.241(204)	0.070(6)	0.006(100)
0.996	0.658(17)	...	0.198(6)
1.117	0.575(23)	2.690(176)	0.176(8)	0.254(67)	0.070(3)	0.052(37)
1.199	0.575(27)	2.806(225)	0.171(9)	0.366(93)	0.070(4)	0.149(51)
1.239	0.584(17)	2.866(147)	0.181(6)	0.216(68)	0.068(3)	0.068(43)

TABLE XIX. Results for the isovector polarized generalized form factors for dataset 2.

$-t[\text{GeV}^2]$	\tilde{A}_{10}^{u-d}	\tilde{B}_{10}^{u-d}	\tilde{A}_{20}^{u-d}	\tilde{B}_{20}^{u-d}	\tilde{A}_{30}^{u-d}	\tilde{B}_{30}^{u-d}
0.000	1.136(18)	...	0.278(6)	...	0.100(3)	...
0.200	1.115(124)	...	0.236(27)	...	0.097(14)	...
0.242	0.967(16)	9.891(469)	0.253(5)	0.562(177)	0.095(3)	-0.028(93)
0.243	0.974(51)	10.370(1.088)	0.237(12)	0.277(298)	0.087(5)	0.007(146)
0.414	0.902(107)	6.917(1.552)	0.217(26)	-0.199(414)	0.082(11)	-0.091(246)
0.473	0.848(16)	6.654(253)	0.231(6)	0.442(96)	0.087(3)	-0.053(50)
0.475	0.819(49)	6.279(672)	0.220(13)	0.391(195)	0.080(5)	0.061(91)
0.498	0.828(23)	6.481(360)	0.224(7)	0.383(127)	0.085(3)	0.033(74)
0.693	0.736(22)	4.549(262)	0.214(8)	0.380(90)	0.085(4)	-0.015(67)
0.741	0.710(24)	4.508(266)	0.199(7)	0.278(106)	0.075(4)	0.025(60)
0.904	0.691(32)	3.778(377)	0.191(11)	0.232(169)	0.081(6)	-0.085(94)
0.911	0.738(85)	4.214(829)	0.170(24)	-0.070(306)	0.075(11)	-0.022(161)
0.996	0.621(22)	...	0.189(7)
1.106	0.580(28)	2.733(228)	0.173(10)	0.212(92)	0.070(5)	-0.031(54)
1.195	0.565(37)	2.342(288)	0.174(12)	0.110(130)	0.067(6)	-0.004(76)
1.238	0.559(20)	2.640(168)	0.173(7)	0.187(85)	0.071(4)	-0.076(55)

TABLE XX. Results for the isovector polarized generalized form factors for dataset 3.

$-t[\text{GeV}^2]$	\tilde{A}_{10}^{u-d}	\tilde{B}_{10}^{u-d}	\tilde{A}_{20}^{u-d}	\tilde{B}_{20}^{u-d}	\tilde{A}_{30}^{u-d}	\tilde{B}_{30}^{u-d}
0.000	1.171(18)	...	0.280(7)	...	0.101(3)	...
0.193	0.926(117)	...	0.212(27)	...	0.068(15)	...
0.241	0.967(16)	9.646(437)	0.250(5)	0.601(166)	0.092(3)	0.102(89)
0.242	0.934(49)	9.656(1.001)	0.238(12)	0.684(315)	0.089(5)	0.171(139)
0.403	0.784(99)	5.562(1.440)	0.185(25)	0.581(359)	0.074(11)	0.324(245)
0.469	0.854(18)	6.667(257)	0.223(6)	0.484(73)	0.083(3)	0.067(49)
0.472	0.827(52)	6.440(675)	0.214(14)	0.495(189)	0.079(6)	0.044(101)
0.498	0.811(23)	6.543(317)	0.222(7)	0.479(109)	0.085(3)	0.094(68)
0.685	0.739(24)	4.501(237)	0.207(8)	0.446(75)	0.078(4)	0.068(68)
0.740	0.711(26)	4.575(247)	0.205(8)	0.505(92)	0.079(4)	0.100(62)
0.891	0.592(28)	2.686(304)	0.176(10)	0.205(142)	0.061(6)	-0.102(87)
0.901	0.669(79)	3.465(693)	0.172(23)	0.315(242)	0.060(11)	-0.068(129)
0.996	0.579(22)	...	0.180(8)
1.089	0.562(31)	2.414(208)	0.170(10)	0.317(75)	0.061(5)	0.039(47)
1.189	0.551(37)	2.328(246)	0.166(12)	0.297(107)	0.067(6)	0.117(65)
1.238	0.529(22)	2.445(160)	0.167(7)	0.297(72)	0.061(4)	0.033(51)

TABLE XXI. Results for the isovector polarized generalized form factors for dataset 4.

$-t[\text{GeV}^2]$	\tilde{A}_{10}^{u-d}	\tilde{B}_{10}^{u-d}	\tilde{A}_{20}^{u-d}	\tilde{B}_{20}^{u-d}	\tilde{A}_{30}^{u-d}	\tilde{B}_{30}^{u-d}
0.000	1.162(32)	...	0.257(10)	...	0.091(6)	...
0.188	0.931(204)	...	0.224(49)	...	0.082(31)	...
0.240	0.945(26)	9.410(668)	0.228(8)	0.357(248)	0.088(5)	0.034(152)
0.241	0.934(80)	9.110(1.700)	0.222(21)	-0.132(487)	0.078(9)	-0.411(227)
0.394	0.710(166)	4.255(2.373)	0.184(43)	-0.140(627)	0.087(21)	0.741(418)
0.465	0.815(27)	6.498(379)	0.214(9)	0.457(135)	0.086(5)	0.236(82)
0.469	0.894(86)	7.418(1.076)	0.218(23)	0.616(293)	0.078(10)	0.100(154)
0.498	0.797(36)	6.362(470)	0.195(10)	0.297(184)	0.078(5)	-0.006(102)
0.678	0.740(37)	4.611(376)	0.210(11)	0.495(133)	0.082(7)	0.217(115)
0.739	0.696(38)	4.407(354)	0.192(12)	0.570(152)	0.072(6)	0.245(102)
0.880	0.564(51)	2.530(492)	0.156(16)	-0.081(218)	0.062(12)	0.011(151)
0.892	0.898(206)	4.339(1.694)	0.232(56)	-0.070(658)	0.041(21)	-0.385(290)
0.996	0.574(33)	...	0.174(12)
1.072	0.471(45)	1.935(280)	0.144(15)	0.096(105)	0.058(8)	0.089(73)
1.183	0.519(71)	2.172(415)	0.139(22)	-0.011(177)	0.056(12)	0.023(118)
1.237	0.475(28)	1.999(229)	0.152(11)	0.131(120)	0.071(6)	0.038(80)

TABLE XXII. Results for the isovector polarized generalized form factors for dataset 5.

$-t[\text{GeV}^2]$	\tilde{A}_{10}^{u-d}	\tilde{B}_{10}^{u-d}	\tilde{A}_{20}^{u-d}	\tilde{B}_{20}^{u-d}	\tilde{A}_{30}^{u-d}	\tilde{B}_{30}^{u-d}
0.000	1.208(60)	...	0.244(19)	...	0.090(11)	...
0.177	0.557(398)	...	0.172(96)	...	0.189(90)	...
0.238	0.954(46)	11.827(1.139)	0.227(14)	-0.112(427)	0.099(10)	-0.019(302)
0.240	1.105(152)	14.903(3.016)	0.239(37)	0.651(848)	0.088(19)	0.389(475)
0.378
0.459	0.810(48)	6.659(597)	0.208(15)	0.430(217)	0.082(10)	-0.087(168)
0.464	0.974(168)	7.646(1.750)	0.214(43)	0.533(527)	0.095(23)	0.539(307)
0.498	0.712(58)	5.767(709)	0.203(18)	0.488(287)	0.095(10)	0.301(187)
0.665	0.665(65)	4.181(577)	0.201(24)	0.500(245)	0.090(16)	0.397(246)
0.738	0.622(72)	3.650(657)	0.208(25)	0.475(298)	0.094(14)	0.201(212)
0.858	0.624(109)	3.380(767)	0.164(35)	0.134(318)	0.072(28)	0.346(249)
0.875
0.996	0.486(64)	...	0.158(25)
1.042
1.173	0.481(106)	2.296(589)	0.177(37)	0.305(285)	0.067(21)	0.041(197)
1.235	0.408(50)	1.486(335)	0.137(18)	0.114(199)	0.059(11)	0.090(147)

TABLE XXIII. Results for the isovector polarized generalized form factors for dataset 6.

$-t[\text{GeV}^2]$	\tilde{A}_{10}^{u-d}	\tilde{B}_{10}^{u-d}	\tilde{A}_{20}^{u-d}	\tilde{B}_{20}^{u-d}	\tilde{A}_{30}^{u-d}	\tilde{B}_{30}^{u-d}
0.000	1.187(64)	...	0.252(20)	...	0.083(12)	...
0.107	1.203(223)	...	0.262(51)	...	0.064(37)	...
0.124	1.070(53)	17.234(1.595)	0.237(17)	0.623(598)	0.083(10)	0.551(391)
0.125	1.150(117)	19.686(3.278)	0.251(28)	2.059(839)	0.080(13)	-0.454(561)
0.219	1.333(295)	16.441(5.731)	0.276(58)	1.696(1.095)	0.086(28)	-0.340(878)
0.244	1.037(55)	13.098(1.010)	0.230(16)	0.808(299)	0.080(10)	0.369(186)
0.245	1.055(113)	13.658(2.080)	0.250(28)	1.879(558)	0.091(14)	0.745(381)
0.254	0.983(66)	12.490(1.361)	0.218(19)	0.918(431)	0.088(10)	0.471(326)
0.359	0.935(56)	9.315(870)	0.217(16)	0.755(268)	0.074(10)	0.108(238)
0.379	0.903(64)	8.869(919)	0.214(19)	1.001(360)	0.087(11)	0.403(283)
0.471	0.841(66)	7.041(992)	0.223(22)	0.900(390)	0.067(14)	-0.100(289)
0.473	0.896(181)	7.785(2.274)	0.260(53)	1.557(725)	0.064(26)	-0.415(419)
0.508	0.815(68)	...	0.203(23)
0.578	0.813(64)	5.751(647)	0.204(20)	0.663(233)	0.075(12)	0.314(144)
0.615	0.751(84)	5.191(847)	0.174(24)	0.643(351)	0.077(14)	0.219(210)
0.632	0.776(60)	5.401(642)	0.192(19)	0.403(295)	0.081(11)	-0.098(226)

TABLE XXIV. Results for the isosinglet polarized generalized form factors for dataset 1.

$-t[\text{GeV}^2]$	\tilde{A}_{10}^{u+d}	\tilde{B}_{10}^{u+d}	\tilde{A}_{20}^{u+d}	\tilde{B}_{20}^{u+d}	\tilde{A}_{30}^{u+d}	\tilde{B}_{30}^{u+d}
0.000	0.623(17)	...	0.170(6)	...	0.061(3)	...
0.203	0.497(79)	...	0.138(22)	...	0.057(14)	...
0.243	0.537(14)	5.234(429)	0.158(5)	0.657(161)	0.058(3)	0.186(96)
0.243	0.485(31)	4.941(958)	0.144(10)	0.676(308)	0.052(4)	0.046(152)
0.420	0.425(75)	2.380(1.559)	0.136(22)	0.624(461)	0.056(10)	0.210(277)
0.475	0.477(15)	4.086(272)	0.145(6)	0.545(107)	0.055(3)	0.096(54)
0.477	0.414(38)	3.397(726)	0.122(11)	0.304(243)	0.047(5)	0.014(113)
0.498	0.458(18)	3.924(375)	0.142(6)	0.559(144)	0.054(3)	0.198(79)
0.697	0.413(19)	2.776(283)	0.134(7)	0.430(111)	0.054(3)	0.142(67)
0.741	0.388(21)	2.681(305)	0.127(7)	0.469(128)	0.049(3)	0.184(74)
0.911	0.404(25)	2.561(305)	0.125(9)	0.429(127)	0.048(5)	0.120(85)
0.918	0.344(50)	2.056(605)	0.110(18)	0.282(240)	0.042(8)	0.035(115)
0.996	0.365(19)	...	0.124(7)
1.117	0.351(24)	1.945(214)	0.113(9)	0.297(92)	0.046(4)	0.073(50)
1.199	0.327(31)	1.522(279)	0.114(11)	0.357(129)	0.044(5)	0.141(68)
1.239	0.328(18)	1.711(189)	0.114(7)	0.308(107)	0.047(4)	0.072(62)

TABLE XXV. Results for the isosinglet polarized generalized form factors for dataset 2.

$-t[\text{GeV}^2]$	\tilde{A}_{10}^{u+d}	\tilde{B}_{10}^{u+d}	\tilde{A}_{20}^{u+d}	\tilde{B}_{20}^{u+d}	\tilde{A}_{30}^{u+d}	\tilde{B}_{30}^{u+d}
0.000	0.627(23)	...	0.169(8)	...	0.063(4)	...
0.200	0.663(107)	...	0.125(29)	...	0.065(18)	...
0.242	0.531(18)	5.042(498)	0.157(7)	0.471(205)	0.062(4)	0.073(123)
0.243	0.568(44)	5.822(1.170)	0.146(14)	0.163(373)	0.053(7)	0.053(179)
0.414	0.543(94)	2.378(1.841)	0.122(29)	-0.367(566)	0.048(13)	0.096(365)
0.473	0.480(20)	4.096(332)	0.145(8)	0.392(129)	0.054(4)	0.008(66)
0.475	0.535(47)	4.970(889)	0.131(15)	0.255(294)	0.047(7)	0.012(124)
0.498	0.468(24)	4.024(467)	0.143(8)	0.315(183)	0.055(4)	0.108(102)
0.693	0.426(26)	2.977(332)	0.133(9)	0.298(136)	0.049(5)	-0.027(91)
0.741	0.404(25)	2.785(339)	0.116(9)	0.050(159)	0.044(5)	-0.043(87)
0.904	0.353(34)	1.709(420)	0.122(12)	0.278(183)	0.056(7)	0.040(115)
0.911	0.383(86)	1.679(936)	0.113(28)	-0.079(339)	0.062(15)	0.172(177)
0.996	0.308(27)	...	0.121(10)
1.106	0.308(32)	1.375(285)	0.111(12)	0.165(111)	0.050(7)	0.135(64)
1.195	0.329(42)	1.266(381)	0.101(16)	0.036(180)	0.044(8)	0.060(102)
1.238	0.279(26)	1.679(259)	0.112(10)	0.259(130)	0.050(5)	0.057(78)

TABLE XXVI. Results for the isosinglet polarized generalized form factors for dataset 3.

$-t[\text{GeV}^2]$	\tilde{A}_{10}^{u+d}	\tilde{B}_{10}^{u+d}	\tilde{A}_{20}^{u+d}	\tilde{B}_{20}^{u+d}	\tilde{A}_{30}^{u+d}	\tilde{B}_{30}^{u+d}
0.000	0.580(24)	...	0.181(8)	...	0.072(4)	...
0.193	0.526(105)	...	0.131(31)	...	0.046(20)	...
0.241	0.515(18)	5.666(508)	0.158(7)	0.409(199)	0.062(4)	0.071(114)
0.242	0.514(43)	7.032(1.094)	0.153(13)	0.299(371)	0.064(6)	0.017(183)
0.403	0.450(97)	4.042(1.708)	0.132(29)	0.480(491)	0.041(15)	-0.056(362)
0.469	0.431(20)	3.438(295)	0.138(7)	0.245(108)	0.055(4)	0.016(67)
0.472	0.352(48)	2.286(768)	0.150(16)	0.592(275)	0.063(8)	0.123(155)
0.498	0.443(22)	3.463(362)	0.141(7)	0.102(158)	0.062(4)	0.140(96)
0.685	0.346(25)	1.935(296)	0.123(9)	0.208(122)	0.051(5)	0.058(91)
0.740	0.367(27)	2.274(330)	0.129(9)	0.130(146)	0.056(5)	0.082(88)
0.891	0.300(32)	1.278(328)	0.101(11)	-0.112(154)	0.036(8)	-0.255(123)
0.901	0.390(81)	2.274(733)	0.116(26)	0.087(271)	0.042(14)	-0.178(151)
0.996	0.295(25)	...	0.107(9)
1.089	0.258(32)	0.988(228)	0.099(11)	0.050(104)	0.037(7)	-0.066(71)
1.189	0.286(41)	1.023(311)	0.110(15)	0.076(149)	0.049(8)	0.098(89)
1.238	0.260(23)	1.149(202)	0.099(9)	0.084(124)	0.038(5)	0.034(75)

TABLE XXVII. Results for the isosinglet polarized generalized form factors for dataset 4.

$-t[\text{GeV}^2]$	\tilde{A}_{10}^{u+d}	\tilde{B}_{10}^{u+d}	\tilde{A}_{20}^{u+d}	\tilde{B}_{20}^{u+d}	\tilde{A}_{30}^{u+d}	\tilde{B}_{30}^{u+d}
0.000	0.598(38)	...	0.159(14)	...	0.064(8)	...
0.188	0.393(194)	...	0.177(56)	...	0.088(40)	...
0.240	0.474(30)	4.326(808)	0.143(11)	0.200(289)	0.059(7)	-0.008(204)
0.241	0.467(71)	6.043(1.796)	0.134(22)	-0.240(548)	0.054(11)	-0.291(284)
0.394	0.522(177)	5.751(2.875)	0.172(52)	0.146(821)	0.049(26)	-0.101(625)
0.465	0.427(33)	3.081(455)	0.136(12)	0.076(174)	0.057(7)	0.106(110)
0.469	0.419(81)	3.280(1.215)	0.148(27)	0.494(432)	0.064(12)	0.118(225)
0.498	0.394(36)	3.088(543)	0.124(12)	0.316(264)	0.052(7)	0.099(145)
0.678	0.407(45)	2.207(462)	0.133(15)	-0.143(200)	0.045(8)	-0.026(158)
0.739	0.433(47)	2.993(499)	0.126(15)	0.263(226)	0.049(8)	0.135(142)
0.880	0.336(56)	1.348(555)	0.108(21)	-0.253(281)	0.051(15)	-0.119(208)
0.892	0.463(164)	3.079(1.375)	0.178(57)	0.320(604)	0.043(29)	-0.369(374)
0.996	0.301(39)	...	0.109(15)
1.072	0.297(53)	0.992(358)	0.097(20)	-0.081(163)	0.035(11)	0.021(105)
1.183	0.213(77)	0.526(503)	0.096(28)	-0.094(262)	0.052(15)	-0.030(158)
1.237	0.248(34)	1.051(280)	0.083(14)	0.126(174)	0.042(8)	0.051(112)

TABLE XXVIII. Results for the isosinglet polarized generalized form factors for dataset 5.

$-t[\text{GeV}^2]$	\tilde{A}_{10}^{u+d}	\tilde{B}_{10}^{u+d}	\tilde{A}_{20}^{u+d}	\tilde{B}_{20}^{u+d}	\tilde{A}_{30}^{u+d}	\tilde{B}_{30}^{u+d}
0.000	0.519(68)	...	0.123(26)	...	0.049(16)	...
0.177	0.003(440)	...	-0.092(122)	...	0.268(131)	...
0.238	0.469(51)	7.022(1.388)	0.126(19)	-0.146(558)	0.065(14)	0.182(426)
0.240	0.604(146)	8.708(3.368)	0.094(42)	0.199(1.052)	0.031(25)	-0.209(618)
0.378
0.459	0.321(56)	2.498(733)	0.113(22)	0.069(314)	0.053(13)	-0.143(228)
0.464	0.536(170)	3.063(2.143)	0.113(56)	0.183(767)	0.033(29)	-0.064(436)
0.498	0.340(62)	2.307(873)	0.092(22)	0.114(422)	0.056(13)	0.088(290)
0.665	0.202(75)	1.395(771)	0.090(30)	0.180(357)	0.056(19)	0.648(331)
0.738	0.128(85)	-0.480(819)	0.057(29)	-0.626(415)	0.052(18)	-0.066(277)
0.858	0.312(124)	1.348(923)	0.109(46)	0.313(388)	0.114(41)	0.618(338)
0.875
0.996	0.234(74)	...	0.063(31)
1.042
1.173	0.337(124)	1.644(738)	0.095(44)	0.626(361)	0.072(29)	0.168(254)
1.235	0.172(54)	-0.034(422)	0.053(22)	-0.405(295)	0.046(16)	0.163(218)

TABLE XXIX. Results for the isosinglet polarized generalized form factors for dataset 6.

$-t[\text{GeV}^2]$	\tilde{A}_{10}^{u+d}	\tilde{B}_{10}^{u+d}	\tilde{A}_{20}^{u+d}	\tilde{B}_{20}^{u+d}	\tilde{A}_{30}^{u+d}	\tilde{B}_{30}^{u+d}
0.000	0.484(72)	...	0.143(25)	...	0.040(15)	...
0.107	0.732(209)	...	0.184(59)	...	0.045(41)	...
0.124	0.493(54)	11.813(1.845)	0.139(20)	0.832(668)	0.049(14)	0.673(521)
0.125	0.722(109)	16.409(3.651)	0.154(34)	0.730(1.118)	0.026(18)	-0.717(732)
0.219	0.867(246)	10.112(5.404)	0.226(61)	0.704(1.398)	0.046(35)	0.104(1.269)
0.244	0.500(58)	7.939(1.175)	0.141(20)	1.075(372)	0.048(13)	0.348(271)
0.245	0.544(118)	6.702(2.649)	0.176(38)	1.910(815)	0.067(18)	1.500(526)
0.254	0.503(67)	8.214(1.553)	0.123(25)	0.844(662)	0.038(13)	0.195(499)
0.359	0.478(63)	6.080(1.065)	0.147(22)	1.257(379)	0.050(13)	0.540(343)
0.379	0.427(73)	4.748(1.289)	0.128(26)	1.757(534)	0.045(14)	0.294(434)
0.471	0.379(74)	3.233(1.004)	0.122(25)	0.847(451)	0.068(21)	0.784(383)
0.473	0.558(178)	5.559(2.237)	0.153(57)	0.722(811)	0.057(36)	0.284(551)
0.508	0.456(75)	...	0.110(30)
0.578	0.399(76)	2.998(772)	0.113(24)	0.725(283)	0.051(17)	0.462(205)
0.615	0.348(93)	2.366(973)	0.083(33)	0.515(464)	0.039(20)	-0.024(295)
0.632	0.433(62)	4.459(837)	0.113(26)	0.926(457)	0.031(15)	-0.426(344)

[1] D. Müller, D. Robaschik, B. Geyer, F.M. Dittes, and J. Horejsi, Fortschr. Phys. **42**, 101 (1994).
 [2] X.-D. Ji, Phys. Rev. D **55**, 7114 (1997).
 [3] A. V. Radyushkin, Phys. Rev. D **56**, 5524 (1997).
 [4] M. Diehl, Phys. Rep. **388**, 41 (2003).
 [5] X.-D. Ji, Phys. Rev. Lett. **78**, 610 (1997).
 [6] M. Burkardt, Phys. Rev. D **62**, 071503 (2000).
 [7] S. Stepanyan *et al.* (CLAS), Phys. Rev. Lett. **87**, 182002 (2001).
 [8] A. Airapetian *et al.* (HERMES), Phys. Rev. Lett. **87**, 182001 (2001).
 [9] S. Chekanov *et al.* (ZEUS), Phys. Lett. B **573**, 46 (2003).
 [10] A. Aktas *et al.* (H1), Eur. Phys. J. C **44**, 1 (2005).
 [11] M. Diehl, T. Feldmann, R. Jakob, and P. Kroll, Eur. Phys. J. C **39**, 1 (2005).
 [12] M. Göckeler *et al.* (QCDSF), Phys. Rev. Lett. **92**, 042002 (2004).
 [13] P. Hägler *et al.* (LHPC), Phys. Rev. D **68**, 034505 (2003).
 [14] P. Hägler *et al.* (LHPC), Phys. Rev. Lett. **93**, 112001 (2004).
 [15] W. Schroers *et al.* (LHPC), Nucl. Phys. B, Proc. Suppl. **129**, 907 (2004).
 [16] M. Göckeler *et al.* (QCDSF), Phys. Lett. B **627**, 113 (2005).
 [17] M. Diehl *et al.* (QCDSF), arXiv:hep-ph/0511032.
 [18] M. Göckeler *et al.*, Phys. Rev. Lett. **98**, 222001 (2007).
 [19] D. B. Renner *et al.* (LHP), Nucl. Phys. B, Proc. Suppl. **140**, 255 (2005).
 [20] R. G. Edwards *et al.* (LHPC), Proc. Sci., LAT2005 (2005) 056.
 [21] M. Diehl, Eur. Phys. J. C **19**, 485 (2001).
 [22] P. Hägler, Phys. Lett. B **594**, 164 (2004).
 [23] D. Dolgov *et al.* (LHPC), Phys. Rev. D **66**, 034506 (2002).
 [24] M. Göckeler *et al.*, Phys. Rev. D **54**, 5705 (1996).
 [25] K. Orginos and D. Toussaint (MILC), Phys. Rev. D **59**, 014501 (1998).
 [26] K. Orginos, D. Toussaint, and R. L. Sugar (MILC), Phys. Rev. D **60**, 054503 (1999).
 [27] S. R. Sharpe, Proc. Sci., LAT2006 (2006) 022.
 [28] C. T. H. Davies *et al.* (HPQCD), Phys. Rev. Lett. **92**, 022001 (2004).
 [29] C. W. Bernard *et al.*, Phys. Rev. D **64**, 054506 (2001).
 [30] A. Hasenfratz and F. Knechtli, Phys. Rev. D **64**, 034504 (2001).
 [31] C. Aubin *et al.*, Phys. Rev. D **70**, 094505 (2004).
 [32] D. B. Kaplan, Phys. Lett. B **288**, 342 (1992).
 [33] Y. Shamir, Nucl. Phys. **B406**, 90 (1993).
 [34] R. Narayanan and H. Neuberger, Phys. Lett. B **302**, 62 (1993).
 [35] V. Furman and Y. Shamir, Nucl. Phys. **B439**, 54 (1995).
 [36] T. Blum *et al.*, Phys. Rev. D **69**, 074502 (2004).
 [37] T. Blum, Nucl. Phys. B, Proc. Suppl. **73**, 167 (1999).
 [38] T. Blum *et al.*, Phys. Rev. D **66**, 014504 (2002).
 [39] B. Bistrovic, Ph.D. thesis, MIT, 2005.
 [40] B. Bistrovic, R. Erwin, J. W. Negele, and M. Ramsey-Musolf (to be published).
 [41] K. Goeke, M. V. Polyakov, and M. Vanderhaeghen, Prog. Part. Nucl. Phys. **47**, 401 (2001).
 [42] S. J. Brodsky, M. Diehl, and D. S. Hwang, Nucl. Phys. **B596**, 99 (2001).
 [43] M. Diehl, T. Feldmann, R. Jakob, and P. Kroll, Nucl. Phys. **B596**, 33 (2001).
 [44] S. R. Beane, P. F. Bedaque, K. Orginos, and M. J. Savage (NPLQCD), Phys. Rev. D **73**, 054503 (2006).
 [45] S. R. Beane *et al.*, Phys. Rev. D **74**, 114503 (2006).
 [46] S. R. Beane, P. F. Bedaque, K. Orginos, and M. J. Savage, Phys. Rev. D **75**, 094501 (2007).
 [47] R. G. Edwards *et al.*, Proc. Sci. LAT2006 (2006) 121.
 [48] D. B. Renner *et al.* (LHPC/MILC Collaboration) (to be published).
 [49] T. R. Hemmert, M. Procura, and W. Weise, Phys. Rev. D **68**, 075009 (2003).

- [50] S. R. Beane and M. J. Savage, *Phys. Rev. D* **70**, 074029 (2004).
- [51] K. Akerstaff *et al.* (HERMES), *Phys. Lett. B* **464**, 123 (1999).
- [52] A. Airapetian *et al.* (HERMES), *Phys. Rev. D* **75**, 012007 (2007).
- [53] V. Y. Alexakhin *et al.* (COMPASS), *Phys. Lett. B* **647**, 8 (2007).
- [54] J.-W. Chen and X.-D. Ji, *Phys. Lett. B* **523**, 107 (2001).
- [55] J.-W. Chen and X.-D. Ji, *Phys. Rev. Lett.* **88**, 052003 (2002).
- [56] D. Arndt and M. J. Savage, *Nucl. Phys.* **A697**, 429 (2002).
- [57] W. Detmold, W. Melnitchouk, J. W. Negele, D. B. Renner, and A. W. Thomas, *Phys. Rev. Lett.* **87**, 172001 (2001).
- [58] A. V. Belitsky and X. Ji, *Phys. Lett. B* **538**, 289 (2002).
- [59] R. D. Young, D. B. Leinweber, and A. W. Thomas, *Prog. Part. Nucl. Phys.* **50**, 399 (2003).
- [60] W. Detmold and C. J. D. Lin, *Phys. Rev. D* **71**, 054510 (2005).
- [61] J.-W. Chen, D. O'Connell, R. S. Van de Water, and A. Walker-Loud, *Phys. Rev. D* **73**, 074510 (2006).
- [62] M. Diehl, A. Manashov, and A. Schäfer, *Eur. Phys. J. A* **31**, 335 (2007).
- [63] S.-i. Ando, J.-W. Chen, and C.-W. Kao, *Phys. Rev. D* **74**, 094013 (2006).
- [64] M. Diehl, A. Manashov, and A. Schäfer, *Eur. Phys. J. A* **29**, 315 (2006).
- [65] M. Dorati, T. A. Gail, and T. R. Hemmert, *Nucl. Phys.* **A798**, 96 (2008).
- [66] P. Wang, D. B. Leinweber, A. W. Thomas, and R. D. Young, *Phys. Rev. D* **75**, 073012 (2007).
- [67] B. C. Tiburzi, *Phys. Rev. D* **72**, 094501 (2005).
- [68] O. Bar, C. Bernard, G. Rupak, and N. Shores, *Phys. Rev. D* **72**, 054502 (2005).
- [69] C. Aubin, J. Laiho, and R. S. Van de Water, *Phys. Rev. D* **75**, 034502 (2007).
- [70] J.-W. Chen, D. O'Connell, and A. Walker-Loud, *Phys. Rev. D* **75**, 054501 (2007).
- [71] M. Procura, B. U. Musch, T. Wollenweber, T. R. Hemmert, and W. Weise, *Phys. Rev. D* **73**, 114510 (2006).
- [72] C. Best *et al.*, *Phys. Rev. D* **56**, 2743 (1997).
- [73] D. Brömmel *et al.*, *Proc. Sci.*, LAT2005 (2006) 360.
- [74] S. Capitani *et al.*, *Phys. Lett. B* **639**, 520 (2006).
- [75] P. J. Sutton, A. D. Martin, R. G. Roberts, and W. J. Stirling, *Phys. Rev. D* **45**, 2349 (1992).
- [76] M. Glück, E. Reya, and I. Schienbein, *Eur. Phys. J. C* **10**, 313 (1999).
- [77] K. Wijesooriya, P. E. Reimer, and R. J. Holt, *Phys. Rev. C* **72**, 065203 (2005).
- [78] C. Alexandrou *et al.*, *Phys. Rev. D* **69**, 114506 (2004).
- [79] C. Alexandrou *et al.*, *Phys. Rev. Lett.* **94**, 021601 (2005).
- [80] C. Alexandrou, T. Leontiou, J. W. Negele, and A. Tsapalis, *Phys. Rev. Lett.* **98**, 052003 (2007).
- [81] Durham Database Group at Durham University (UK).
- [82] T. Gail, in *Lattice QCD, Chiral Perturbation Theory and Hadron Phenomenology, I3HP Workshop, ECT, Trento, Italy, 2006*, edited by U.-G. Meissner and G. Schierholz (2006), arXiv:hep-ph/0611072.
- [83] O. V. Teryaev, arXiv:hep-ph/9904376.
- [84] O. V. Teryaev, *AIP Conf. Proc.* **915**, 260 (2007).
- [85] R. G. Edwards *et al.* (LHPC), *Phys. Rev. Lett.* **96**, 052001 (2006).
- [86] J. W. Negele *et al.*, *Nucl. Phys. B, Proc. Suppl.* **128**, 170 (2004).
- [87] R. F. Dashen, E. Jenkins, and A. V. Manohar, *Phys. Rev. D* **49**, 4713 (1994).